Development of a Novel High Efficiency Dye-sensitized Solar Cell Using ZnO Based Electrodes

by

Shengwen Hou
Student ID Number: 1186003

A dissertation submitted to the
Engineering Course, Department of Engineering,
Graduate School of Engineering,
Kochi University of Technology,
Kochi, Japan
in partial fulfillment of the requirements for the degree of
Doctor of Philosophy

Assessment Committee:
Supervisor: Chaoyang Li
Co-Supervisor: Toshiyuki Kawaharamura
Co-Supervisor: Hisao Makino
Akimitsu Hatta
Mamoru Furuta

March 2017

Development of a Novel High Efficiency Dye-sensitized Solar Cell Using ZnO Based Electrodes

Shengwen Hou

Abstract

Dye-sensitized solar cell (DSSC) has attracted extensive attention and been considered as a promising candidate for the next generation solar cell due to its advantages such as low-cost, relatively simple fabrication process, and environmentally friendly materials. Since DSSC was invented by Prof. M. Graetzel and Dr B. O'Regan in 1991, it has gained more and more research attention all over the world in over last 25 years. Until now, the highest conversion efficiency of DSSC reported by Graetzel's group has reached to 15%. However, the development of DSSC has encountered the bottleneck in the improvement of conversion efficiency. The reasons are small surface area and low transportation of TiO_2 based photoanode, low photoelectric conversion of dye, and corrosion of redox electrolyte etc.

Photoanode is one of the most important parts for DSSC. Photoanode is composed of the photoanode material and transparent conductive oxide (TCO) substrate. High transmittance and large surface area for dye absorption are the basic requirement for photoanode material. TiO_2 is the most common photoanode material used in DSSCs. Anatase TiO_2 has a better photovoltaic performance than other phases due to its larger bandgap. However, TiO_2 is difficult to obtain textured structure to enlarge the surface area to absorb more dye molecules. Moreover, the low electron mobility (i.e. 0.1~4 $cm^2/(V•s)$) of TiO_2 causes low transportation during electron transportation from TiO_2 to substrate. These limitations influence the conversion efficiency of TiO_2 based DSSC. Compared with TiO_2, ZnO has similar energy bandgap (3.3 eV) with TiO_2 (3.2 eV). However, ZnO has much higher electron mobility (i.e. 200~1000 $cm^2/(V•s)$) than TiO_2. In addition, ZnO is much easier to be fabricated into nanostructures. Therefore, ZnO is one of the most promising alternative photoanode materials for DSSC. So far, ZnO based DSSC has reached the highest conversion efficiency of 8.03% using ZnO nanostructures after air plasma treatment. Therefore, ZnO shows high potential to be applied in DSSC.

ITO or FTO are the most common TCO substrates. However, vertical alignment of ZnO nanorods could not be well controlled on ITO or FTO. Therefore, suitable TCO substrates should be studied to replace ITO or FTO. Based on our previous research, fabrication of vertical aligned ZnO nanorods was still not well studied. The growth mechanism of vertical aligned ZnO nanorods should be further investigated.

In order to solve above problems, we designed a novel photo electrode structure that ZnO nanorods fabricated on ZnO based substrates, which was called the unified ZnO electrodes. Unified ZnO electrodes were expected to fabricate ZnO nanorods with good crystallinity, good vertical alignment and large surface area. Furthermore, due to the high electron recombination and low stability in acidic

electrolyte of ZnO-based electrodes, anatase TiO_2 shell was coated on ZnO nanorods with the purpose to reduce electron recombination and improve the stability.

In my research, there are several novel ideas to improve performance of ZnO based DSSC.

1. The unified ZnO electrodes, which was ZnO nanorods fabricated on aluminium or gallium doped ZnO substrates. The fabrication of unified ZnO electrodes included the fabrication of AZO or GZO films and vertical alignment of ZnO nanorods.

1.1. The transparent conductive AZO and GZO films with low resistivity and high transmittance were deposited to replace ITO as TCO substrates. The effects of metal doping on crystallinity, resistivity, and transmittance were investigated.

1.2. Vertical alignment of ZnO nanorods was controlled on ZnO based substrates to improve optical transmittance and crystallinity. The growth mechanism of vertical aligned ZnO nanorods was investigated.

2. Anatase TiO_2 shell was coated on ZnO nanorods to reduce electron recombination. The mechanism of TiO_2 shell improving the performance of DSSC was investigated.

The main work will be discussed in terms of fabrication of unified ZnO electrodes including transparent conductive ZnO based substrates, vertical alignment controlling on ZnO based substrates, and fabrication of ZnO-TiO_2 core-shell nanorods.

1. Deposition of transparent conductive ZnO based substrates

Transparent conductive substrates should not only have low resistivity, high optical transmittance and high electron mobility, but also contribute to the vertical alignment of ZnO nanorods. However, common substrates such as ITO could not contribute to the vertical alignment of ZnO nanorods due to large lattice mismatch. Therefore, transparent conductive substrates with low lattice mismatch were studied.

Transparent conductive AZO and GZO films were deposited by sputtering system with optimized deposition conditions. The aluminium and gallium dopants not only improved the crystallinity of ZnO film, but also the resistivity and electron mobility. Film thickness dependence on structural, optical and electrical properties of films was investigated. As film thickness increased from 50 to 300 nm, the crystallinity of AZO and GZO films was improved, resistivity decreased, and electron mobility increased. 300 nm-thick AZO film showed lowest resistivity of 6.23×10^{-4} Ω•cm, highest mobility of 18.1 $cm^2/(V\bullet s)$ and high optical transmittance of 85%, which were comparable to commercial ITO substrate of Sigma-Aldrich Co. Ltd (a resistivity of 3×10^{-4} Ω•cm, a mobility of 20 $cm^2/(V\bullet s)$ and optical transmittance of 84%). Moreover, (0001) orientation growth was controlled for AZO and GZO films. The lattice constants of AZO and GZO films were 0.52126 nm and 0.52074 nm, respectively, which were very close to that of bulk ZnO (0.52070 nm).

In summary, 300 nm-thick AZO and GZO substrates could replace ITO substrate to be used as TCO layers for electrode of DSSC. The deposited ZnO based substrates showed very similar lattice constants to bulk ZnO.

2. Vertical alignment controlling of ZnO nanorods on ZnO based substrates during multi-annealing process

High transmittance was required for both substrate and ZnO nanorods in application of DSSC. Therefore, ZnO nanorods should be fabricated in vertical alignment to reduce the light scattering and absorption. Our previous research verified that the lattice mismatch influenced the vertical alignment of ZnO nanorods. However, the merchanism was not clear. In order to realize the vertical alignment of ZnO nanorods, further studies were performed.

Multi-annealing process was developed to fabricate ZnO nanorods. The influence of substrates including AZO, GZO, and ITO substrates on the growth of ZnO nanorods was investigated. It was found that ZnO nanorods fabricated on ZnO based substrates were vertical alignment while those fabricated on ITO substrate were not vertical aligned. The calculated lattice constant c showed lattice mismatches between ZnO nanorods and AZO film, ZnO nanorods and GZO, ZnO nanorods and ITO substrate were 0.048%, 0.035%, and 70.35%, respectively. During multi-annealing process, ZnO film was reduced to zinc and ZnO nuclei formed on the surface of ZnO film. ZnO nuclei would follow the same (0001) growth direction with ZnO based substrates according to minimum energy principle. Due to (0001) orientation was the polarization direction of ZnO, ZnO nanorods would prefer to grow along this orientation. Therefore, vertical alignment of ZnO nanorods was well controlled, which had high optical transmittance. The mobility and optical transmittance of unified ZnO electrodes were 10.2 $cm^2/(V•s)$ and over 70% in visible range, which were much better than those of TiO_2 based electrodes (0.01~4 $cm^2/(V•s)$ and below 50% in visible range).

In summary, the growth direction of ZnO nanorods followed the same vertical growth direction with underneath ZnO based substrate due to the low lattice mismatch between ZnO nanorods and substrate. The unified ZnO electrodes showed greatly improved mobility and optical transmittance than TiO_2 based electrodes.

3. Vertical alignment controlling of ZnO nanorods on ZnO based substrates during chemical bath deposition.

Chemical bath deposition (CBD) is a low-temperature method to fabricate ZnO nanorods. During CBD process, substrates served as the seed layer for ZnO nanorods. Vertical alignment of ZnO nanorods was largely influenced by the substrates. Therefore, vertical alignment of ZnO nanorods in CBD method should be studied.

AZO film was used as substrate for growing ZnO nanorods by CBD method. It was found that vertical alignment of ZnO nanorods was obtained on AZO substrate. During CBD process, ZnO nanorods were grown at AZO substrate, which served as seed layers. As well-known, (0001) orientation is the polarization direction of ZnO nanords. Because ZnO based substrates had good (0001) orientation, ZnO nanorods would follow the same (0001) growth direction due to homogenous growth. As growth time increased, ZnO nanorods would prefer to grow vertically on ZnO based

substrates. Moreover, the effects of AZO film thickness, precursor concentration and growth time on growth of ZnO nanorods were investigated. As thickness of AZO film increased, the diameter of ZnO nanorod increased due to the increasing grain size of AZO film. As precursor molecule concentration ratio increased, the growth of ZnO nanorods was suppressed. As growth time expanded, ZnO nanorods kept the same (0001) orientation with AZO film.

In summary, ZnO nanorods followed the same (0001) growth direction with ZnO based substrates due to homogenous growth. Therefore, vertical alignment of ZnO nanorods was controlled on ZnO based substrates by CBD method.

4. Fabrication of ZnO-TiO_2 core-shell nanorods.

Until now, the performance of ZnO based DSSC was limited by high electron recombination, low stability in acidic electrolyte solution, and formation of Zn^{2+}/dye complex on the surface. In order to overcome these disadvantages, ZnO nanorods should be coated with a chemically stable shell. Anatase TiO_2 had similar bandgap to ZnO, which meant electron could easily transport from TiO_2 to ZnO. Anatase TiO_2 was more chemically stable and had low electron-hole recombination, which was expected to improve the performance of ZnO based electrodes. Therefore, anatase TiO_2 was coated on ZnO nanorods.

TiO_2 film was synthesized on ZnO nanorods using titanium tetraisopropoxide (TTIP) as titanium source by mist-CVD method. It was found that pure anatase TiO_2 film with very uniform surface could be synthesized by mist-CVD method. The anatase TiO_2 films were stable and not transformed to rutile phase at high temperature of 1000 ˚C, which meant this TiO_2 film had very high thermal stability. This is the highest non-transformation temperature for anatase TiO_2. Anatse TiO_2 shell showed a significant influence on the efficiency ZnO based DSSC. As the thickness of TiO_2 shell increased, the anatase crystallinity of TiO_2 shell was increased and the optical transmittance was decreased. After coated with TiO_2 shell, short circuit current density (J_{sc}) and fill factor (FF) of ZnO based DSSC was significantly improved. The conversion efficiency of ZnO based DSSC was twice improved after coated with TiO_2 shell.

Anatase TiO_2 shell had slightly higher conductive band with ZnO nanorods, which meant electrons could easily transmit from conductive band of TiO_2 to that of ZnO. Therefore, during electron transmission, electron was ejected from the lowest unoccupied molecule orbit (LUMO) of dye molecule to the conductive band of TiO_2 shell and then transmitted to that of ZnO nanorods. Because of the barrier between TiO_2 shell and ZnO nanorods, the electron-dye and electron-I_3^- recombination were greatly suppressed. Furthermore, because electron mobility in ZnO was much faster than that in TiO_2, the electron transportation from dye to conductive band of TiO_2 and then through ZnO nanorods to AZO substrate was significantly improved. Therefore, the TiO_2-ZnO core-shell greatly improved J_{sc} and FF.

In summary, ZnO-TiO_2 core-shell nanorods were verified to help utilize electron mobility and diffusion rate of ZnO nanorods as well as the low recombination of TiO_2. Low electron recombination

and fast electron mobility of ZnO based electrodes improved the performance of DSSC. Therefore, the efficiency of ZnO based DSSC was greatly improved after coating anatase TiO_2 shell.

Acknowledgements

I would like to express my sincere gratitude to my supervisor Prof. Chaoyang Li for her brilliant guidance and endless support during my PhD study and research. You are a tremendous mentor to me. Your advice on both research as well as on my career have been priceless. Your strict attitude to research makes me a better researcher. I have learned so much from you in both research work and lifestyle. I am honored to be one of your students.

I would also like to thank my vice-supervisor Associate Prof. Toshiyuki Kawaharamura and Associate Prof. Hisao Makino for your helpful comments and suggestions in my research. Your support to my experiments and analysis makes me do the research smoothly and efficiently.

I would also like to thank my committee members, Prof. Akimitsu Hatta and Prof. Mamoru Furuta for the support of doing the research in your laboratory and cleanroom.

I would also like to give my special appreciations to my senior, Dr. Dapeng Wang and Dr. Xin Li for your excellent guidance and support in my research. You have introduced me to be a real researcher.

My sincere appreciations extended, to Dr. Noriko Nitta for the support of TEM and FIB measurement. I am also grateful to the members in Institute of Nanotechnology for your kind help to teach me the operation of many instruments.

I would like to thank the staff of International Relation Division. You made my life in Japan convenient and colourful. I have experienced many traditional Japanese cultures with your support. You helped me experience a totally different and exciting Japan.

I would also like to thank all of my friends who supported me in doing experiment, analysis, and writing as well as cheering me up when I was upset with the problems I cannot solve. You are really like my family in this university. You colour my social life. I cherish all the valuable moments we had together.

I appreciate the homestay in Mr. Morimoto who lives in Nankoku, Kochi. You are so kind and friendly. I have a deep and new understanding of Japanese style. The homestay in your home will be one of valuable memories in my life.

A special thank is for my family. Words cannot express how grateful I am to my father, mother and sister for all of the sacrifices that you have made on my behalf. Your understanding and support sustained me the whole time.

List of Figures

List of Tables

Contents

Chapter 1

Introduction

1.1 Research on ZnO material

1.1.1 Basic properties of ZnO

Zinc oxide (ZnO) is a II-VI compound oxide semiconductor with wide direct bandgap of 3.37 eV. The study of ZnO material started in 1912. Since the semiconductor age started, the systematic investigations of ZnO as a compound semiconductor were performed [1].

ZnO naturally crystallizes in wurtzite structure, as shown in Fig. 1.1(a) [2]. Wurtzite structure, which belongs to space group of *p6mc*, is characterized by two interconnecting sublattices of Zn^{2+} and O^{2-}. In this configuration, each Zn ion is surrounded by a tetrahedral of O ions and each O ion is also surrounded by a tetrahedral of Zn ions. The configuration of tetrahedral coordination in ZnO determines the polar symmetry along hexagonal axis, shown in Fig 1.1(b). This polarity of ZnO crystal induces many properties such as the crystal growth, etching and defect generation. ZnO crystals exhibit several typical surface orientations. The most important surfaces are the polar Zn-terminated (0001) and O-terminated (000-1) (c-axis oriented), the non-polar (11-20) and (10-10) faces [3]. For ZnO crystal, (0001) orientation has the lowest Gibbs free energy, which is the preferred orientation for hexagonal ZnO growth. The lattice parameters of hexagonal unit cell are a = 3.2495 Å and c = 5.2069 Å [4].

ZnO crystal has native point defects which form the electronic states in the bandgap and influence its optical and electrical properties. Oxygen vacancies and zinc interstitials are the most common defects in ZnO crystals [5]. Existence of defects causes the distortion of bandgap and also works as the donors located in deep or shallow levels, which influences the electron transmission and luminescent property. Due to these defects in ZnO, ZnO has been used in the application of light emission diodes [6].

ZnO has many unique properties such as the wide direct bandgap of 3.37 eV and a large exciton binding energy of 60 meV at room temperature. The strong high binding energy, which is much larger than that of GaN (25 meV), can greatly improve the exciton emission at room temperature under low excitation energy. Additionally, ZnO is easy to be fabricated into single crystals, which makes ZnO an ideal candidate for a variety of devices such as sensors, ultra-violet laser diodes and displays [7,8].

ZnO also has piezoelectric properties due to its non-central symmetric structure of tetrahedral

coordination, which has high potential to be used in the sensors and actuators [9,10].

1.1.2 Fabrication of ZnO nanostructures

Nanostructured ZnO materials have received much attention due to their good performance in electronics, optics and photonics. Because wurtzite ZnO has a high polarized (0001) orientation, the formation of ZnO films or nanostructures prefers to grow along this orientation. Therefore, ZnO can be easily fabricated into various nanostructures such as nanorods [11], nanoflowers [12], nanobelts [13], and nanocombs [14] etc, shown in Fig. 1.2. The morphology of ZnO nanostructures is dependent on the fabrication method and experimental parameters. During the past several decades, ZnO nanostructures were fabricated using various methods including vapor-liquid-solid process (VLS) [15], pulse laser deposition (PLD) [16], chemical vapor deposition (CVD) [17,18], electrochemical [19], hydrothermal method, and chemical bath deposition (CBD) [20-22] etc.

For most fabrication method, seed layer such as Au is nessasary to obtain ZnO nanostructures [23]. The seed layer serves as a growth site for the nucleation during fabrication of ZnO nanostructures. For example, Au is used as the seed layer for ZnO nanowires via VLS process. The liquid droplet serves as the preferentiual site for absorption of fas phase reactant. When supersaturated, the nucleation site for crystallization occurred. During growth, the catalyst droplet directs the nanowire's growth direction and defines the diameter of the nanowire. Eventually, the growth is terminated when the reactant is no longer available or temperature is below the eutectic temperature for catalyst. Research reported that Sn can also be an effective catalyst for growing ZnO nanorods [24]. Not only the seed layer but also the geometrical shape of substrate can affect the growth morphology of ZnO nanorods [25].

The electrical and optical properties of ZnO nanostructures could be modified with ion implanation. Metal elements such as Cu, Ag, Mn and Na are doped into the ZnO nanostructures, resulting in substantial changes in terms of strutural, electrical and optical properties [26-28].

ZnO nanostructures exhibits a direct bandgap of 3.37 eV at room temperature with a large exciton energy of 60 meV. Moreover, single crystals nanostructures usually perform a UV emission and strong visible emission, which are attributed to the near band edge emission and defects emission. Therefore, ZnO has been applied in blue-UV emission and displays [29,30].

ZnO nanostructures usually has small dimensions, the oxygen sites density are much higher, which can significantly influence the conductivity of ZnO nanostructures. Therefore, the electrical conductivity of ZnO nanostructures can be changed due to the interaction between surface complexes such as O^-, O_2^-, H^+ and OH^- etc reactive chemical species or gas molecules. Therefore, ZnO nanostructures can be used for gas, chemical and biology sensors [31].

ZnO nanostructures has much larger surface area than film. Moreover, ZnO nanostructures are single crystal, which the electron mobility in ZnO is very high. The wide bandgap indicates ZnO has higher surface energy. All these advantages gurantee ZnO nanostructures has a high photocatalytic and photovoltaic activity. Therefore, ZnO nanostructures are also widely investigated in the application of photocatalytic and photovoltaic devices [32,33].

1.2 Research on ZnO based DSSC

1.2.1 Introduction of ZnO based DSSC

Recently, fuel and energy crisis became more and more serious due to depleting fossil fuels while the demand for energy is growing. Renewable energy sources such as solar and wind have become important approaches for gaining independence from fossil fuels. Utilizing solar energy is certainly one of the most viable ways to solve the world's energy crisis. Dye-sensitized solar cells (DSSC) have emerged as promising candidates for ultilizing solar power due to its advantages such as low-cost, relatively simple fabrication process, and environmentally friendly materials. Since DSSC was invented by Prof. M. Graetzel and Dr B. O'Regan in 1991 [34], it has gained more and more research attention all over the world in over last 25 years.

A conventional DSSC is composed of four parts including electrode, dye, electrolyte and cathode. Mesoporous TiO_2 film is deposited on transparent conductive oxide (TCO) substrate, which is composed the photoelectrode. The dye molecules anchored on the surface of TiO_2 film are the photoactive material of DSSC, and can produce electricity once they are sensitized by light.

The working principle of DSSC is explained as follows, shown in Fig. 1.3. The dye molecules absorb photons of incoming light (sunlight and ambient artificial light) to excite electrons from highest occupied molecule orbital (HOMO) to lowest unoccupied molecule orbital (LUMO). The dyes inject excited electrons into the conductive band of TiO_2. The electrons are conducted away by nanocrystalline TiO_2 and TCO substrate to the circuit. Then the electrons are transmitted to cathode part. The dyes are regenerated by iodide ions in the electrolyte. The iodide ions are reduced to triiodide ions by the electrons from cathode part. This is how DSSC generates electricity.

Over last 25 years, the overall efficiency of DSSC was greatly improved [35-37]. So far, the highest energy conversion efficiency of DSSC was 15%, made by research group of Prof. Grazel [38].

However, the development of DSSC has encountered the bottleneck in the improvement of conversion efficiency. The reasons include that mall surface area and low transportation of TiO_2

based electrode, low photoelectric conversion of dye, and corrosion of redox electrolyte etc. In this thesis, I will focus on the fabrication of electrode.

Electrode is one of the most important parts for DSSC, which is composed of the electrode material and TCO substrate. High transmittance and large surface area for dye absorption are the basic requirement for electrode material.

TiO_2 is the most common electrode material used in DSSCs. Anatase TiO_2 has a better photovoltaic performance than other phases due to its larger bandgap. However, TiO_2 is difficult to obtain textured structure to absorb more dye molecules. The low electron mobility (i.e. 0.1~4 $cm^2/(V•s)$) of TiO_2 causes low transportation during electron transportation from TiO_2 to substrate. These limitations influence the conversion efficiency of TiO_2-based DSSC [39,40].

Compared with TiO_2, ZnO has similar energy bandgap (3.3 eV) with TiO_2 (3.2 eV). However, ZnO has much higher electron mobility (i.e. 200~1000 $cm^2/(V•s)$) than TiO_2 [41]. In addition, ZnO is much easier to be fabricated into nanostructures [42]. Therefore, ZnO is one of the most promising alternative electrode materials for DSSC.

In my research, the traditional TiO_2 films were replaced with the ZnO nanostructures as the electrode material. Compared to TiO_2 based electrodes, ZnO nanostructures based electrodes had similar bandgap, much faster electron transportation and relatively large surface area, which was expected to improve the conversion efficiency of DSSC.

1.2.2 Development of ZnO based DSSC

The development of ZnO based DSSC was earlier but much slower than that of TiO_2 based DSSC. The first record of ZnO based DSSC was in 1980. The porous ZnO films were used to fabricate dye-sensitized photoanode. The energy conversion efficiency of 2.5% for specific incidence light of 562 nm [43]. However, the conversion efficiency for ZnO based DSSC in the whole light range was from 0.4% to 5.7% in last 30 years [12,44,45].

Saito et al [46] fabricated ZnO photoanode using nanocrystalline ZnO nanoparticles. The conversion efficiency was up to 6.58% using N719 as the dye sensitizer.

Memarian et al. [47] obtained the high conversion efficiency of 7.5% by fabricating hierarchically structured ZnO-based photoanodes.

He et al. [48] adopted the air plasma treatment to ZnO nanostructures, and obtained the high conversion efficiency of 8.03%. It is the highest conversion efficiency of ZnO based DSSC until now.

The conversion efficiency of ZnO based DSSC was much lower than that of TiO_2 based DSSC. One important reason is that it is difficult to obtain ZnO nanorods with vertical alignment.

Vertical alignment for ZnO nanorods not only improves the transmittance of electrode, but also improves the transportation from ZnO nanorods to TCO substrates. As reported, the vertical alignment of ZnO nanorods was significantly dependent on the substrates. However, the most common TCO substrates such as ITO or FTO cannot contribute to the vertical alignment due to large lattice mismatch [49]. Therefore, suitable TCO substrates should be studied to replace ITO or FTO. Based on our previous research [49-51], fabrication of vertical aligned ZnO nanorods was still not well studied. The growth mechanism of vertical aligned ZnO nanorods should be further investigated. Furthermore, ZnO-based electrodes have high electron recombination and low stability in acidic electrolyte. All these remained issues limited the improvement of ZnO based DSSC.

1.3 Objectives and structure of this thesis

In this thesis, in order to solve above remained problems, we designed a novel photo electrode structure that ZnO nanorods fabricated on ZnO based substrates, which was called the unified ZnO electrodes. Unified ZnO electrodes were expected to fabricate ZnO nanorods with good crystallinity, good vertical alignment and large surface area. Furthermore, due to the high electron recombination and low stability in acidic electrolyte of ZnO-based electrodes, anatase TiO_2 shell was coated on ZnO nanorods with the purpose to reduce electron recombination and improve the stability.

In my research, there are several novel ideas to improve performance of ZnO based DSSC.

1) Aluminium or gallium doped ZnO substrates with low resistivity and high transmittance were deposited as TCO substrates to replace ITO. The effects of metal dopping on crystallinity, resistivity and transmittance were investigated.

2) Vertical alignment of ZnO nanorods was controlled on ZnO based substrates to improve optical transmittance and crystallinity. The growth mechanism of vertical aligned ZnO nanorods was investigated.

3) Anatase TiO_2 shell was coated on ZnO nanorods to reduce electron recombination. The mechanism of TiO_2 film reducing the recombination was investigated.

The main work will be discussed in terms of fabrication of transparent conductive ZnO based substrates, vertical alignment controlling on ZnO based substrates, and fabrication of ZnO-TiO_2 core-shell nanorods. The structure of my thesis was shown in Fig. 1.4.

Chapter 1: Research background of ZnO material and ZnO-based DSSC including the development and applications was introduced in details. The objectives of thesis were proposed and the structure of thesis was settled.

Chapter 2: The principle and measurement methods of fabrication and characterization equipment were briefly introduced.

Chapter 3: Fabrication and characterization of vertical aligned ZnO nanorods by multi-annealing method were investigated in detail. Vertical alignment control of ZnO nanorods by multi-annealing was discussed. The deposition and characterization of aluminium and gallium doped ZnO films was also investigated.

Chapter 4: Fabrication and characterization of vertical aligned ZnO nanorods by chemical bath deposition method were investigated in detail.

Chapter 5: Fabrication and characterization of TiO_2 coating on ZnO nanorods by mist chemical vapour deposition method were investigated. The deposition and characterization of pure anatase TiO_2 film was also discussed in detail.

Chapter 6: ZnO based DSSCs were fabricated and evaluated. The effects of surface area, post-treatment and TiO_2 coating on the performance of DSSC were investigated.

Chapter 7: The main results of this thesis were summarized. The future improvement and application were discussed.

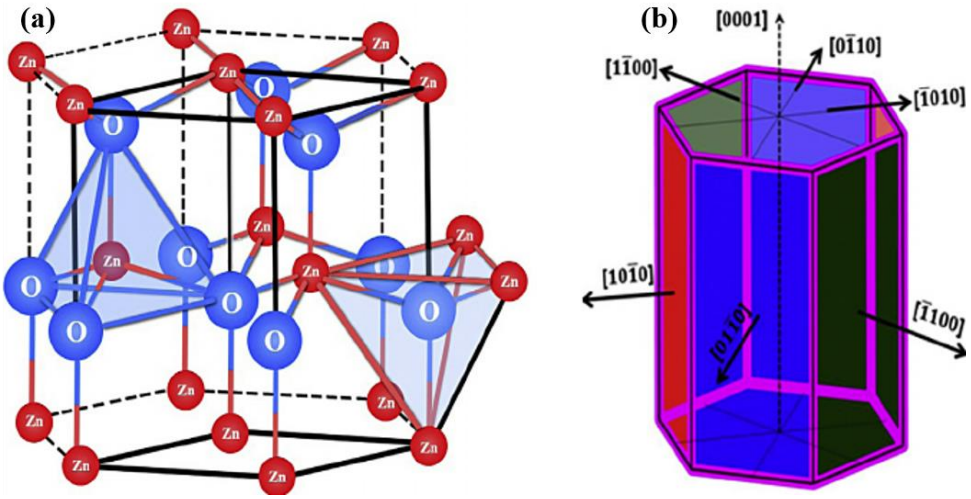

Fig. 1.1 (a) hexagonal wurtzite crystal structure and (b) different crystallographic faces of ZnO [1].

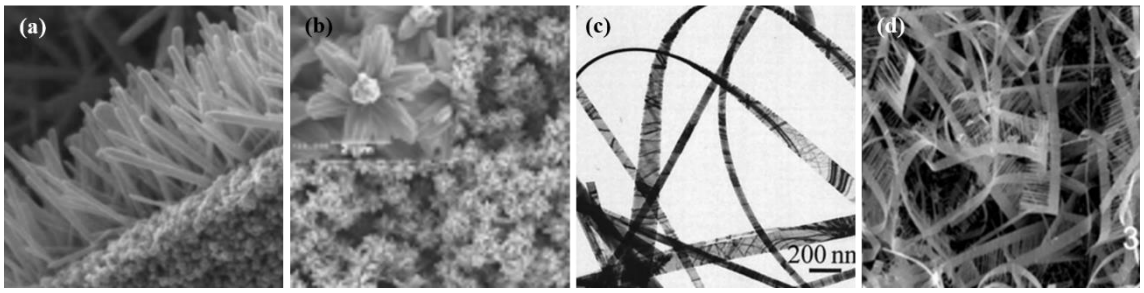

Fig. 1.2 Different shapes of Zno nanostructures. ((a) nanorods [11], (b) nanoflowers [12], (c) nanobelts [13], and (d) nanocombs [14])

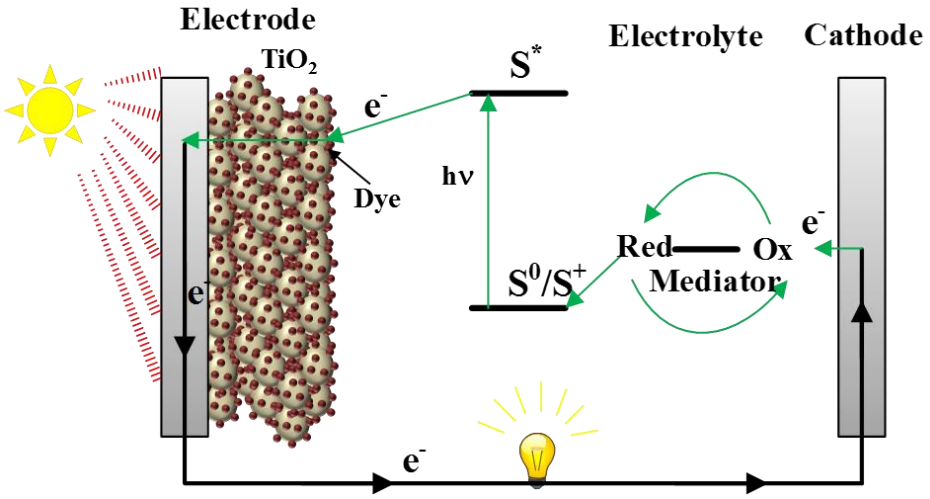

Fig. 1.3 The working principle of dye-sensitized solar cell.

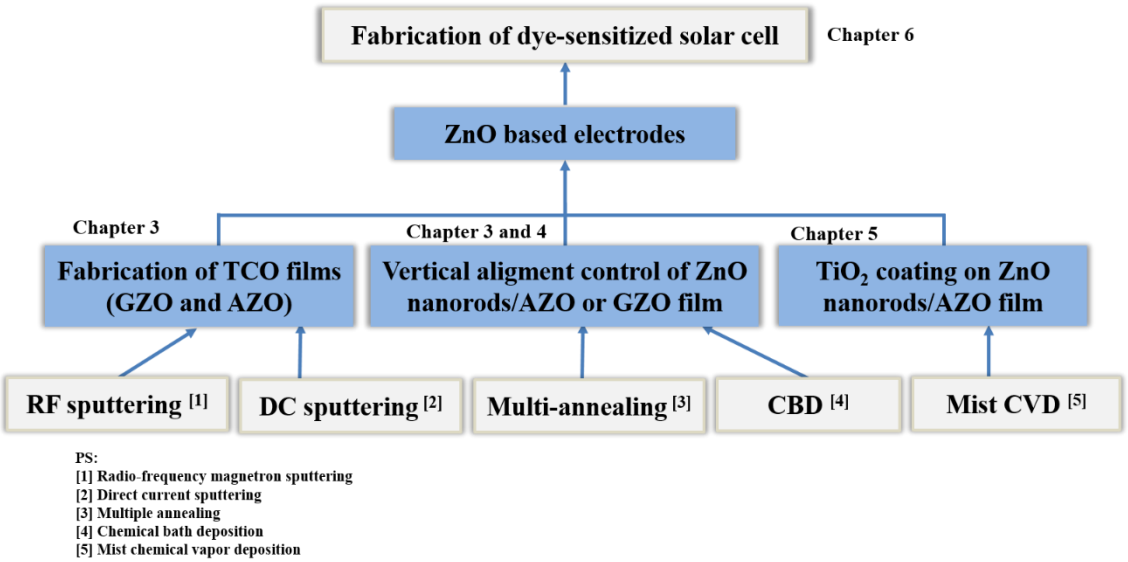

Fig. 1.4 The thesis structure.

1.4 References

[1] J. Bardeen, and W.H. Brattain. *Phys. Rev.* 74 (1948) 230.

[2] A.S. Kamble, B.B. Sinha, K. Chung, M.G. Gil, V. Burungale, C.J. Park, J.H. Kim, and P.S. Patil. *Electrochim. Acta,* 149 (2014) 386-393.

[3] O. Dulub, L.A. Boatner, and U. Diebold. *Surf. Sci.* 519 (2002) 201-217.

[4] D.R. Lide (Ed.). CRC Handbook of Chemistry and Physics, 73rd Edition, CRC Press, New York, 1992.

[5] A.F. Kohan, G. Ceder, D. Morgan, and C.G. Van de Walle. *Phys. Rev. B,* 61 (2000) 15019-15027.

[6] X.L. Guo, J.H. Choi, H. Tabata, and T. Kawai. *Jpn. J. Appl. Phys.* 40 (2001) L177-L180.

[7] D.K. Hwang, S.H. Kang, J.H. Lim, E.J. Yang, J.Y. Oh, J.H. Yang, and S.J. Park. *Appl. Phys. Lett.* 86 (2005) 222101.

[8] J.F. Wager. *Science,* 300 (2003) 1245-1246.

[9] S.H. Park, C.W. Ahn, S. Nahm, and J.S. Song. *Jpn. J. Appl. Phys.* 43 (2004) L1072-L1074.

[10] J.H. He, C.L. Hsin, J. Liu, L.J. Chen, and Z.L. Wang. *Adv. Mater.* 19 (2007) 781-784.

[11] L. Vayssieres. *Adv. Mater.* 15 (2003) 464-466.

[12] C.Y. Jiang, X.W. Sun, G.Q. Lo, D.L. Kwong, and J.X. Wang. *Appl. Phys. Lett.* 90 (2007) 263501.

[13] Z.W. Pan, Z.R. Dai, and Z.L. Wang. *Science,* 291 (2001) 1947-1949.

[14] X. Pan, X. Liu, A. Bermak, and Z. Fan. *ACS Nano,* 7 (2013) 9318-9324.

[15] S.E. Ahn, J.L. Soo, H. Kim, S. Kim, B.H. Kang, K.H. Kim, and G.T. Kim. *Appl. Phys. Lett.* 84 (2004) 5022-5024.

[16] T. Okada, B.H. Agung, and Y. Nakata. *Appl. Phys. A,* 79 (2004) 1417-1419.

[17] X. Liu, X. Wu, H. Cao, and R.P.H. Chang. *J. Appl. Phys.* 95 (2004) 3141-3147.

[18] A. Yengantiwar, R. Sharma, O. Game, and A. Banpurkar, *Curr. Appl. Phys.* 11 (2011) S113-S116.

[19] S. Chu, D. Li, P.C. Chang, and J.G. Lu. *Nanoscale Res. Lett.* 6 (2011) 1-4.

[20] I. Gonzalez-Valls, Y. Yu, B. Ballesteros, J. Oro, and M. Lira-Cantu. *J. Power Sources,* 196 (2011) 6609-6621.

[21] S. Kahraman, H.M. Çakmak, S. Çetinkaya, H.A. Çetinkara, and H.S. Güder. *Internat. J. Mater. Res.* 104 (2013) 799-804.

[22] P.K. Baviskar, P.R. Nikam, S.S. Gargote, A. Ennaoui, and B.R. Sankapal. *J. Am. Ceram.* 551 (2013) 233-242.

[23] M.H. Huang, Y. Wu, H. Feick, N. Tran, E. Weber, and P. Yang. *Adv. Mater.* 13 (2001) 113-116.

[24] P. Gao, and Z.L. Wang. *J. Phys. Chem. B,* 106 (2002) 12653-12658.
[25] J.Y. Lao, J.Y. Huang, D.Z. Wang, and Z.F. Ren. *Nano Lett.* 3 (2003) 235-238.
[26] J.P. Cheng, X.B. Zhang, and Z.Q. Luo. *Surf. Coat. Technol.* 202 (2008) 4681-4686.
[26] R. Mohan, K. Krishnamoorthy, and S.J. Kim. *Sol. Sta. Commun.* 152 (2012) 375-380.
[27] X.H. Huang, C. Zhang, C.B. Tay, T. Venkatesan, and S.J. Chua. *Appl. Phys. Lett.* 102 (2013) 111106.
[28] M.H. Hsu, and C.J. Chang. J. Hazard. *Mater.* 278 (2014) 444-453.
[29] G.S.R. Raju, E. Pavitra, G. Nagaraju, and J.S. Yu. *Dalton Trans.* 44 (2015) 1790-1799.
[30] S. Kim, M.S. Kim, G. Nam, and J.Y. Leem. *Electron. Mater. Lett.* 8 (2012) 445-450.
[31] N.F. Hamedani, A.R. Mahjoub, A. Ali khodadad, and Y. Mortazavi. *Sens. Actuator B-Chem.* 169 (2012) 67-73.
[32] C. Han, M.Q. Yang, B. Weng, and Y.J. Xu. *Phys. Chem. Phys.* 16 (2014) 16891-16903.
[33] D. Bi, G. Boschloo, S. Schwarzmüller, L. Yang, E.M. Johansson, and A. Hagfeldt. *Nanoscale,* 5 (2013) 11686-11691.
[34] B. O'regan, and M. Grätzel. *Nature,* 353 (1991) 737-740.
[35] A. Sedghi, and H.N. Miankushki. *Int. J. Electrochem. Sci.* 7 (2012) 12078-12089.
[36] J. Gong, J. Liang, and K. Sumathy. Renew. *Sustainable Energy Rev.* 16 (2012) 5848-5860.
[37] M. Fitra, G. Nair, M. Irwanto, M.I. Yusoff, and N. Mariun. *Appl. Mech. Mater.* 699 (2015) 540-545.
[38] J. Burschka, N. Pellet, S.J. Moon, R. Humphry-Baker, P. Gao, M.K. Nazeeruddin, and M. Grätzel. *Nature,* 499 (2013) 316-319.
[39] M. Law, L.E. Greene, J.C. Johnson, R. Saykally, and P. Yang. *Nature Mater.* 4 (2005) 455.
[40] Q. Zhang, C.S. Dandeneau, X. Zhou, and G. Cao. *Adv. Mater.* 21 (2009) 4087-4108.
[41] A. Kołodziejczak-Radzimska, and T. Jesionowski. *Mater.* 7 (2014) 2833-2881.
[42] I. Gonzalez-Valls, and M. Lira-Cantu. *Energy Environ. Sci.* 2 (2009) 19-34.
[43] M. Matsumura, S. Matsudaira, H. Tsubomura, M. Takata, and H. Yanagida. *Ind. Eng. Chem. Prod. Res. Dev.* 19 (1980) 415-421.
[44] G. Redmond, D. Fitzmaurice, and M. Graetzel. *Chem. Mater.* 6 (1994) 686-691.
[45] D. Barpuzary, A.S. Patra, J.V. Vaghasiya, B.G. Solanki, S.S. Soni, and M. Qureshi. *ACS Appl. Mater. Interfaces,* 6 (2014) 12629-12639.
[46] M. Saito, and S. Fujihara. *Energy Environ. Sci.* 1 (2008) 280-283.
[47] N. Memarian, I. Concina, A. Braga, S.M. Rozati, A. Vomiero, and G. Sberveglieri. *Angew. Chem.* 123 (2011) 12529-12533.
[48] Y. He, J. Hu, and Y. Xie. *Chem. Commun.* 51 (2015) 16229-16232.
[49] X. Li, C. Li, T. Kawaharamura, D. Wang, N. Nitta, M. Furuta, H. Furuta, and A. Hatta. Nanosci. *Nanotechnol. Lett.* 6 (2014) 174-180.

[50] C. Li, T. Kawaharamura, T. Matsuda, H. Furuta, T. Hiramatsu, M. Furuta, and T. Hirao. *Appl. Phys. Express,* 2 (2009) 091601.
[51] D. Wang, Z. Li, T. Kawaharamura, M. Furuta, T. Narusawa, and C. Li. *Phys. Status Solidi C,* 9 (2012) 194-197.

Chapter 2

Fabrication equipment and characterization techniques

2.1 Introduction

The equipments used to fabricate and characterize film, nanostructures and DSSC etc were briefly described in this chapter. The ZnO based films were deposited by radio frequency (RF) magnetron sputtering system and direct current (DC) sputtering system. ZnO nanostructures were fabricated by a commercial annealing furnace and chemical bath deposition (CBD). TiO_2 films and ZnO-TiO_2 core-shell structures were fabricated by mist chemical vapour deposition (mist CVD). After fabrication, the samples were evaluated morphological, structural, optical and electrical properties with variety of equipment. The morphologies of films and nanostructures were observed with a field emission scanning electron microscope (FE-SEM) system. Surface roughness was characterized by an atomic force microscope (AFM). The microstructure of nanostructures was measured by a transmission electron microscope (TEM) system. The crystallinity was evaluated with an X-ray diffraction (XRD) system. The luminescent property of nanostructures was performed by photoluminescence (PL) measurement. Raman spectroscopy was measured with a confocal Raman microscope. Optical transmittance spectra were characterized by an ultraviolet-visible spectrophotometer. Electrical properties were measured with a Hall measurement system. All the measurement was carried out at room temperature. In next two sections, the equipments were interpreted in detail.

2.2 Fabrication equipment

2.2.1 Sputtering system

Sputtering is a widely used technique to deposit thin films on different substrates. General sputtering system involves target and substrate. The difference of the power supply classifies the sputtering as RF sputtering and DC sputtering. In general, RF sputtering is used for deposition of insulating, semiconductive materials while DC sputtering is applied to deposit conductive materials [1].

The process of sputtering can be interpreted as follows. Firstly, the ionic plasma is produced from inlet gas such as argon by applying a high voltage to the glow tube. Then the ions bombard the target located in cathode and the target atoms are ejected from the cathode by energy and

momentum transfer. Therefore, the sputtered atoms are deposited on the substrate located in anode. During sputtering process, it is impossible to sputter insulating materials with DC sputtering technique due to the positive charged ions can't flow through the insulator, resulting in that the electric circuit is interrupted. So the cathode potential drops and the positive ions are no longer accelerated towards the target and the process ends. However, due to rapidly changing electric field for RF sputtering, the plasma moves to substrate and target back and forth. The potential difference between cathode and anode can be maintained. Therefore, the insulating materials can be deposited by RF sputtering.

As for the magnetron effect, the magnetron field is oriented parallel to the cathode surface, resulting in that the plasma forms a closed loop in the local polarity of magnetron field. Due to the increased confinement of plasma, the plasma density will be much higher. Therefore, more target atoms are ejected. The sputtered atoms are not affected by the magnetron field due to their electrical neutrality.

In this research, ZnO based films including pure ZnO and aluminum doped ZnO (AZO) films were deposited by a conventional RF (13.56 MHz) magnetron sputtering system, which was shown in Fig. 2.1 [2]. The gallium doped ZnO (GZO) film was deposited by DC sputtering system, shown in Fig. 2.2 [3]. The quality of deposited film was influenced by the deposition parameters including power, working gas pressure, substrate temperature, and the distance from target to substrate etc. Therefore, the deposition conditions are very critical to the deposited films. The deposition conditions of ZnO based films would be discussed in chapter 3 and 4.

2.2.2 Commercial annealing furnace

A commercial annealing furnace used in this research is shown in Fig. 2.3, which is composed of a quartz tube, gas supply system, vacuum system and water cooling system. The heating temperature for this furnace ranges from room temperature to 1000 ℃. Various gases including Ar, O_2 and forming gas (2% H_2 in N_2) can be supplied in the system, depending on the research purpose. A quartz boat is used for holding the treated samples in the furnace.

In this research, the commercial annealing furnace was used to fabricate ZnO nanorods with different ambient [4]. The gases used for fabrication of ZnO nanorods were forming gas and oxygen. The annealing conditions including annealing temperature, time and gas ambient were optimized to obtain ZnO nanorods with large surface area and good vertical alignment. The details of experimental conditions will be interpreted in chapter 3.

2.2.3 Chemical bath deposition

CBD method is one of the easiest and cheapest methods to deposit thin films and nanomaterials due to non-expensive equipment and potentiality for large area deposition [5]. The CBD method contains a heating unit and reaction unit, shown in Fig. 2.4. The heating unit is used to heat the water or other solutions at a certain temperature for reaction. The reaction unit is for the fabrication of thin films or nanomaterials, which is strongly dependent on the chemical reactions. The major advantage of CBD is that it requires only solution containers and substrate mounting devices.

In this research, CBD method was used to synthesize ZnO nanorods on ZnO based substrates. The CBD conditions including growth temperature, precursor concentrations, and growth time were optimized for ZnO nanorods growth.

2.2.4 Mist chemical vapor deposition

Mist CVD is a novel method to fabricate oxide films and nanoparticles. The schematic diagram of mist CVD is shown in Fig. 2.5 [6]. The conventional mist CVD system mainly consists of two parts. The first part is the mist generator unit, in which the solution is atomized to mist droplets by ultrasonic transducer. The frequency of ultrasonic is 2.4 MHz. The second part is the reaction unit. The carrier gas transfers mist droplets from the mist chamber to the reaction unit. The dilution gas dilutes the density of the mist droplets. After mist droplets reach the reaction unit, the droplets will burst into much smaller droplets due to the high temperature and high vapor pressure. These smaller droplets will form very uniform thin films or nanoparticles.

In this research, mist CVD was used to fabricate TiO_2 film and ZnO-TiO_2 core-shell structure nanorods. The deposition conditions were optimized to control the quality of thin films and nanostructures. The details of experimental conditions were interpreted in chapter 5.

2.3 Characterization techniques

2.3.1 Field emission scanning electron microscope

Morphological property of the samples was obtained via FE-SEM system. It contains electron gun, the focus coils, detector system and vacuum system, shown in Fig. 2.6 [7]. A focused beam of high-energy electrons is used to generate a variety of signals at the surface of solid specimens. These signals include secondary electrons, backscattered electrons (BSE), diffracted backscattered electrons (DBSE), photons (characteristic X-rays), visible light (cathodoluminescence), and heat etc. The signals reveal information of the sample including external morphology, chemical composition, crystalline structure, and orientation of materials.

The FE-SEM equipment used in this research was JEOL-JSM7400F, shown in Fig. 2.7. During measurement, the chamber pressure was maintained at 10^{-5} Pa. The gun voltage ranged from 1 to 30 kV. The highest magnification was 300,000X. The observed modes are SEI and LEI modes.

In this research, the morphologies of thin films and nanostructures were measured by the FE-SEM equipment.

2.3.2 Transmission emission microscope

TEM is a microscopy technique to observe the morphology, measure the microstructure and analyze the element composition [8]. TEM contains the electron gun, the coils focus system, the detector system, and vacuum system, shown in Fig. 2.8. When a beam of electrons is transmitted through an ultra-thin specimen, interaction between electrons and specimen can form an image of morphology, a magnified image of the microstructure, and an image of electron diffraction pattern etc. The interaction between electrons and specimen generates the characterized X-ray, which can identify the element composition. It is called energy dispersive X-ray spectrometry (EDX).

In this research, TEM ((JEOL-2100F) measurement was performed to observe the morphology and microstructure of films and nanostructures. The EDX was used to analyze the element composition of the nanostructures.

2.3.3 X-ray diffraction

X-ray is one kind of electromagnetic radiation with the wavelength of 0.1 nm, which equals to the diameter of the atom. X-ray diffraction is one of most popular non-destructive techniques for probing the crystalline structure at atomic level.

Crystal, which means regularity and symmetry, is a regular three-dimensional distribution of atoms in space. A series of parallel planes separated with a distance d are well arranged, which are dependent on various structure and packing method for different materials. According to Bragg's law, when a monochromatic X-ray with the wavelength of λ incident to a crystal sample at an angle of θ, X-ray will be diffracted by parallel planes of atoms [9].

$$n\lambda = 2\mathrm{d}sin\theta \qquad (2.1)$$

Here, n is integer that represents the order of the reflection, λ is the wavelength of X-ray, d is the spacing between diffracting planes, is the incident angle. Therefore, the characteristic of the materials can be evaluated in detail.

The XRD patterns can not only provide the peak position and intensity of the diffracted beam, but also provide structural information of the films or nanostructures. The information including the crystalline orientation, crystallite size, stress and lattice constants can be easily calculated from XRD patterns [10].

In this research, Rigaku ATX-G was used to measure the structural properties of films and nanostructures, shown in Fig. 2.9 [11]. The structural property of ZnO film and nanostructures was measured by using 2θ-ω scanning and employing a Cu Kα tube (λ = 0.154178 nm) radiation (50 kV, 300 mA) in the range from 20 to 40°. The structural property of TiO_2 film was measured by using grazing incidence x-ray diffraction (GIXRD) model at a 0.35° incidence angle in the range from 20 to 80°.

2.3.4 Photoluminescence spectroscopy

PL spectroscopy is a contactless, nondestructive method to probe the electrical properties of materials. Photo-excitation occurs when the light incidents on the sample. Photo-excitation causes electrons with the materials to transmit into other possible energy leves. When the electrons return to the equilibrium states, the energy is leased as photons. The photons can be detected by the CCD camera. The photon energy is dependent on the defects level or dopants level of material. Therefore, the photoluminescence provides a good method to study the electrical property of material [12].

In this research, PL measurement was performed with an iHR320 Micro-PL/Raman spectroscope (Horiba Ltd.) using a He-Cd laser with a wavelength of 325.25 nm as an excitation light source. During measurement, the power of laser ranged from 1 to 5 mW with an exposure time of 0.5-5 s. The composition of PL measurement was shown in Fig. 2.10.

2.3.5 Raman spectroscopy

Raman spectroscopy is a spectroscopic technique to observe vibrational, rotational, and other low-frequency modes in a system. When laser interacts with molecular vibrations, rotations, or phonons in the materials, the energy of the laser photons is shifted left or right. The shift in energy gives information about the vibrational modes in the system. Raman spectroscopy can be used for both qualitative and quantitative applications. The spectra are very unique for different material or different phase of same materials. Chemical identifications can be performed by using search algorithms against digital databases [13].

In this research, a confocal Raman microscope (HORIBA, LabRAM HR800) (shown in Fig. 2.11) with a 532.8 nm excitation laser was used to measure the phase of TiO_2 films.

2.3.6 Transmission spectroscopy

Transmission spectroscopy is one of most basic techniques for analyzing the optical properties of samples in the light range from near UV light to infrared. It is a non-destructive system to measure the optical properties. Light passes through a sample to be registered by a detector and compared to original light. Using this transmission spectroscopy, we can obtain the information of the sample including the absorption coefficient of the sample, the reflectance and refractive index, the dielectric constant, and coarse calculation of bandgap [14].

In this research, optical transmission spectra measurements of samples were performed using an Ultraviolet-Visible-Infrared (UV-Vis-IR) spectrophotometer (U-4100, Hitachi Corp), shown in Fig. 2.12. The measurement region ranges from 175 up to 2600 nm. The transmittance spectra of ZnO films, ZnO nanostructures, TiO_2 films, and core-shell structures were measured via this equipment.

2.3.7 Hall effect measurement

Hall effect measurement has been a valuable tool for electrical property characterization of materials [15]. Basically, when a magnetic field through a sample and a current along the length of the sample are combined together, the electrical current is generated to be perpendicular to both the magnetic field and the current, which in turn creates a transverse voltage that is perpendicular to both the magnetic field and the current. The behind principle is the Lorentz Force. Using this basic principle, Hall effect measurement can be performed to measure the electrical properties of materials. A Hall effect measurement system can actually be used to determine the Hall voltage, carrier mobility, carrier concentration and resistivity etc.

In this thesis, a Hall effect measurement system (Accent HL5500, M-1) was used to measure the electrical properties of ZnO based films, shown in Fig. 2.13. The mobility of ZnO based electrodes was also measured by this Hall measurement.

2.3.8 Atomic force microscopy

AFM is one of the most powerful microscopy technology to study the surface morphology. It is non-destructive and can provide structural, mechanical and functional information under physiological conditions [16]. The schematic diagram of AFM was shown in Fig. 2.14 [17]. The main unit for AFM is the sharp cantilever tip. When the tip approaches to the sample surface, the local force between tip and surface will be detected. Via scanning the sample surface, the

microscopic features of the samples will be detected. Because the images are acquired by the atomic force, the images with good resolution are possible. Therefore, the AFM is a useful instrument for analyzing surface roughness.

In this research, the AFM (Nanoscope II, Digital Instruments) was used to measure the surface root mean squre roughness of ZnO based films, which shown in Fig. 2.15.

2.3.9 Solar simulator system

The nature solar spectrum changes all the time. It is difficult to test solar cell under nature solar illumination. In order to evaluate the fabricated solar cell, standard reference spectra should be defined to compare the performance of photovoltaic devices from different manufacturers and research laboratories [18]. The standard spectra were refined in the early 2000's to increase the resolution and to co-ordinate the standards internationally.

In this research, a simulated AM 1.5 G illumination with a power density of 100 mW/cm^2 (shown in Fig. 2.16) was applied to characterize the fabricated DSSC.

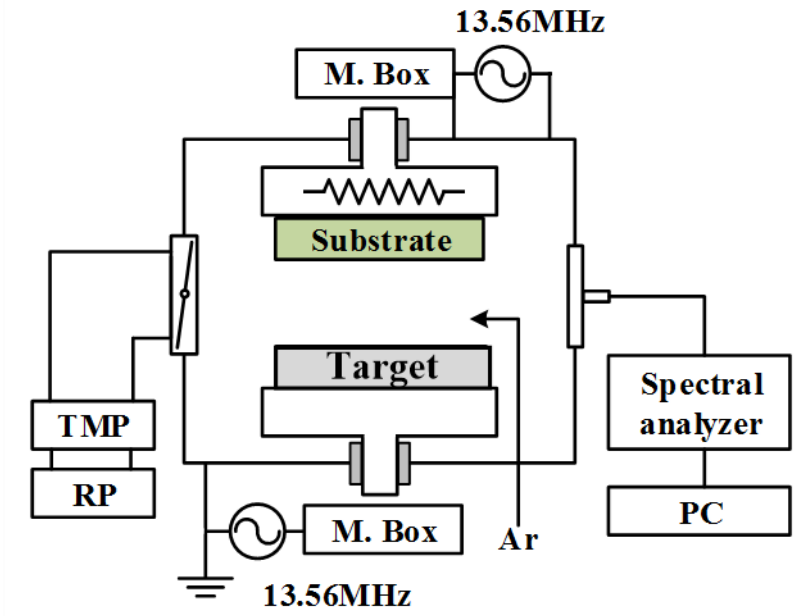

Fig. 2.1 The diagrammatic sketch of RF sputtering apparatus.

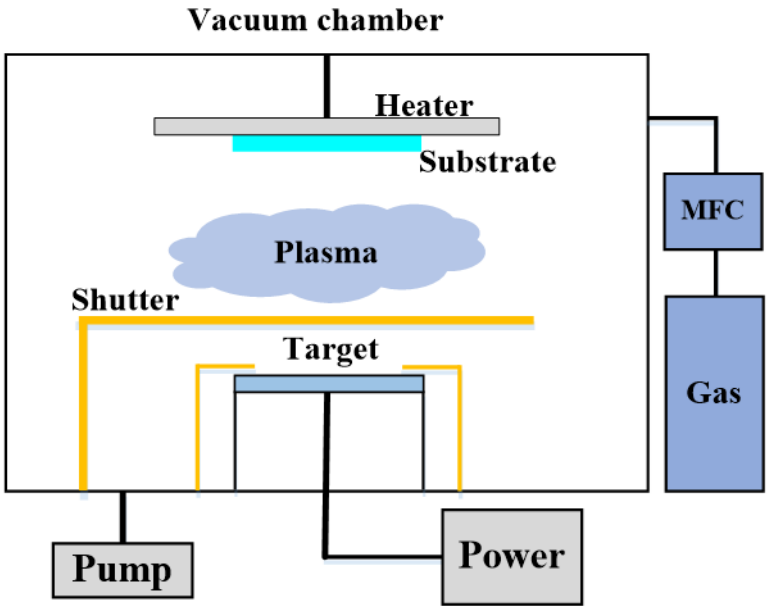

Fig. 2.2 The diagrammatic sketch of DC sputtering apparatus.

Fig. 2.3 A commercial annealing furnace.

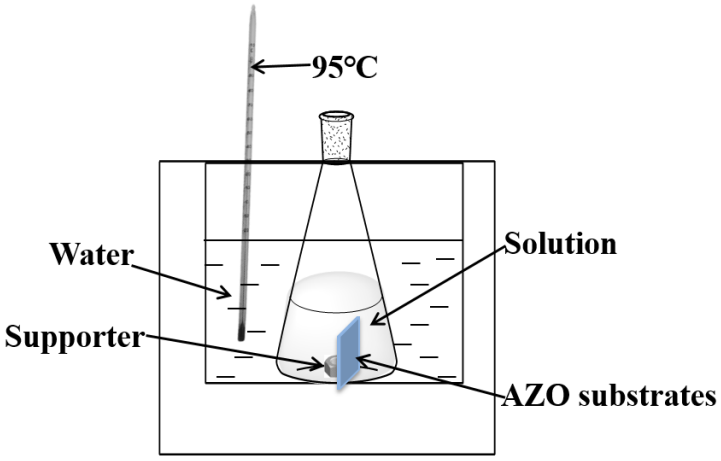

Fig. 2.4 The diagrammatic sketch of CBD apparatus.

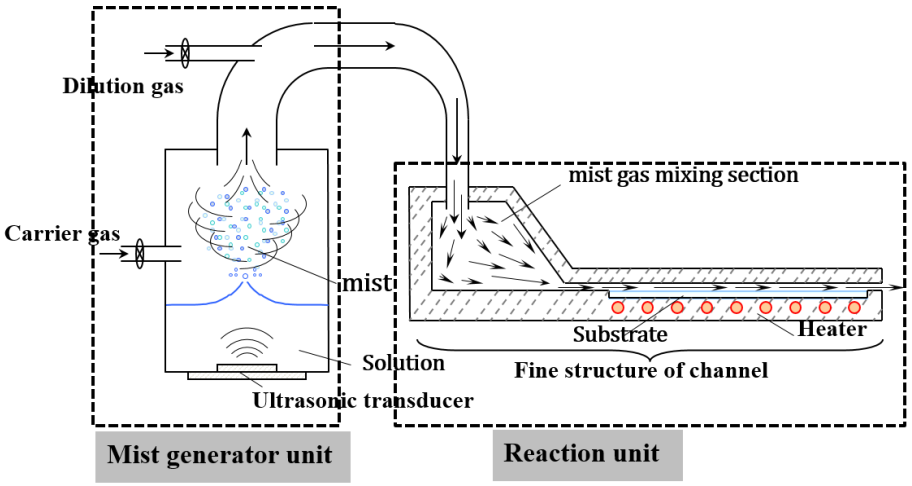

Fig. 2.5 The schematic diagram of mist CVD process [6].

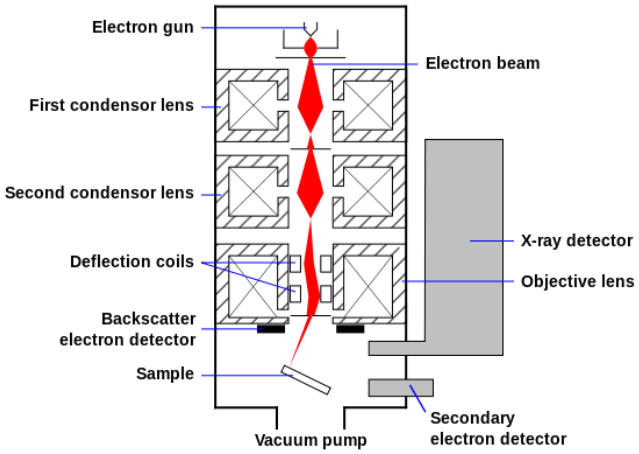

Fig. 2.6 The schematic image of SEM [7].

Fig. 2.7 FE-SEM instrument.

Fig. 2.8 TEM instrument.

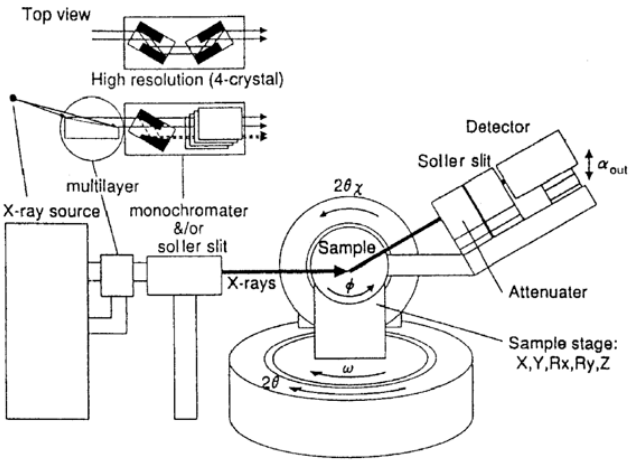

Fig. 2.9 The schematic diagram of XRD [11].

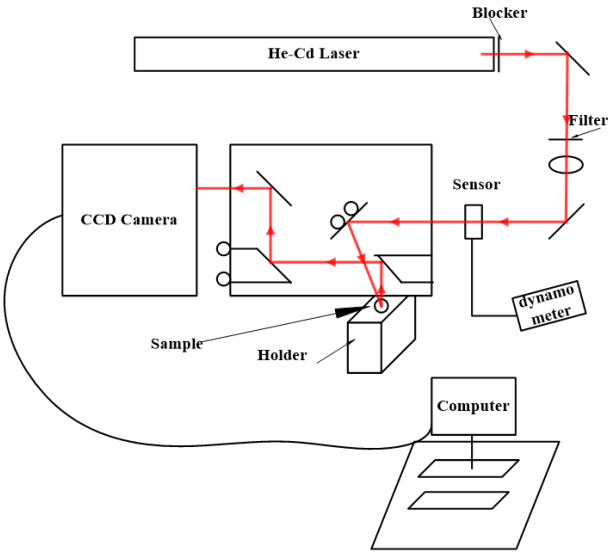

Fig. 2.10 The schematic diagram of PL spectroscopy measurement.

Fig. 2.11 Raman spectroscopy instrument.

Fig. 2.12 U-4100 UV-Vis-IR spectrophotometer.

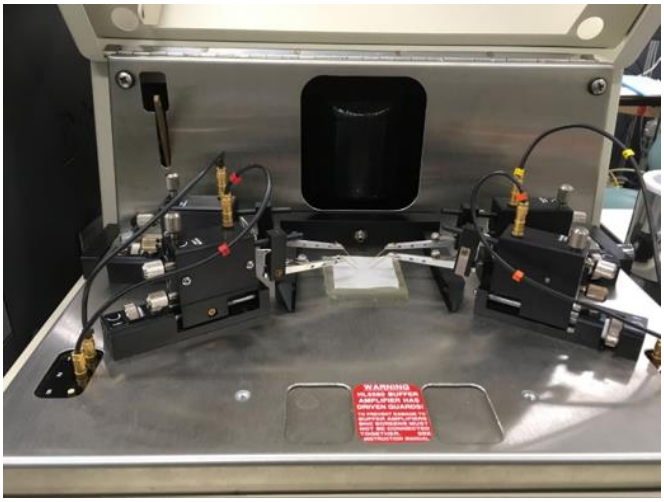

Fig. 2.13 Hall effect measurement system.

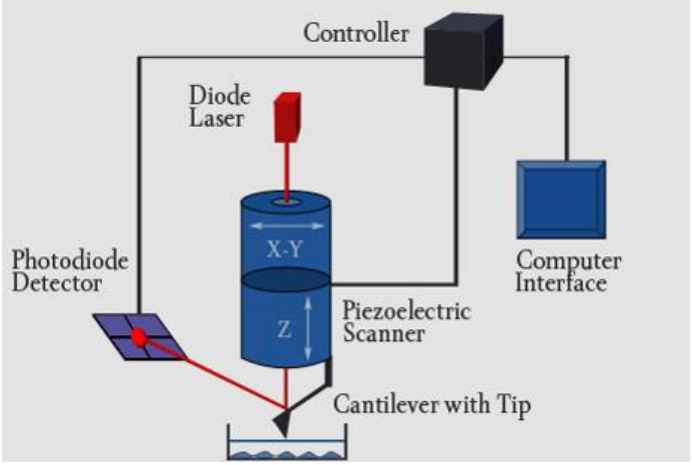

Fig. 2.14 The schematic diagram of AFM measurement [17].

Fig. 2.15 AFM instrument.

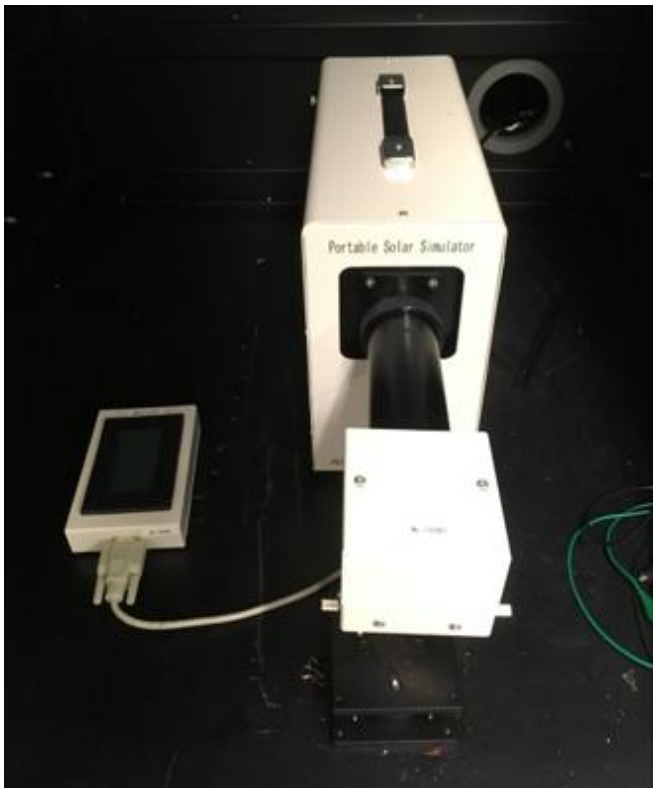

Fig. 2.16 AM 1.5G solar simulator.

2.4 References

[1] J.L. Vossen, and W. Kern. Thin film processes II. *Academic press, San diego,* (2012) 177-200.

[2] T. Matsuda, M. Furuta, T. Hiramatsu, H. Furuta, C. Li, and T. Hirao. *Appl. Surf. Sci.* 256 (2010) 6350-6353.

[3] J. Nomoto, M. Konagai, K. Okada, T. Ito, T. Miyata, and T. Minami. *Thin Solid Films,* 518 (2010) 2937-2940.

[4] C. Li, T. Kawaharamura, T. Matsuda, H. Furuta, T. Hiramatsu, M. Furuta, and T. Hirao. *Appl. Phys. Exp.* 2 (2009) 091601.

[5] B. Cao, and W. Cai. *J. Phys. Chem. C,* 112 (2008) 680-685.

[6] T. Kawaharamura, and S. Fujita. *Phys. Status Solidi c,* 5 (2008) 3138-3140.

[7] http://en.wikipedia.org/wiki/Scanning_electron_microscope.

[8] L.L. Yang, Dr. Thesis, Synthesis and characterization of ZnO nanostructures, *Linkoping-Univ. Sweden,* 2010.

[9] J.M. Jensen, A.B. Oelkers, R. Toivola, D.C. Johnson, J.W. Elam, and S.M George. *Chem. Mater.* 14 (2002) 2276-2282.

[10] J. Zhang, L. Sun, C. Liao, and C. Yan. *Chem. Comm.* (2002) 262.

[11] Advanced Thin film X-ray system-Grazing incidence in-plane diffractometer. *The Rigaku Journal,* 16 (1999) 53-58.

[12] G.D. Gilliland. *Mater. Sci. Eng. R-Rep.* 18 (1997) 99-399.

[13] D.T. Schwartz. Renishaw Raman Microscope (2010).

[14] S. Hong, T. Joo, W.I. Park, Y.H. Jun, and G.C. Yi. *Appl. Phys. Lett.* 83 (2003) 4157-4159.

[15] R. Green. *White paper,* 3111 (2011).

[16] G. Binnig, C.F. Quate, and C. Gerber. *Phys. Rev. Lett.* 56 (1986) 930-934.

[17] https://medicine.tamhsc.edu/afm/principles.php.

[18] http://www.pveducation.org/pvcdrom/appendices/standard-solar-spectra.

Chapter 3

Fabrication and characterization of ZnO nanorods by multi-annealing method

3.1 Introduction

In previous research, the vertical alignment of ZnO nanorods could not be controlled on ITO or FTO substrates [1-3]. Recently, some studies reported that ZnO-based substrates including aluminum doped ZnO (AZO) and gallium doped ZnO (GZO) had great potential to contribute to the alignment of ZnO nanorods [4-6]. However, good crystallinity and vertical alignment could not be realized by using ZnO-based substrates. Moreover, the mechanism of alignment of ZnO nanorods was still not clear. Therefore, the remained critical issue for ZnO nanorods applying in DSSC is how to achieve vertical alignment on TCO substrate.

Based on our previous research, we had succeeded in fabricating different conductive films by the sputtering system, as well as fabricating ZnO nanorods in different substrates by reducing annealing [7-10]. However, vertical alignment of ZnO nanorods were not well controlled. Based on our previous research [11], we found that lattice mismatch between ZnO film and substrate had significant influence on the alignment of ZnO nanorods. The low lattice mismatch contributed to the vertical alignment of ZnO nanorods. Therefore, in this chapter, ZnO based films including AZO and GZO films with good crystallinity and orientated (0001) direction were deposited to grow ZnO nanorods. Effects of metal dopants on structural and electrical properties of ZnO films were investigated. The mechanism of alignment of ZnO nanorods during reducing annealing process was discussed in details.

3.2 Deposition of transparent conductive AZO and GZO films

3.2.1 Effects of film thickness on the structural and electrical properties of AZO films

3.2.1.1 Experiments

Alkali-free glass sheets (Eagle XG, Corning Co. Ltd) were used as the substrates for deposition of AZO films. A conventional RF (13.56 MHz) magnetron sputtering system was applied to deposit AZO films with a 4-inch AZO ($ZnO : Al_2O_3$=98 : 2 wt%) ceramic target. The glass substrate was set 60 mm away from the target. During the sputtering process, pure argon

(30 sccm) was introduced as the working gas. The pressure and the temperature were maintained at 1Pa and 150 ℃ respectively. AZO films with different thicknesses (100, 150, 200, 250 and 300 nm) were deposited by controlling the deposition time. The deposition conditions were summarized in Table 3.1.

Table 3.1 Deposition conditions of AZO films with different thicknesses.

Film	Working gas	Temperature (˚C)	Pressure (Pa)	Power (W)
AZO	Ar (30 sccm)	150	1	60

3.2.1.2 Results and discussion

SEM images of AZO films were shown in Fig. 3.1. It was clearly seen that uniform surfaces were found from all as-deposited AZO films. The average grain size of as-deposited films increased from 32.6, 36.4, 57.2, 77.8 to 104.2 nm in sequentially as the AZO thickness increased from 100, 150, 200, 250 to 300 nm. As reported, the increasing grain size of thin films could be attributed to ion bombardment during sputtering process [12]. AZO film with small grains formed at the surface of glass substrate. As deposition time increased, argon ions bombarded the surface of AZO film with energies, resulting in that the small grains grew bigger.

Figure 3.2(a) revealed XRD patterns of AZO films with different thicknesses. It was found that all as-deposited AZO films exhibited a dominant (002) diffraction peak, which meant the preferentially oriented growth was in the (0001) orientation perpendicular to the substrate. As shown in Fig. 3.2(b), the intensity of (002) diffraction peak increased and full width at half maximum (FWHM) decreased with AZO film thickness increased, which meant that the crystallinity of AZO films was improved. The highest (002) diffraction peak intensity and narrowest FWHM were obtained from 300 nm-thick AZO film. Based on biaxial strain model, the compressive stress (σ) in AZO films could be expressed as [13]

$$\sigma = \frac{2C_{13}^2 - C_{33}(C_{11}+C_{12})}{2C_{13}} \times \frac{c_{film} - c_{bulk}}{c_{bulk}} \quad (3.1)$$

where c is the lattice constant, Cij is the elastic modulus of bulk ZnO films, and C_{11}=208.8 GPa, C_{12}=119.7 GPa, C_{13}=104.2 GPa and C_{33}=213.8 GPa. The (002) diffraction peak position varied from 34.36, 34.37, 34.37, 34.38 to 34.48°, which indicated that stress existed in the films. Because the peak position of AZO film was smaller than that of standard ZnO powder, the stress was identified as compressive stress. According to the calculated results shown in Fig. 3.3(a), compressive stress decreased from -0.73 to -0.35 GPa in parallel to the increase of AZO films thickness. According to Scherrer's equation [13], the c-axis crystallite size could be calculated using the FWHM value.

$$\tau = \frac{K\lambda}{\beta cos\theta} \tag{3.2}$$

where λ is the X-ray wavelength, θ is the Bragg angle of (002) diffraction peak, and β is the FWHM of (002) peak. Fig. 3.3(b) presented the variation of c-axis crystallite size of as-deposited AZO films with different thicknesses. It was found that c-axis crystallite sizes of AZO films increased from 24.9 to 31.0 nm as film thickness increased from 100 to 300 nm. The lattice constant c also could be calculated based on residential stress and XRD patterns. The lattice constant c of AZO film was relaxed to the lattice constant c (0.52 nm) of bulk ZnO as the thickness increased from 100 to 300 nm.

Figure 3.4 showed the optical transmittance of AZO films with different thicknesses. It revealed that the average optical transmittance of these films was nearly 80%, which meant AZO films were highly transparent in visible range. The commercial ITO glass exhibits average transmittance of around 83%, which was similar to the optical transmittance of AZO films.

The electrical properties of as-deposited AZO films were investigated due to the reason that they would serve as the conductive substrates in photovoltaics fabrication. Fig. 3.5 showed the resistivity, mobility, and carrier concentration of AZO films as a function of film thickness. As the thickness of AZO film increased, the resistivity decreased significantly, while mobility increased and carrier concentration increased. The reason why carrier concentration in AZO films increased was because more aluminum atoms were doped in AZO films, which introduced more free electrons for transportation.

The density function theory (DFT) was applied to simulate the equillium position of aluminum doped ZnO film. In DFT calculation, the calculation of many-electron wavefunction exceed any computational capabilities by far. However, this problem can be overcome using the Kohn-Sham (KS) ansatz, in which the fully-interacting system is replaced by a non-interacting one. Applying KS ansatz, the single-particle Schrödinger equation was transformed into Kohn-Sham equation in DFT, which shown in Equation 3.3 [14].

$$\left[-\frac{1}{2}\nabla^2 + v_{eff}(r)\right]\varphi_i = \varepsilon_i\varphi_i \tag{3.3}$$

This equation included an effective potential $v_{eff}(r)$, which was produced by the Coulomb forces of all other electrons and nuclei and incorporates the exchange and correlation interactions, shown in Equation 3.4.

$$v_{eff}(r) = V_{en}(r) + \int \frac{\rho(r')}{|r-r'|}dr' + V_{xc}(r) \tag{3.4}$$

However, the exchange and correlation interactions, which was the complicated part of physics, could not be calculated exactly. The above eigen-value problem was solved using an iterative method that makes up the computationally expensive step of the DFT calculations. A

schematic representation of a self-consistent loop in this numerical method was depicted in Fig. 3.6. With the forces at hands, the energy of a configuration can be minimized with respected to the atomic coordinates. Mathematically, this corresponds to finding the stationary point of a function whose exact form is generally unknown. Iterative methods was employed to solve this mathematical calculation. The obtained energy minima corresponds to the stable configurations, which are physically realized and thus important for the determination of stable defect configurations.

The calculation in this research was based on the Abinit [15]. Abinit was an open-source suite of programs for materials science whose main program allows one to find the total energy, charge density and electronic structure of systems made of electrons and nuclei (molecules and periodic solids) within Density Functional Theory. In this calculation, a 2×2×3 ZnO supercell with 48 zinc atoms and 48 oxygen atoms is constructed. One zinc atom was replaced with one aluminum atom in 48 zinc atoms, which meant the aluminum dopping concentration was 2.08 wt%. During our calculations, projector augmented wave (PAW) pseudo-potentials were used to describe the interactions between the atomic nucleus and valence electrons [16]. The local density approximation (LDA) was used to describe the exchange–correlation energy among electrons, and a 4×4×8 kpoint mesh was employed for the Brillouin zone integration of the 48-atom supercell. The energy cutoff was 420 eV, which had been confirmed to be large enough. The breaking condition for ionic relaxation in total energy was 10^{-5} eV.

The calculated cell lattice constants were shown in Fig. 3.7. Lattice constants in this research were a = b = 0.3254 nm and c = 0.5212 nm, which were in very small lattice deviation with both the experimental values and bulk ZnO values. The calculation lattice deviation of a and c with those of bulk ZnO were 0.11% and 0.12%, respectively. The calculated lattice constant c also showed very low deviation from the experimental data (0.5209 nm) of 300 nm-thick AZO film. It meant the lattice constants was very close to the bulk ZnO after doping with aluminum. It can be attributed to the small radius deviation betweeen Al (0.118 nm) and Zn (0.125 nm).

The lattice constant c and compressive stress of AZO film and ZnO film with thickness of 300 nm was calculated based the XRD patterns. The calculated compressive stress of AZO film (-0.5 GPa) was much lower than that of ZnO film (-1.5 GPa). The lattice constant c of AZO film was 5.209 nm, which was much closer to that of bulk ZnO. However, ZnO film showed a lattice constant c of 0.5223 nm. Therefore, it was proven that aluminum doping improved the crystallinity of ZnO film and reduce the compressive stress of ZnO film.

Low resistivity of 5.60×10^{-4} Ω•cm and high mobility of 15.0 $cm^2/(V•s)$ were found from the fabricated 300-nm-thick AZO film, which was comparable to commercial ITO (resistivity and mobility is 10^{-4} Ω•cm and 20 $cm^2/(V•s)$ respectively) [17]. Therefore, AZO films can be alternative substrates using as transparent conductive substrates.

3.2.1.3 Summary

AZO films were deposited on glass substrate by RF magnetron sputtering. The thickness of AZO film had a significant influence on morphological, structural, optical and electrical properties on AZO films. It was found that grain size increased, crystallinity of AZO films improved while resistivity decreased and mobility increased as the thickness increased. AZO films with different thicknesses showed high transmittance of 80% in visible range. Calculated lattice constants of AZO film were in good agreement with experimental values. Aluminum doping could improve the crystallinity of ZnO film. 300 nm-thick AZO film showed good crystallinity, high transmittance and comparable resistivity and mobility to ITO substrate, which would be the suitable substrate for photovoltaic application.

3.2.2 Effects of film thickness on the structural and electrical properties of GZO films

3.2.2.1 Experiments

GZO films were deposited on alkali-free OA-10 glass (Eagle XG, Corning Co. Ltd) using a conventional DC sputtering system. A 4-inch GZO ($ZnO : Ga_2O_3 = 94.3 : 5.7$ wt%) target was set 80 mm away from the glass substrates. The temperature of 150 ˚C was preheated for one hour before deposition and kept during deposition. Argon (30 sccm) was introduced as the working gas and the pressure was maintained at 1 Pa. The deposition power was set at 150 W. GZO films with different thicknesses of 100, 150, 200, 250 and 300 nm was deposited. The deposition conditions were shown in Table 3.2.

Table 3.2 Deposition conditions of GZO films with different thicknesses.

Film	Working gas	Temperature (˚C)	Pressure (Pa)	Power (W)
GZO	Ar (30 sccm)	150	1	150

3.2.2.2 Results and discussion

AFM images of GZO films were shown in Fig. 3.8. The average root mean square (RMS) roughness of GZO films was calculated in a scan area of 2×2 μm^2. It was found that the uniform surface was found on all the GZO films. The rms roughness of GZO films were 1.10, 1.23, 1.80, 1.95 and 2.56 nm in the order of 100, 150, 200, 250 and 300 nm in thickness.

XRD patterns of GZO films with different thicknesses were shown in Fig. 3.9(a). It revealed

that all the as-deposited GZO films exhibited only one (002) diffraction peak, indicated that GZO films had a preferred c-axis orientation growth. It was found that as the thicknesses of GZO film increased, the intensity of (002) peak increased and FWHM decreased significantly from 0.278° to 0.234°, which shown in Fig. 3.9(b). It was related to an improvement in the crystallinity. The 300-nm-thick GZO film showed the highest intensity of (002) peak and the smallest FWHM, which meant it had the best crystallinity.

The (002) diffraction peak position of GZO films were 34.29, 34.36, 34.38, 34.40 and 34.41° corresponding to the thickness of 100, 150, 200, 250 and 300 nm, as shown in Fig. 3.10(a). The deviation of peak position indicated compressive stress existed in the films. The compressive stress of GZO films could be calculated based on Equation 3.1. Compressive stress in GZO films were -1.89, -1.18, -0.83, -0.68 and -0.24 GPa in the order of film thickness from 100 to 300 nm. Therefore, the decreased compressive stress indicated the crystallinity became better.

Based on Equation 3.2, c-axis crystallite size could be calculated. It was obtained that c-axis crystallite size of GZO films also increased from 24.31, 27.06, 28.83, 29.77 to 30.21 nm corresponding to the GZO film thickness of 100, 150, 200, 250, and 300 nm respectively, as shown in Fig. 3.10(b). Z. You et. Al [18] reported that Ga atoms substitute Zn in the hexagonal structure and Ga may occupy the interstitial sites of ZnO or Ga possibly segregates to the non-crystalline region in grain boundaries, then formed the Ga-O bond. The ionic radius of Ga^{3+} (0.62 Å) was smaller than that of Zn^{2+} (0.74 Å), which meant Ga^{3+} was easier to replace Zn^{2+}. Moreover, the covalent band length of Ga-O (1.92 Å) was 5.0% shorter than that of Zn-O (1.97 Å) and the bonding energy of Ga-O was higher than that of Zn-O, which indicated the bonding between Ga-O was stronger than that of Zn-O [19]. As the thickness of GZO films increased, more Ga atoms substituted the sites of Zn atoms, thus resulting in reducing the compressive stress among crystallite size. This may be one of the reasons for GZO films performed good crystallinity. As well known, bigger c-axis crystallite size for ZnO thin film have better crystallinity. The increasing crystallite size of GZO films resulted in increasing crystallinity for GZO films. Furthermore, the calculated lattice constant c decreased from 5.22 to 5.20 Å, which also confirmed the increased crystallinity.

Figure 3.11 showed the optical transmittance spectra of GZO films with different thicknesses. It revealed all as-deposited GZO films showed clear and smooth curves with interference fringe patterns. It indicated the surface of as-deposited GZO films was smooth and uniform. The average optical transmittance of these films in visible range (380 nm-760 nm) was nearly 80%. In terms of the effects of the thickness of GZO films, the average optical transmittance was similar, which meant the film thickness had little influence on the transparency of GZO films in visible light range.

The resistivity, carrier concentration, and carrier concentration of sputtered GZO films were measured by the Hall Effect measurement. Fig. 3.12 showed resistivity, Hall mobility and carrier concentration of GZO films. It was found that the resistivity decreased, Hall mobility increased, and carrier concentration increased significantly with increasing thickness of GZO films. The lowest resistivity of 3.96×10^{-4} Ω•cm, the highest Hall mobility of 16.3 $cm^2/(V•s)$, and the highest carrier concentration of -1.608×10^{21} cm^{-3} were obtained from the GZO film with the thickness of 300 nm.

As widely known, GZO film is one of metal doped n-type semiconductor materials. During the DC sputtering process, more gallium atoms were substituted at zinc sites in films with the thickness increased, resulting in the increase in the concentration of free electrons in GZO films. Therefore, carrier concentration of GZO films increased and resistivity decreased.

The DFT calculation was also performed in gallium doped ZnO films. A 3×3×3 ZnO supercell with 108 zinc atoms and 108 oxygen atoms. Due to the different doping concentration in ZnO film, 6 zinc atoms were replaced with gallium atoms in 108 zinc atoms, which meant the gallium dopping concentration was 5.56 wt%. a 6×6×8 kpoint mesh was employed for the Brillouin zone integration of the 108-atom supercell. The energy cutoff was 840 eV, which had been confirmed to be large enough.

Figure 3.13 showed the total energy as a function of lattice constant. It was clearly seen that the total energy reached the minimum at lattice constants a = 0.3251 nm and c = 0.5208 nm, which were in very small lattice deviation with both the experimental values and bulk ZnO values. The calculation lattice deviation of a and c with those of bulk ZnO were 0.02% and 0.04%, respectively. The lattice deviation between GZO and bulk ZnO was much smaller than that between AZO and bulk ZnO. The calculated lattice constant c also showed very low deviation from the experimental data (0.5207 nm) of 300 nm-thick GZO film. It meant the lattice constants of GZO were very close to those of the bulk ZnO after doping with gallium. The radius of gallium atoms was 0.126 nm, which was much closer to that of Zn (0.125 nm).

The calculated compressive stress of GZO film (-0.3 GPa) was much lower than that of ZnO film (-1.5 GPa). The lattice constant c of GZO film and ZnO film was 5.2070 nm and 5.2223 nm, respectively. which meant lattice constant c of GZO was much closer to that of bulk ZnO. Therefore, aluminum doping improved the crystallinity of ZnO film and reduced the compressive stress of ZnO film. Compared with aluminum doping in ZnO, gallium doping exhibited much lower compressive stress. Therefore, gallium doping exhibited a better improvement in crystallinity of ZnO film than aluminum doping.

According to the above results, 300 nm-thick GZO film exhibited the electrical resistivity of 3.96×10^{-4} Ω•cm and high optical transmittance of 85% in visible range, which were comparable to those from commercial ITO substrate (the resistivity and optical transmittance are 3×10^{-4}

Ω•cm, and 83% respectively) produced by Sigma-Aldrich Co. Ltd.

3.2.2.3 Summary

GZO films were deposited on glass substrates by DC magnetron sputtering system. The morphological, structural, optical and electrical properties of GZO films were greatly affected by the thickness. As thickness increased, surface roughness increased as well as the crystallinity of GZO film increased. The resistivity of GZO film decreased significantly and mobility increased with thickness increased. Gallium doping significantly improved the crystallinity of ZnO film. GZO film with thickness of 300 nm showed comparable resistivity, mobility and transmittance to commercial ITO substrate. Therefore, GZO film could be used as the TCO substrate for DSSC.

3.3 Fabrication of ZnO nanorods by multi-annealing method

3.3.1 Substrate effects on the the structural and electrical properties of ZnO nanorods

3.3.1.1 Experiments

ZnO films were deposited on AZO, GZO and ITO substrates. AZO and GZO films were prepared according to the expriments described in 3.2.1 and 3.2.2. ITO films were deposited on glass substrates by DC sputtering method. These three films were deposited in same thickness of 300 nm. ZnO thin film was deposited by a conventional 13.56 MHz RF magnetron sputtering system. The deposition process was performed in an Ar ambient (30 sccm). The pressure and RF power were maintained at 7 Pa and 150 ℃ respectively. The deposition conditions were shown in Table 3.3. The obtained ZnO films were put into a conventional annealing furnace. A multi-annealing process was carried out in forming gas (H_2 : N_2 = 1 : 96 %) firstly at 300 ˚C for 2 hours in order to increase the density of zinc seeds on the surface. Secondly, the temperature was increased to 450℃ and kept for 3 hours in forming gas ambient to produce the ZnO nanorodss. Due to lack of oxygen during the reaction, the oxygen was introduced into the furnace for 40 minutes before the second forming gas annealing process. For safety consideration, N_2 was introduced for 5 minutes between forming gas and oxygen annealing processes. The mutli-annealing process was shown in Fig. 3.14.

Table 3.3 Deposition conditions of ZnO film on AZO, GZO and ITO.

Film	Working gas	Temperature (˚C)	Pressure (Pa)	Power (W)
ZnO	Ar (30 sccm)	150	7	180

3.3.1.2 Results and discussion

Figure 3.15 showed the SEM images of ZnO nanorods grown on AZO, GZO and ITO substrates. It was clearly that ZnO nanorods grown on AZO and GZO films were vertical aligned while those on ITO films were not vertical aligned. ZnO nanorods grown on all these substrates showed hexagonal structures. However, ZnO nanorods grown on AZO and GZO substrates showed much bigger diameter than those grown on ITO. The diameter of ZnO nanorods were 80, 201 and 192 nm corresponding to ITO, AZO and GZO substrates. The length of ZnO nanorods were 1.125, 1.407 and 1.427 μm in the order of ITO, AZO and GZO substrates, which meant ZnO nanorods grown on AZO and GZO had a bigger length than those on ITO substrate. The diameter, density and length of ZnO nanorods were summarized in Table 3.4.

Table 3.4 Diameter, density and length of ZnO nanorods on ITO, AZO and GZO.

Substrates	Diameter (nm)	Density (/μm^2)	Length (nm)
ITO	80	8	1125
AZO	201	12	1407
GZO	1125	12	1427

XRD patterns of ZnO nanorods grown on ITO, AZO and GZO substrates were shown in Fig. 3.16. It exhibited that a dominant (002) diffraction peak was found for ZnO nanorods grown both on AZO and GZO substrates, which meant ZnO nanorods preferentially grew along (0001) orientation on AZO and GZO substrates. However, ZnO nanorods grew on ITO substrate showed no visible diffraction peak, indicating poor growth direction for ZnO nanorods.

PL spectra of ZnO nanorods grown on different substrates were shown in Fig. 3.17. It was found that ZnO nanorods grown on different substrates showed a UV emission centered at 378 nm and a strong visible emission centered at 492 nm. Intensities of both visible emission and UV emission were increased in the order of ITO, AZO and GZO, which indicated that both optical crystallinity and oxygen vacancies were increased. SEM images showed the density of ZnO nanorods on ITO was less than those on AZO and GZO, resulting in both intensities of UV emission and visible emission decreased. Although ZnO nanorods grown on AZO and GZO showed similar morphological and structural properties, the UV intensity of ZnO nanorods on GZO was much higher than that on AZO. It could be attributed to the longer length for ZnO nanorods on GZO.

Figure 3.18 showed that transmittance spectra of ZnO nanorods fabricated on different substrates. Because of the vertical alignment of ZnO nanorods on AZO and GZO films, they

showed high transmittance of 60%, which was much higher than those on ITO (40%) in visible range. However, the reason of vertical alignment of ZnO nanorods should be investigated.

Figure 3.19 showed the comparison of XRD patterns between GZO film, ZnO film deposited on GZO, and ZnO nanorods on GZO. The only (002) diffraction peak was found for GZO film, ZnO film and ZnO nanorods. ZnO film and nanorods exhibited much stronger intensity of (002) diffraction peak than as-deposited GZO film, indicating that ZnO film and nanorods had much better c-axis orientation growth. The lattice constant c of GZO film and ZnO film was 0.52069 nm and 0.52046 nm respectively, demonstrating the very low lattice mismatch of 0.048% between GZO and ZnO films. The lattice mismatch between ZnO nanorod and ZnO film was 0.035%, which was smaller than that of GZO and ZnO films.

Figure 3.20 showed the FE-SEM images of GZO film, ZnO film deposited on GZO film and ZnO nanorodss fabricated on GZO film. It can be observed that column-structured grains were present for as-deposited GZO film and ZnO film, indicating the as-deposited films would preferentially grow along the c-axis. According to XRD analysis, GZO film showed c-axis orientation growth. Because of the very low lattice mismatch between ZnO film and GZO film, the deposited ZnO film kept the same direction with respect to GZO film.

After the multi-annealing process, as shown in Fig. 3.20(c-1) and (c-2), uniform and well-aligned ZnO nanorodss on GZO substrate were observed. The diameter, density and length of ZnO nanorodss were 145.8 nm, 31 /μm^2 and 1.427 μm respectively.

In order to confirm the relationship between the growth direction of ZnO nanorods and as-deposited GZO film, TEM measurement was performed. Fig. 3.21 shows the TEM images of ZnO nanorodss and selected area electron diffraction patterns of four different regions including ZnO nanorods, the interface between ZnO nanorods and ZnO film, the interface between ZnO film and GZO film, and GZO film. The diffraction patterns showed these four regions had wurtzite crystal structure and the same (0001) orientation, indicating that the orientation of ZnO nanorods was dependent on that of underlying as-deposited GZO film.

The mechanism why ZnO nanorods were vertical aligned could be attributed to the growth process during reducing annealing. As reported in our previous research [9,20], the growth of ZnO nanorodss during the reducing annealing process might be attributed to the vapor-solid and vapor-liquid-solid mechanism. ZnO film was reduced by hydrogen to zinc and H_2O, as shown in the following reaction:

$$ZnO + H_2 \rightarrow Zn + H_2O \quad (3.5)$$

The reduced zinc atoms only existed at the original positions where they were reduced when the annealing temperature was lower than the melting point of zinc (419.58 ˚C). When the temperature was greater than 419.58 ˚C, the reduced zinc atoms melted and moved easily on ZnO film, and the reaction rate increased as well. Also, because ZnO film were deposited in the

atmosphere of argon, some unoxidized zinc remained in the film. These zinc could also move on surface of ZnO film. The reduced zinc would formed into ZnO based on the following equations:

$$H_2O \rightarrow H^+ OH^- \quad (3.6)$$

$$Zn + 2OH^- \rightarrow Zn(OH)_2 \rightarrow ZnO + H_2O \quad (3.7)$$

Water was ionized at high temperature of 450 ˚C. Reduced zinc atoms reacted with ionized water and formed $Zn(OH)_2$. $Zn(OH)_2$ was highly unstable and easily dehydrated into ZnO [21]. According to XRD results, ZnO film/GZO was highly oriented in the (0001) orientation. It is well known that (0001) orientation is the preferential growth direction for wurtzite ZnO [22]. Therefore, dehydrated ZnO tended to grow in the same (0001) direction as the underneath GZO film due to the minimum energy principle, which was called ZnO recrystallization growth. Therefore, ZnO nuclei with very good (0001) orientation growth would form on the surface. Then the formed ZnO nanocrystal would bond to ZnO nuclei to form ZnO nanorods. Because recrystallization rate in (0001) orientation was much faster than those in other orientations, the growth rate of ZnO nanorodss in longitudinal direction was much faster than that in transverse direction. As annealing time increased, ZnO nanorodss would grow vertically to the substrate. Therefore, vertical alignment of ZnO nanorodss was realized by annealing method.

In addition, both hydrogen reduction of ZnO film and recrystallization of ZnO nanorodss occurred at the same time during reducing annealing. In order to obtain bigger ZnO nanorodss, the recrystallization rate must be controlled with the balance of the reduction reaction rate. During reducing annealing, the reducing process could be continuously carried out due to the continuous supplement of hydrogen. Because of lack of oxygen during reducing annealing process, oxygen vacancies formed and some zinc could not be oxidized, which would cause the crystallinity worse and growth rate of ZnO nanorod growth slower. Therefore, it was necessary to supply oxygen periodically to the furnace between every two reducing annealing steps.

3.3.1.3 Summary

Vertical alignment of ZnO nanorods was obtained by multi-annealing method on AZO and GZO substrates. It was found that the vertical alignment of ZnO nanorod was dependent on the crystallinity of subtrates. ZnO film and ZnO nanorods followed the same growth orientation of AZO and GZO films. Low lattice mismatch between ZnO film and GZO film contributed to good c-axis growth of ZnO film, further contributing to the vertical alignment of ZnO nanorods. The vertical alignment of ZnO nanorods contributed to the high transmittance of ZnO nanorods.

3.3.2 Effects of oxygen annealing on the structural and optical properties of ZnO nanorods

3.3.2.1 Experiments

The double layers including 500 nm-thick ZnO thin film on 300 nm-thick AZO substrate was deposited by a conventional 13.56 MHz RF magnetron sputtering system to investigate oxygen annealing effects. The deposition conditions were interpreted in last section. The obtained ZnO/AZO was put into a conventional furnace. A multi-annealing process was performed to fabricate ZnO nanorods. Forming gas was introduced into the annealing furnace and the temperature was kept at 300 ˚C for 2 hours. Then the temperature increased to 450 ˚C and kept for 3 hours. After reducing annealing, the oxygen annealing was introduced to investigate the oxygen annealing effects on the ZnO nanorods. The oxygen was introduced in the furnace and kept for 40 minutes. For safety consideration, N_2 was introduced in the furnace for 5 minutes between forming gas and oxygen annealing processes. The annealing processes were shown in Fig. 3.22.

3.3.2.2 Results and discussion

ZnO nanorods before and after oxygen annealing was compared to investigate the annealing effects. SEM images of ZnO nanorods before and after oxygen annealing were shown in Fig. 3.23. It was observed that there were small ZnO nanorods were vertically fabricated on ZnO films after reducing annealing. The diameter and length of ZnO nanorods were 75 nm and 109 nm respectively. Comparing the morphologies of ZnO nanorods before and after oxygen annealing, the difference on the morphology including diameter, length and density was not obvious, which meant oxygen annealing had no visible effects on (oxygen annealing) the growth of ZnO nanorods.

However, observing from XRD patterns, as shown in Fig. 3.24, the slightly higher intensity of (002) diffraction peak was obtained from ZnO nanorods after oxygen annealing than those before oxygen annealing. It was also found the (002) diffraction peak was slightly higher angle shift, which indicated the stress was relaxed after oxygen annealing. Therefore, the crystallinity of ZnO nanorods was improved after oxygen annealing.

The photoluminescence properties of ZnO nanorods were significantly influenced by oxygen annealing, as shown in Fig. 3.25. A strong UV emission peak and a strong blue-green emission peak centered at 380 nm and 491 nm respectively were observed from ZnO nanorods for both ZnO nanorods before and after oxygen annealing. The blue-green emission was decreased significantly while the UV peak was enhanced after oxygen annealing process. It is well-known

that the UV emission was attributed to the exciton emission and the blue-green emission was due to the oxygen vacancies. Therefore, it assumed that the oxygen vacancies were reduced after the oxygen annealing process due to the oxidization of the zinc atoms. Because the oxygen vacancies were reduced by oxidization, which formed more ZnO, enhancing the UV emission.

Optical transmittance of ZnO nanorods before and after oxygen annealing which was shown in Fig. 3.26 showed no much difference. It was found that the transmittance was slightly increased due to less defects and better crystallinity after oxygen annealing.

The oxygen annealing process had significant influence on the properties of ZnO nanorods. Due to the good (0001) orientation growth of ZnO and GZO films, ZnO nanorods would follow the same (0001) orientation, which was verified by the vertical growth of ZnO nanorods. During reducing annealing process, ZnO nanorods were formed in the ambinent which was lack of oxygen. Therefore, some zinc could not be oxidized during recrystallization, forming oxygen vacancies. Oxygen vacancies were existed in both surface and inside of ZnO nanorods. After oxygen annealing, some oxygen vacancies could be oxidized and disappeared, which resulted in better crystallinity and enhancing the UV emission. Due to less oxygen vacancies, the blue-green emission was weakened.

Due to the lack of oxygen during the reducing annealing, it was difficult to keep the balance between reduction and oxidization processes. Therefore, it was necessary to supply the oxygen to further increase ZnO nanorods growth after reducing annealing.

3.3.2.3 Summary

Structural and optical properties of ZnO nanorods were influenced by oxygen annealing. Crystallinity of ZnO nanorods was improved after oxygen. The photoluminescence property was influenced significantly with oxygen annealing. The UV emission was enhanced and the blue-green emission was weakened, which was attributed to the less oxygen vacancies and better crystallinity. The transmittance was slightly improved after oxygen annealing because less oxygen vacancies existed in ZnO nanorods.

3.3.3 Effects of annealing time on the structural and optical properties of ZnO nanorods

3.3.3.1 Experiments

ZnO thin film with thickness of 500 nm was deposited on AZO film by a conventional 13.56 MHz RF magnetron sputtering system using 4-inch ZnO (5N) target. Ar (30 sccm) was introduced in the ambient as working gas. The pressure and RF power were maintained at 7 Pa

and 150 ℃ respectively. The obtained ZnO/AZO (500 nm-thick ZnO on 300 nm-thick AZO) was put into a conventional furnace. A multi-annealing process was carried out in order to obtain ZnO nanorods. Firstly, forming gas (FG) (1.96% H_2 in N_2) was introduced in the furnace at 300 ˚C for 2 hours. Then the temperature was increased to 450 ˚C and kept for 3 hours. This annealing process of 5 hours was called preliminary annealing (PA). Secondly, oxygen was introduced into the furnace for 40 min before the second forming gas annealing for two hours, which was defined as circle 1. Continuously, the same circle was repeated twice. For safety consideration, N_2 was introduced in the furnace for 5 minutes between every forming gas and oxygen annealing processes. The annealing processes were shown in Fig. 3.27.

3.3.3.2 Results and discussion

Figure 3.28 showed the SEM images of ZnO nanorods after 4 different annealing processes. ZnO nanorods showed highly vertical alignment on AZO substrates. It was found that both the diameter and the length of ZnO nanorods increased with annealing processes increased. The diameter of ZnO nanorods increased from 75, 80, 142, to 196 nm corresponding to PA, 1 circle, 2 circles and 3 circles respectively. Moreover, the length of ZnO nanorods increased from 310 to 1427 nm. After 3 circles annealing, all of ZnO film was almost reduced completely by hydrogen.

Table 3.5 Diameter, density and length of ZnO nanorods by different annealing processes.

	PA	1 circle	2 circles	3 circles
Diameter (nm)	75	80	142	196
Density (/μm^2)	8.0	8.6	13.1	11.8
Length (nm)	109	310	627	1407

Figure 3.29 showed the XRD patterns of ZnO nanorods after the multi-annealing process. XRD patterns exhibited only (002) diffraction peak for ZnO nanorods, which confirmed ZnO nanorods grew along (0001) orientation The intensity of (002) diffraction peak increased and the FWHM decreased, indicating the crystallinity became better with annealing circles extended. It was also found that the peak position was slightly higher angle-shifted, which was due to the nanorods growth while the ZnO film reduced.

Figure 3.30 showed the PL spectra of ZnO nanorods after PA, 1 circle, 2 circles and 3 circles annealing. It was found that the two emission peaks centered at 380 nm and 491 nm were both enhanced with the annealing cycles. As annealing steps increased, the intensities of both UV emission and blue-green emission increased, indicating that better optical crystallinity and more

oxygen vacancies were introduced into the nanorods. However, comparing to the visible/UV ratio, it was found that the visible emission peak was increased much stronger than UV peak, which meant that the ratio of oxygen vacancies was increased quickly.

Optical transmittance curves of ZnO nanorods by different annealing circles were shown in Fig. 3.31. Optical transmittance of ZnO nanorods was decreased from 80% to 65% after three circles annealing, which might be due to the much oxygen vacancies inside of ZnO nanorods and also slightly remained ZnO films.

3.3.3.3 Summary

Multi-annealing process had significant influence on the ZnO nanorod growth. ZnO nanorods kept the c-axis growth orientation during annealing. As annealing process increased, diameter and length of ZnO nanorods were greatly increased as well as the crystallinity was improved. ZnO nanorods exhibited a UV emission and a strong blue-green emission peak. The intensities of both UV emission and visible emission increased as annealing process extended. Optical transmittance of ZnO nanorods was decreased from 75% to 55%.

3.4 Conclusions

In this chapter, ZnO-based electrodes were fabricated on transparent conductive AZO or GZO films as TCO substrate.

1) The transparent conductive AZO and GZO films were deposited by sputtering method. As thin film thickness increased, the grain size and the crystallinity of AZO films were both increased. Mobility increased and resistivity decreased significantly with thickness of AZO film increased. GZO film showed similar tendency with AZO film as film thickness increased. AZO and GZO films showed strongly c-axis growth direction. Aluminum and gallium doping significantly improved the crystallinity of ZnO films. Both films showed high transmittance of over 80% in visible range. AZO and GZO films with thickness of 300 nm showed comparable mobility and resistivity to commercial ITO films. Therefore, both films could replace ITO substrate to be applied as the TCO substrates for electrodes in DSSC.

2) ZnO nanorods were fabricated on ITO, AZO and GZO substrates by multi-annealing method. ZnO nanorods fabricated on AZO and GZO films were vertical aligned while those on ITO were not. The diameter of ZnO nanorods on AZO and GZO was much bigger than that on ITO. ZnO nanorods on AZO and GZO preferentially grew along c axis orientation while those on ITO grew randomly. Due to AZO and GZO had good c axis growth, ZnO nanorods followed the same growth direction to the underneath AZO and GZO films. Low mismatch between ZnO

film and AZO or GZO film contributed to vertical alignment of ZnO nanorods. Therefore, vertical alignment of ZnO nanorods could be obtained on AZO and GZO films by multi-annealing method.

3) Oxygen annealing affected the structural and optical properties of ZnO nanorods. It was found that crystallinity, PL spectra and optical transmittance of ZnO nanorods were significantly influenced by oxygen annealing. After oxygen annealing, the crystallinity was improved, UV emission was enhanced, the blue-green emission was weakened, and optical transmittance was slightly improved.

4) Multi-annealing process had significant effects on the ZnO nanorod growth. Vertical aligned ZnO nanorods were obtained during annealing. Diameter and length of ZnO nanorods were greatly increased with annealing process increased. The crystallinity was also improved. The intensities of both UV emission and visible emission were increased as annealing process extended.

ZnO based electrodes showed low resistivity of 5.60×10^{-4} Ω•cm, high mobility of 15.0 $cm^2/(V•s)$ and high optical transmittance of 55% in visible range, which would be fabricated into DSSC.

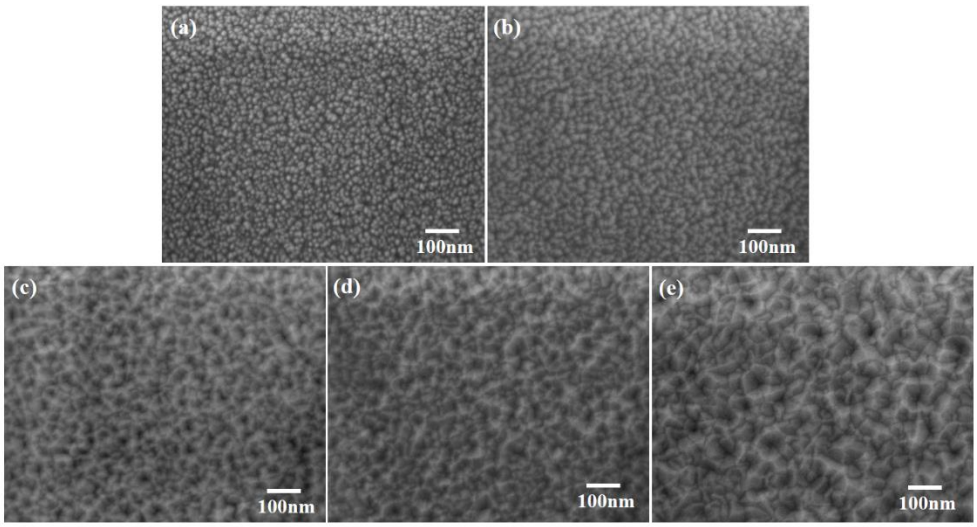

Fig. 3.1 SEM images of AZO films with thickness of (a) 100 nm, (b) 150 nm, (c) 200 nm, (d) 250 nm and (e) 300 nm.

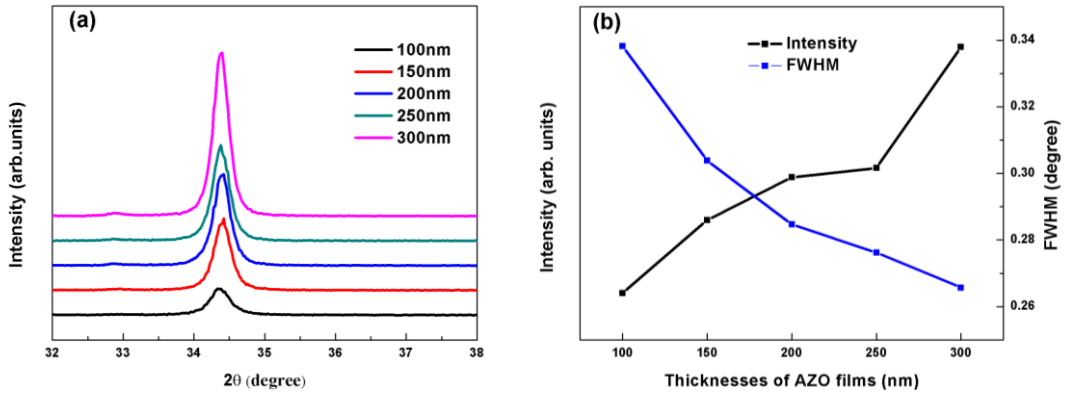

Fig. 3.2 (a) XRD patterns, (b) intensity and FWHM of (002) diffraction peak of as-deposited AZO films with different thicknesses.

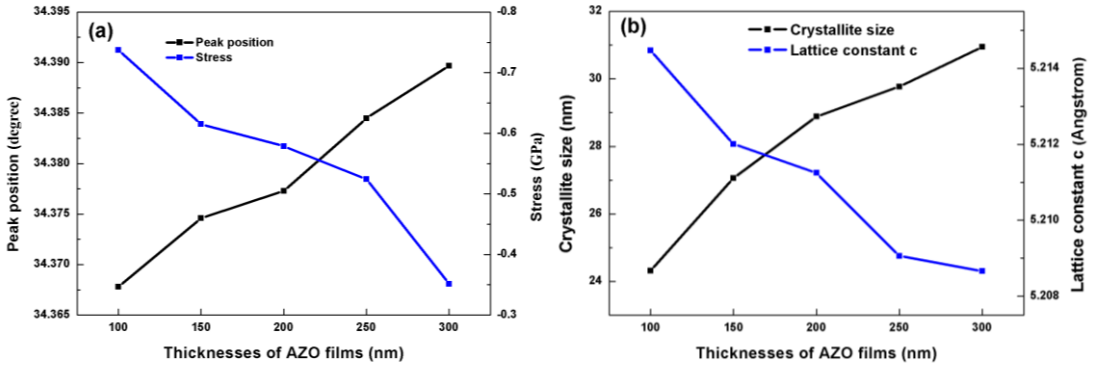

Fig. 3.3 (a) Peak position and stress, (b) c axis crystallite size and lattice constant c of AZO films with different thicknesses.

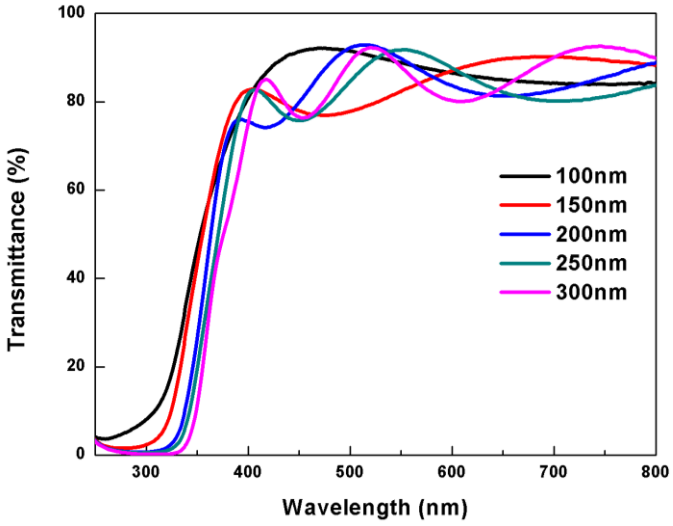

Fig. 3.4 Optical transmittance spectra of as-deposited AZO films with different thicknesses.

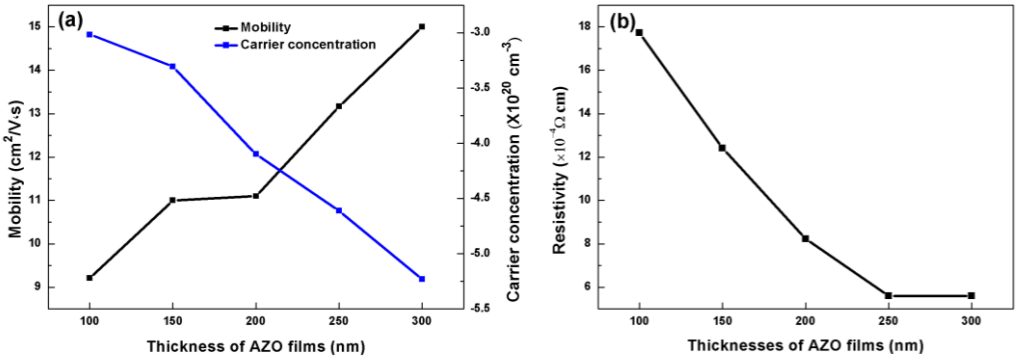

Fig. 3.5 (a) Hall mobility and carrier concentration, (b) resistivity of AZO films with different thicknesses.

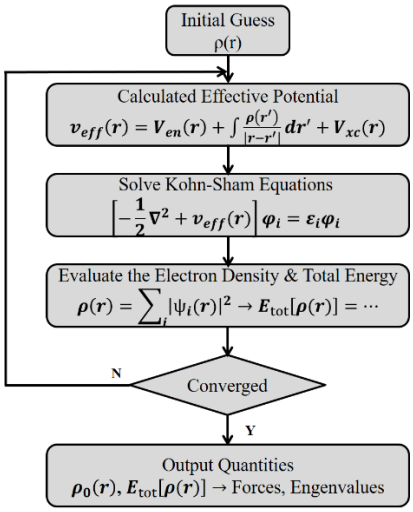

Fig. 3.6 schematic representation of a self-consistent loop for KS equation.

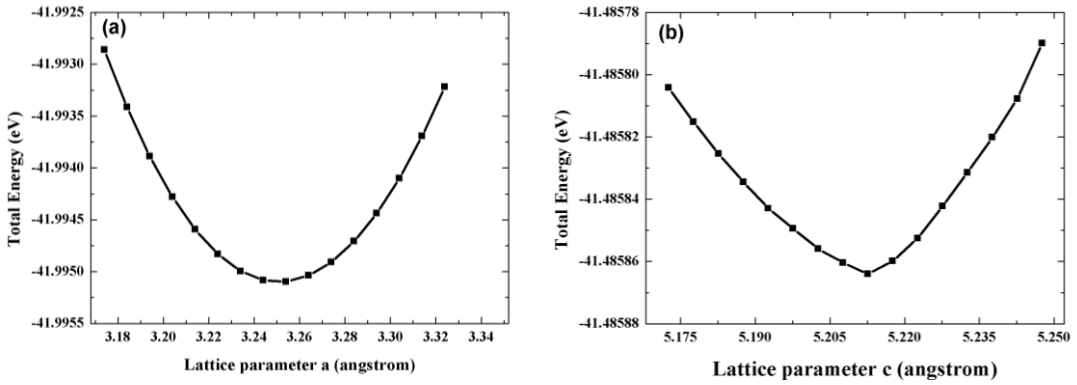

Fig. 3.7 Total energy as a function of lattice constant (a) a and (b) c for aluminum doping in ZnO.

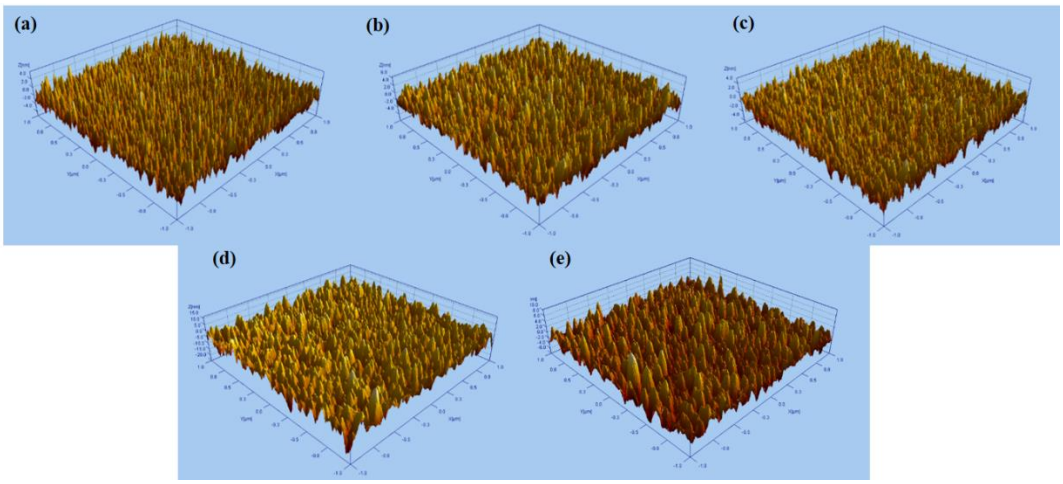

Fig. 3.8 AFM images of GZO films with thickness of (a) 100 nm, (b) 150 nm, (c) 200 nm, (d) 250 nm and (e) 300 nm.

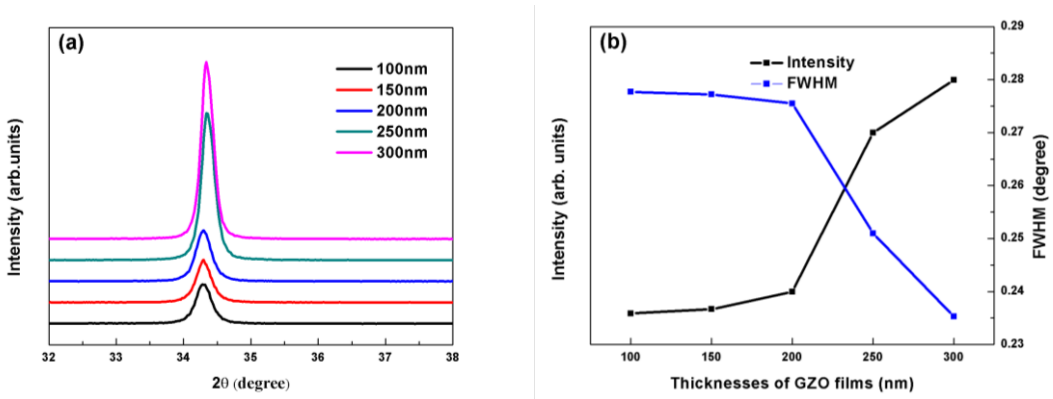

Fig. 3.9 (a) XRD patterns, (b) intensity and FWHM of (002) diffraction peak of GZO films as a function of thickness.

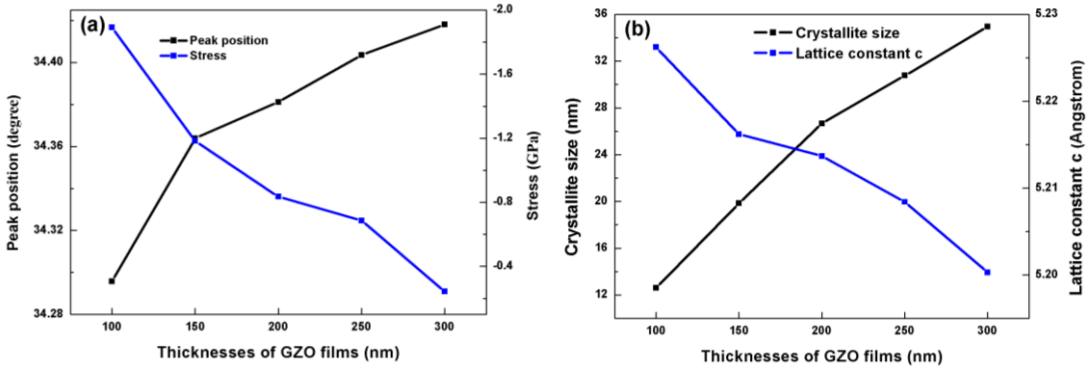

Fig. 3.10 (a) Peak position and stress, (b) c axis crystallite size and lattice constant c of GZO films with different thicknesses.

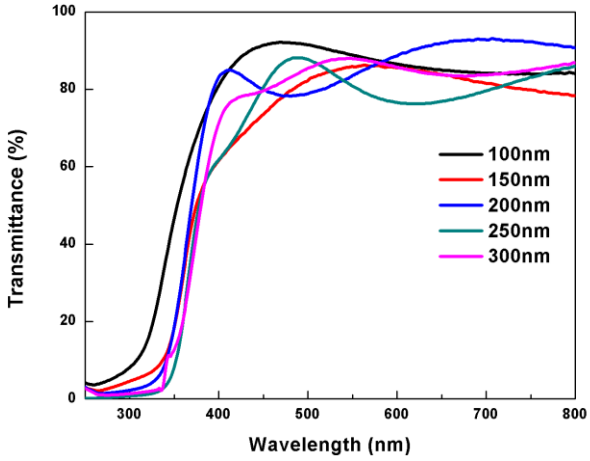

Fig. 3.11 Optical transmittance spectra of as-deposited GZO films.

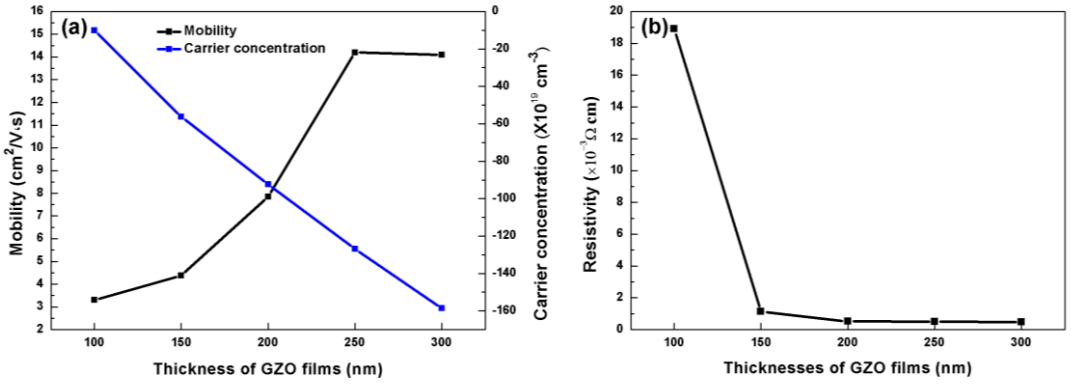

Fig. 3.12 (a) Hall mobility and carrier concentration, and (b) resistivity of AZO films as a function of film thickness.

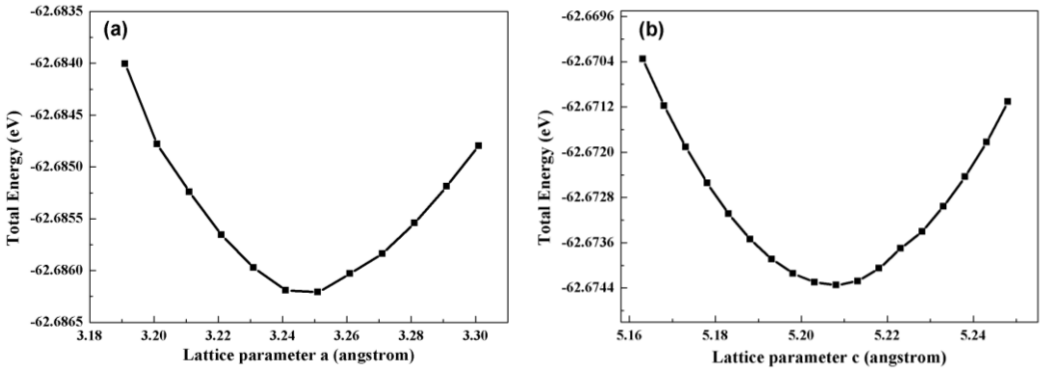

Fig. 3.13 Total energy as a function of lattice constant (a) a and (b) c for gallium doping in ZnO.

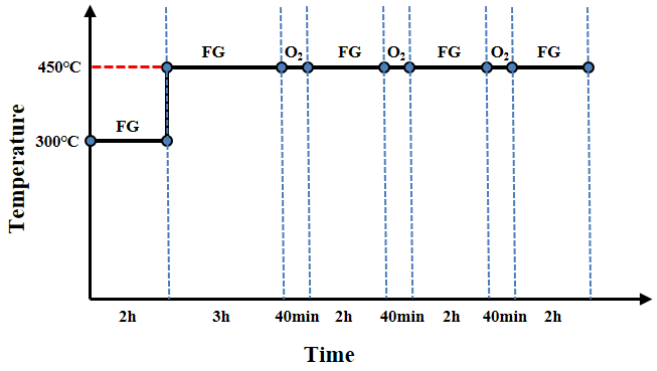

Fig. 3.14 Multi-annealing process applied for ZnO/ITO, ZnO/AZO and ZnO/GZO.

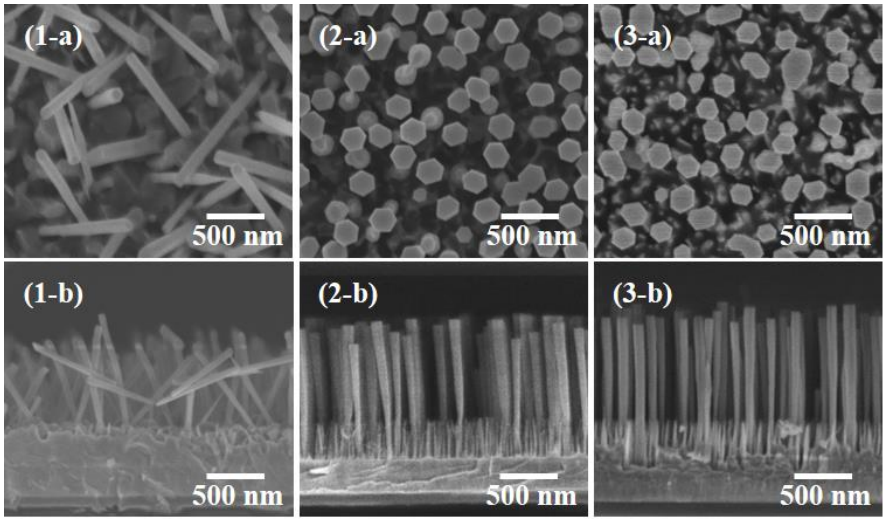

Fig. 3.15 (a) Top view and (b) cross section view FE-SEM images of ZnO nanorods grown on (1) ITO, (2) AZO and (3) GZO substrates.

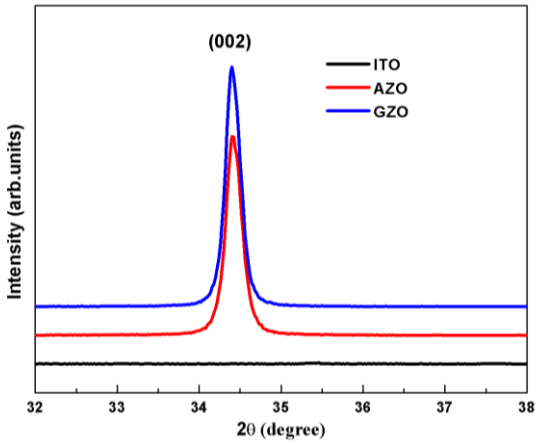

Fig. 3.16 XRD patterns of ZnO nanorods grown on ITO, AZO and GZO.

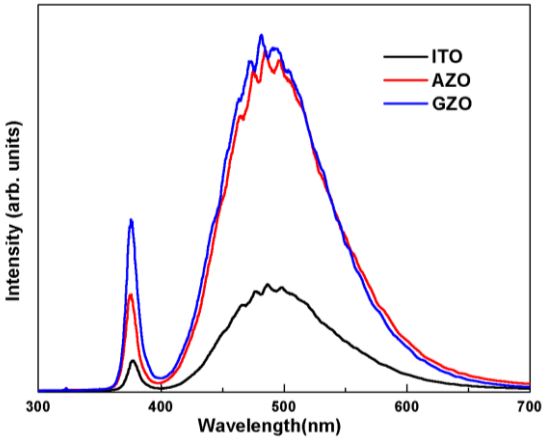

Fig. 3.17 PL spectra of ZnO nanorods grown on different substrates.

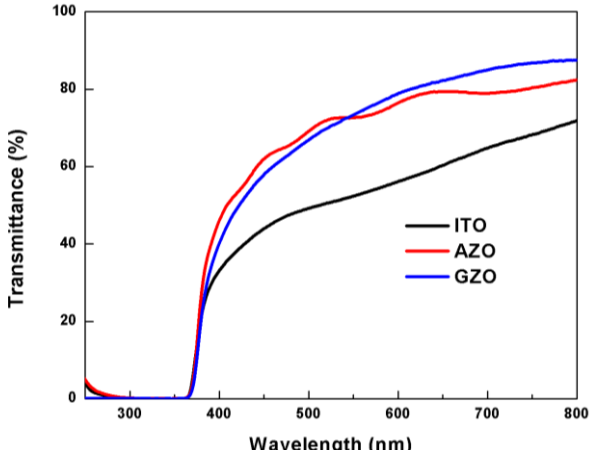

Fig. 3.18 Optical transmittance spectra of ZnO nanorods fabricated on different substrates.

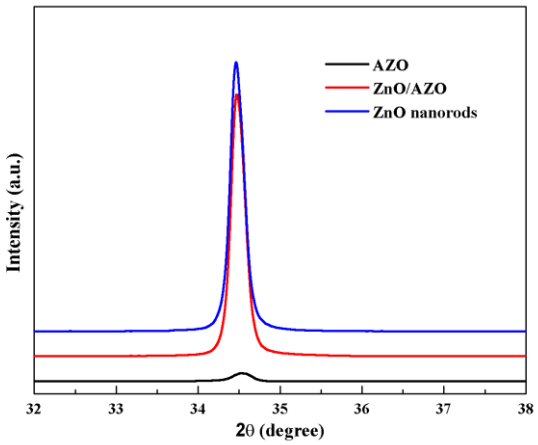

Fig. 3.19 Comparison of XRD patterns of GZO film with thickness of 300 nm, ZnO film deposited on GZO, and ZnO nanorods on GZO.

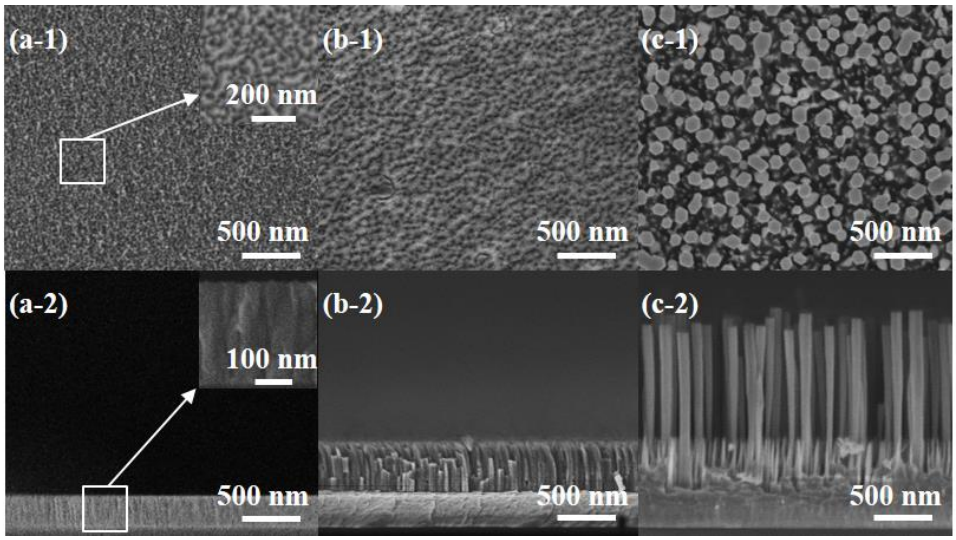

Fig. 3.20 (1) top view, and (2) cross section view FE-SEM images of (a) GZO film with thickness of 300 nm, (b) ZnO film with thickness of 500 nm on GZO film, (c) ZnO nanorods fabricated on GZO film.

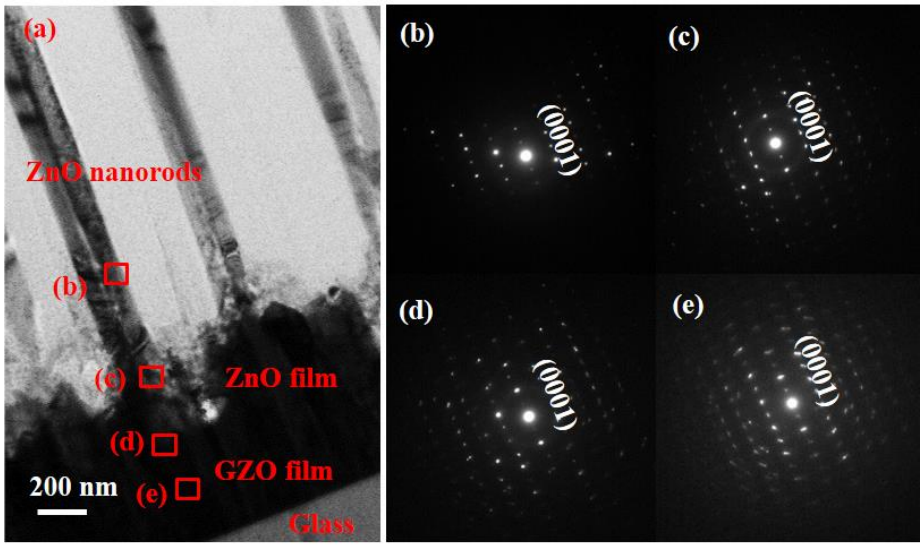

Fig. 3.21 (a) TEM cross-section images of ZnO nanorods fabricated on GZO film and diffraction patterns of (b) ZnO nanorod, (c) interface between ZnO nanorod and ZnO film, and (d) interface between ZnO film and GZO film, and (e) GZO film.

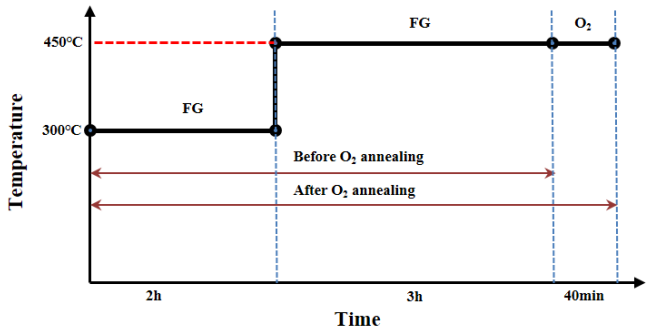

Fig. 3.22 Annealing conditions for ZnO nanorods before and after oxygen annealing.

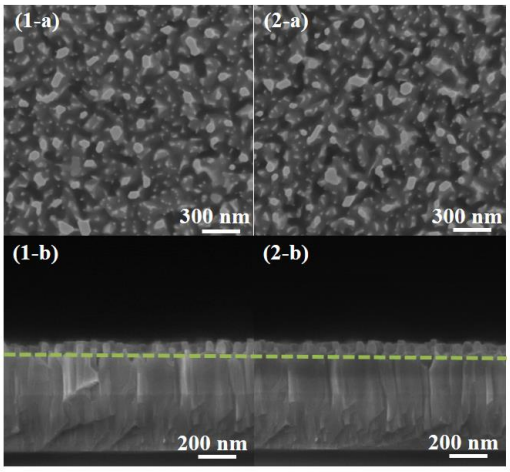

Fig. 3.23 (a) Top view and (b) cross section view FE-SEM images of ZnO nanorods (1) before and (2) after oxygen annealing.

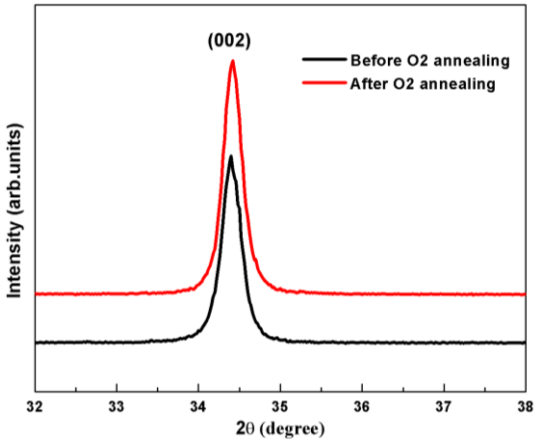

Fig. 3.24 XRD patterns of ZnO nanorods before and after oxygen annealing.

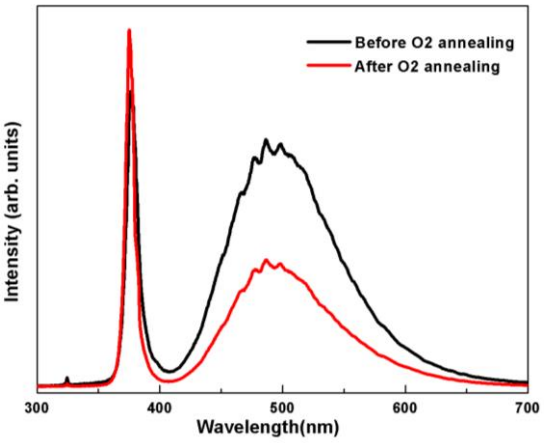

Fig. 3.25 PL spectra of ZnO nanorods before and after oxygen annealing.

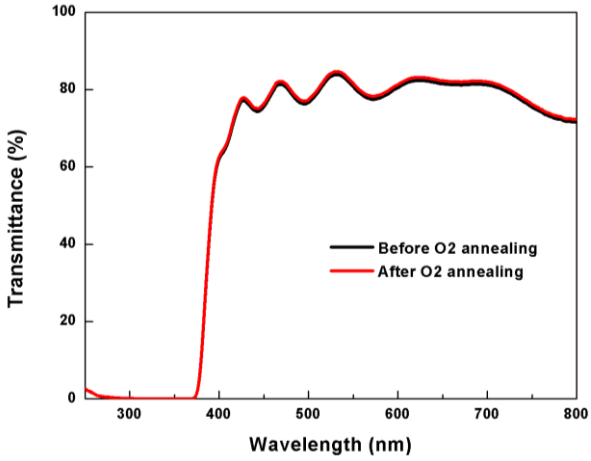

Fig. 3.26 Optical transmittance curves of ZnO nanorods before and after oxygen annealing.

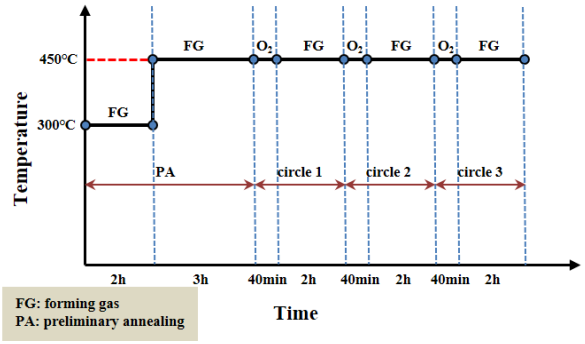

Fig. 3.27 Multi-annealing conditions for ZnO/AZO with different annealing processes.

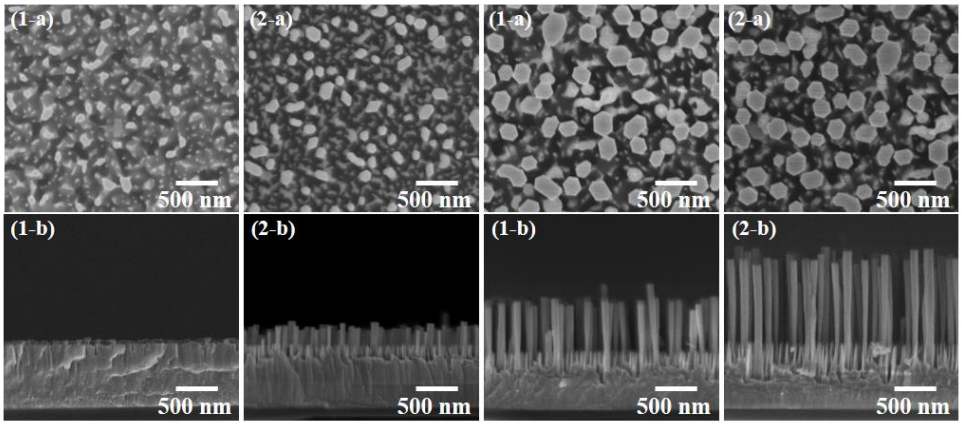

Fig. 3.28 (a) Top view and (b) cross section view FE-SEM images of ZnO nanorods after PA, 1 circle, 2 circles and 3 circles annealing.

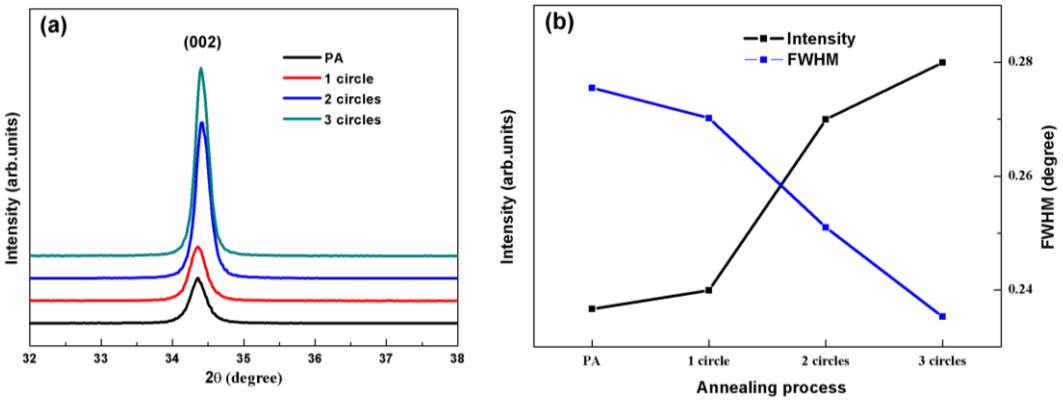

Fig. 3.29 (a) XRD patterns, (b) intensity and FWHM of (002) diffraction peak of ZnO nanorods after PA, 1 circle, 2 circles and 3 circles annealing.

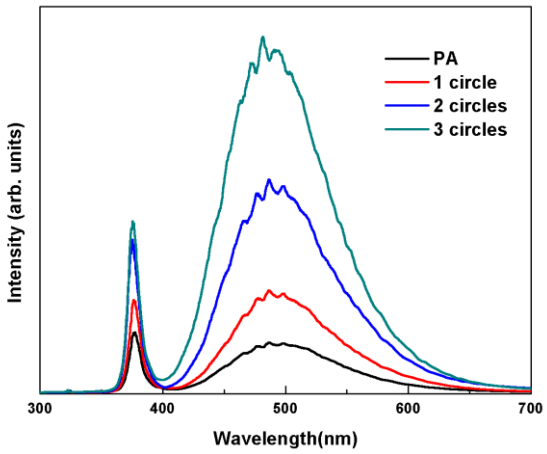

Fig. 3.30 PL spectra of ZnO nanorods after PA, 1 circle, 2 circles and 3 circles annealing.

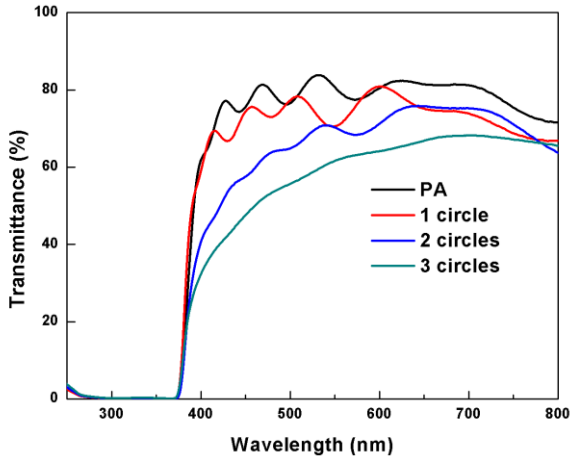

Fig. 3.31 Optical transmittance curves of ZnO nanorods after PA, 1 circle, 2 circles and 3 circles annealing.

3.5 References

[1] P.P. Das, S. Mukhopadhyay, S.A. Agarkar, A. Jana, and P.S. Devi. *Solid State Sci.* 48 (2015) 237.
[2] S. Ameen, M.S. Akhtar, M. Song, and H.S. Shin. *ACS Appl. Mater. Interfaces*, 4 (2012) 4405.
[3] N. Islavath, E. Ramasamy, D. Das, and S.V. Joshi. *Ceram. Int.* 41 (2015) 4118.
[4] A. Tubtimtae, and M.W. Lee, *Superlattice. Microst.* 52 (2012) 987.
[5] Q. Hu, Y. Li, F. Huang, Z. Zhang, K. Ding, M. Wei, and Z. Lin, *Sci. Rep.* 5 (2015) 11499.
[6] A.A. Rani, and S. Ernest, J. *Mater. Sci. Mater. El.,* 26 (2015) 762.
[7] C. Li, M. Furuta, T. Matsuda, T. Hiramatsu, H. Furuta, and T. Hirao. *Thin Solid Films,* 517 (2009) 3265.
[8] J. Nomoto, M. Konagai, K. Okada, T. Ito, T. Miyata, and T. Minami. *Thin Solid Films,* 518, (2010) 2937.
[9] D. Wang, Z. Li, T. Kawaharamura, M. Furuta, T. Narusawa, and C. Li. *Phys. Status Solidi C,* 9 (2012) 194.
[10] X. Li, C. Li, S. Hou, A. Hatta, J. Yu, and N. Jiang. *Compos. Part B: Eng.* 74 (2015) 147.
[11] X. Li, C. Li, T. Kawaharamura, D. Wang, N. Nitta, M. Furuta, H. Hiroshi, and A. Hatta. *Nanosci. Nanotech. Lett.* 6 (2014) 174.
[12] J. Musil, and J. Vlček. *Mater. Chem. Phys.* 54 (1998) 116.
[13] P.F. Fewster. *Rep. Prog. Phys.* 59 (1996) 1339.
[14] F. Jensen, Introduction to Computational Chemistry. John Wiley & Sons, New York, 1999.
[15] http://www.abinit.org/about
[16] D.R. Hamarm, M. Schhter, and C. Chiang. *Phys. Rev. Lett.* 43 (1979) 1494.
[17] J. Gong, J. Liang, and K. Sumathy. *Renew. Sustainable Energy Rev.* 16 (2012) 5848.
[18] Z. You, and G. Hua. *J. Alloy Comp.* 530 (2012) 11.
[19] X.M. Duan, C. Stampfl, M.M. Bilek, and D.R. McKenzie. *Phys. Rev. B,* 79 (2009) 235208.
[20] C. Li, T. Kawaharamura, T. Matsuda, H. Furuta, T. Hiramatsu, M. Furuta, and T. Hirao. *Appl. Phys. Exp. 2* (2009) 091601.
[21] M.N. Ashfold, R.P. Doherty, N.G. Ndifor-Angwafor, D.J. Riley, and Y. Sun. *Thin Solid Films,* 515 (2007) 8679.
[22] Z.L. Wang. *J. Phys. Condens. Mat.* 16 (2004) R829.

Chapter 4

Fabrication and characterization of ZnO nanorods by chemical bath deposition

4.1 Introduction

During past several decades, ZnO nanorods could be fabricated via various methods including vapor-liquid-solid process [1], pulse laser deposition [2], chemical vapor deposition [3,4], electrochemical [5], hydrothermal method and chemical bath deposition However, some of these methods require expensive equipment, high temperature and high vacuum conditions. Comparing with those methods required for expensive experimental conditions, chemical bath deposition (CBD) method is a simple technique to synthesis nanorods. It was reported that ZnO nanorods were fabricated by CBD method with optimized experimental conditions such as temperature, growing time and concentrations [6-8]. However, the obtained ZnO nanorods were either not uniform or not well-aligned. In order to fabricate well-aligned and uniform ZnO nanorods, further study should be performed.

In our previous work, the deposition of ZnO films by RF magnetron sputtering system [9,10] and the fabrication of ZnO nanorods by reducing annealing method [11,12] had been investigated. It was also difficult to obtain controllable ZnO nanorods with large area, high density and high uniformity by reducing annealing method.

In order to fabricate ZnO based electrode with controllable and well-aligned ZnO nanorods, a novel fabrication method combined RF sputtering with CBD method was reported in this chapter. Preparing of transparent conductive AZO film was reported in previous chapter. In this chapter, the fabrication of ZnO nanorods by CBD method will be investigated in detail. The effects of experimental parameters such as substrate thickness, precursor concentration and extended time on morphology, structural and optical properties of ZnO nanorods will be investigated.

4.2 Effects of AZO film thickness on the structural and optical properties of ZnO nanorods

4.2.1 Experiments

AZO films with different thicknesses ranging from 100 to 300 nm were deposited on

alkali-free glass sheets (Eagle XG, Corning Co. Ltd) according to the deposition conditions described in 3.2.1.1. The obtained AZO films were fixed with the screw standing vertically, as shown in Fig. 4.1. Then they were put into the solution of $Zn(NO_3)_2$•$6H_2O$ and hexathylenetetramine (HMT), which were analytical reagent grade. The concentrations of $Zn(NO_3)_2$•$6H_2O$ and HMT were 0.025 and 0.0125 mol/L, respectively. The solution was heated from room temperature to 95 °C and kept at 95 °C for 5 hours. After 5 hours, the substrate was taken out from the solution and washed with deionized water in an ultrasonic cleaner several times, dried in the air at room temperature. The CBD conditions were summarized in Table 4.1.

Table 4.1 CBD conditions of ZnO nanorods grown on AZO films with different thicknesses.

Film	Thickness (nm)	Concentration of $Zn(NO_3)_2$•$6H_2O$ (mol/L)	Concentration of HMT (mol/L)	Temperature (°C)	Time (h)
AZO	100 150 200 250 300	0.025	0.0125	95	5

4.2.2 Results and discussion

Figure 4.2 showed SEM images of ZnO nanorods grown on AZO films with different thicknesses. It was observed that well-aligned ZnO nanorods could grow on all of the as-deposited AZO films. The average diameter, density and the length of ZnO nanorods could be roughly counted from the top views and the cross-section views of SEM images. It was observed that the average length of ZnO nanorods grown on these films varied from 815, 630, 784, 732 and 711 nm in the order of the AZO thickness of 100, 150, 200, 250 and 300 nm respectively. Correspondingly, the average diameter of ZnO nanorods increased from 63 to 258 nm. The above results revealed that the morphological properties of ZnO nanorods were significantly influenced by AZO films. According to SEM images of AZO as-deposited films in Fig. 3.1, the average grain size of AZO films increased as thickness increased, which contributed to the increase in the diameter of ZnO nanorods during CBD procedure.

XRD patterns of ZnO nanorods grown on AZO films were presented in Fig. 4.3(a). It was observed that there was only a single dominant (002) diffraction peak for ZnO nanorods grown on these films. The dominant (002) peak indicated ZnO nanorods had highly preferred orientations in the (0001) direction, being perpendicular to the substrates. Fig. 4.3(b) showed the dependence of intensity and FWHM of ZnO nanorods as a function of AZO film thickness. This indicated that intensity of (002) diffraction peak increased as the thickness of AZO films

increased. In contrast, FWHM decreased from 0.1738 to 0.1287°. It also suggested that the crystallinity of ZnO nanorods improved as the thickness of AZO films increased. The variations in intensity and FWHM of (002) diffraction peak for ZnO nanorods were similar to those for AZO films, indicating that ZnO nanorods with better crystallinity were dependent on seeds layers with better crystallinity.

In order to confirm the microstructure of the obtained ZnO nanorods, a TEM measurement was carried out for the ZnO nanorod selected from 200-nm-thick AZO film. Fig. 4.4 showed TEM images of ZnO nanorods grown on 200-nm-thick AZO film. The high-resolution image in Fig. 4.3(b) confirmed that ZnO nanorod was highly c-axis oriented with lattice-plane spacing of 0.52 nm. The selected area electron diffraction (SAED) patterns in Fig. 4.3(c) displayed perfect regular diffraction spots, revealing good crystallinity for ZnO nanorods.

In the CBD process, AZO films served as the seeds layers for ZnO nanorods growth. The only (002) diffraction peak was found for all as-deposited AZO films, which revealed a preferable growth in the (0001) direction perpendicular to the substrates. According to ZnO crystal growth, ZnO prefers to grow in (0001) direction because the bonding energy in that direction is lower than that in other directions [13]. In the solution, the (0001) plane of AZO films attracted more Zn^{2+} and OH^- ions, promoting a faster growth rate along (0001) direction. ZnO nanorods grew vertically further in this direction with reaction time increased. Therefore, growth direction of AZO films contributed to the vertical alignment of ZnO nanorods.

The photoluminescence spectra were shown in Fig. 4.5. It was found that ZnO nanorods grown on AZO films showed a strong broad visible emission band centred at 636 nm and a weak near UV emission band centred at 378 nm. The strong visible emission could be attributed to zinc interstitials in ZnO nanorods [14]. Using software of Origin, this broad visible emission was divided into three emissions, which were centred at 540, 631, and 712 nm, respectively, shown in Fig. 4.6. These three emissions can be attributed to zinc interstitials located in different energy level. During CBD reaction, concentration ratio of $Zn(NO_3)_2 \cdot 6H_2O$ and HMT was set to 2:1, which meant concentration of zinc precursor was 2 times greater than that of OH^- source, resulting in more zinc interstitials formed in ZnO nanorods.

The optical transmittance of ZnO nanorods grown on AZO films with different thicknesses was given in Fig. 4.7. ZnO nanorods showed high transmittance of over 65% in visible range. Compared with the optical transmittance of as-deposited AZO films, the slight transmittance decrease might be due to the light scattering by defects in ZnO nanorods and impurities among ZnO nanorods.

ZnO nanorods showed controllable growth direction and high transmittance in visible range and AZO films showed low resistivity and high mobility. ZnO nanorods fabricated on AZO film can be used as photoanode in applications such as DSSCs.

4.2.3 Summary

Well-aligned ZnO nanorods were fabricated on AZO films with different thicknesses by CBD method. It was found that diamter of ZnO nanorod increased as film thickness increased, which was attributed to the increasing grain size. The obtained ZnO nanorods showed a similar tendency with regards to crystallinity to AZO films. As thickness increased, the crystallinity of ZnO nanorods improved. Good alignment of ZnO nanorods was dependent on the growth direction of AZO films. Fabricated ZnO nanorods showed a near UV emission and a strong broad visible emission, which was resulted from introducing zinc interstitials during ZnO nanorods formation. ZnO nanorods showed high transmittance of over 65% in visible range.

4.3 Effects of concentration of $Zn(NO_3)_2 \cdot 6H_2O$ and on the structural and optical properties of ZnO nanorods

4.3.1 Experiments

According to section 4.2, ZnO nanorods with hexeganol structure and uniform morphology were found at AZO film with thickness of 200 nm. Therefore, the next three sections would choose AZO film with thickness of 200 nm as the baseline to investigate the concentration dependence and time expanding dependence. In this section, the concentration of $Zn(NO_3)_2 \cdot 6H_2O$ was varied from 0.00625 to 0.05 mol/L while that of HMT were maintained at 0.0125 mol/L. The solution was heated from room temperature to 95 °C and kept for 5 hours. After 5 hours, the substrate was taken out from the solution and washed with deionized water in an ultrasonic cleaner several times, dried in the air at room temperature. The conditions were summarized in Table 4.2.

Table 4.2 CBD conditions of ZnO nanorods growth with different concentrations of $Zn(NO_3)_2 \cdot 6H_2O$.

Film	Thickness (nm)	Concentration of $Zn(NO_3)_2 \cdot 6H_2O$ (mol/L)	Concentration of HMT (mol/L)	Ratio	Temperature (°C)	Time (h)
AZO	200	0.00625	0.0125	0.5:1	95	5
		0.0125		1:1		
		0.025		2:1		
		0.05		4:1		

4.3.2 Results and discussion

Figure 4.8 showed SEM images of ZnO nanorods grown on AZO films under the concentration ratio of $Zn(NO_3)_2$•$6H_2O$ and HMT ranging from 0.5:1 to 4:1. It was obviously observed that well-aligned ZnO nanorods were fabricated on AZO film in different concentration of $Zn(NO_3)_2$•$6H_2O$. It was found that the morphology of ZnO nanorods was influenced significantly by the concentration of zinc precursor. As the concentration of zinc precursor increased, the average diameter of ZnO nanorods increased from 49 nm to 303 nm corresponding to the concentration ration increased from 0.5:1 to 4:1 while the density of ZnO nanorods decreased from 132/μm^2 to 8/μm^2. However, the average length of ZnO nanorods increased from 253 nm to 784nm, then decreased to 746 nm with the concentration ratio increased from 0.5:1 to 4:1. The above results were summarized in Table 4.3.

Table 4.3 Diameter, density and length of ZnO nanorods under different concentrations of $Zn(NO_3)_2$•$6H_2O$.

Concentration ratio	Diameter (nm)	Density (/μm^2)	Length (nm)
0.5:1	49	132	253
1:1	82	71	457
2:1	131	52	784
4:1	303	8	746

The mechanism for influence of concentration of $Zn(NO_3)_2$•$6H_2O$ on morphology property could be interpreted with chemical reactions of CBD method. According to the principle of minimum energy, it states that the internal energy will decrease and approach a minimum value at equilibrium with constant external parameters and entropy for a closed system [15]. This theory is also suitable for synthesis of ZnO nanorods grown by CBD method. The detailed chemical reactions were:

$$Zn(NO_3)_2 \rightarrow Zn^{2+} + 2\ NO_3^- \quad (1)$$

$$C_6H_{12}N_4 + H_2O \rightarrow 4\ NH_3 + 6HCHO \quad (2)$$

$$NH_3 + H_2O \leftrightarrow NH_4^+ + OH^- \quad (3)$$

$$Zn^{2+} + 4\ NH_3 \leftrightarrow Zn(NH_3)_4^{2+} \quad (4)$$

$$Zn^{2+} + 2\ OH^- \rightarrow Zn(OH)_2 \quad (5)$$

$$Zn(OH)_2 \leftrightarrow ZnO + H_2O \quad (6)$$

The growth of ZnO nanorods was controlled by above chemical reactions (1-6). With increasing concentration of $Zn(NO_3)_2$•$6H_2O$, more Zn^{2+} ions were ionized in the solution and reacted with OH^-, which was hydrolyzed from HMT, into $Zn(OH)_2$. $Zn(OH)_2$ dehydrated into

ZnO immediately once formed. As concentration of $Zn(NO_3)_2•6H_2O$ increased, more ZnO formed and stacked along the crystalline direction of AZO substrate, which served as the catalyst layer. Growth rate along c axis was faster than that along other axis. After growing for 5 hours, ZnO nanorods would grow up quickly along (001) direction.

The reason why concentration of precursors had a significant influence on growth of ZnO nanorods can be explained as follows: with the increase of zinc source, more ZnO formed and stacked along c axis and horizontal axis of nanorods, which resulted in the length and the diameter of ZnO nanorods increased. However, the growth rate along c axis was faster than that along horizontal axis because c axis was the polar growth direction along which the forming energy reached the minimum. When the concentration of $Zn(NO_3)_2•6H_2O$ was 0.05 mol/L, HMT was relatively rare compared with the excessive amount of zinc precursor, resulting in the decreasing growth rate along c axis.

XRD patterns of ZnO nanorods grown in different concentration ratios of $Zn(NO_3)_2•6H_2O$ and HMT indicated the presence of a single diffraction peak at (002) plane shown in Fig. 4.9(a), which revealed the preferentially oriented growth along c axis perpendicular to the substrate. As shown in Fig. 4.9(b), it illustrated that intensity of (002) peak increased and FWHM decreased as the concentration of $Zn(NO_3)_2•6H_2O$ increased, which meant crystallinity of obtained ZnO nanorods along (002) direction became better with increasing concentration of $Zn(NO_3)_2•6H_2O$.

Figure 4.10 showed photoluminescence spectra of ZnO nanorods grown in different concentration ratios of $Zn(NO_3)_2•6H_2O$ and HMT. PL spectra of ZnO nanorods by CBD method exhibited two different emissions: a strong broad emission with the peak located at around 636 nm in the visible region and a weak UV emission located at around 376 nm. The UV emission peak could be attributed to the exciton recombination corresponding to the near band-edge transition and the visible (orange-red) emission peak could be attributed to zinc vacancies V_{Zn}, zinc interstitials Zn_i and oxygen interstitials O_i [14]. It was found that the intensity of visible peak increased significantly. It can be attributed to the increasing growing rate of ZnO nanorods and excessive amount of Zn^{2+} with the increase of concentration, which formed more Zn_i in ZnO nanorods.

Figure 4.11 showed optical transmittance spectra of ZnO nanorods grown in different concentration ratios of $Zn(NO_3)_2•6H_2O$ and HMT. All samples showed high transmittance of over 80% in the visible range. High transmittance could be attributed to the well-aligned ZnO nanorods because less light was scattered by ZnO nanorods, which showed well-alignment of ZnO nanorods could be controlled by this novel method combined RF sputtering and CBD method.

4.3.3 Summary

The concentration ratios of $Zn(NO_3)_2$•$6H_2O$ and HMT had great influence on growth of ZnO nanorods grown on AZO film glass substrate by chemical bath deposition. ZnO nanorods were vertical aligned fabricated on AZO films due to the good growth direction of AZO films. As the concentration of zinc precursor increased, the diameter of ZnO nanorods remarkably increased, density of ZnO nanorods decreased, the length increased to the maximum at 2:1, the crystallinity became better, and the intensity of visible emission increased. All the samples showed high transmittance in the visible range.

4.4 Effects of concentration of hexamethylenetetramine on the structural and optical properties of ZnO nanorods

4.4.1 Experiments

In last section 4.3, the concentration of $Zn(NO_3)_2$•$6H_2O$ was changed while that of HMT were maintained at 0.0125 mol/L. However, in this section, the concentration of HMT was varied from 0.003125 to 0.025 mol/L while that of $Zn(NO_3)_2$•$6H_2O$ was kept at 0.025 mol/L, which set the concentration ratio from 2:025 to 2:2. The AZO films with thickness of 200 nm was put into the solutions with different concentration ratios. The solution was heated to 95 °C and kept for 5 hours. After 5 hours, the substrate was taken out of the solution and washed with deionized water in an ultrasonic cleaner several times, dried in the air at room temperature. The conditions were summarized in Table 4.4.

Table 4.4 CBD conditions of ZnO nanorods growth with different concentrations of HMT.

Film	Thickness (nm)	Concentration of $Zn(NO_3)_2$•$6H_2O$ (mol/L)	Concentration of HMT (mol/L)	Ratio	Temperature (°C)	Time (h)
AZO	200	0.025	0.003125	2:0.25	95	5
			0.00625	2:0.5		
			0.0125	2:1		
			0.025	2:2		

4.4.2 Results and discussion

Figure 4.12 showed SEM images of ZnO nanorods grown on AZO films with the concentration ratio of $Zn(NO_3)_2$•$6H_2O$ and HMT ranging from 2:0.25 to 2:2. The SEM images showed that ZnO nanorods were vertically aligned on AZO film under different concentration ratio. The morphology including diameter, density, and length was remarkably influenced by the

concentration ratios. Unlike the effects the concentration of $Zn(NO_3)_2 \cdot 6H_2O$ on ZnO nanorods, the average diameters of ZnO nanorods were 32, 67, 131 and 88 nm in the order of concentration ratio of 2:0.25, 2:0.5, 2:1 and 2:2. The density of ZnO nanorods was decreased from 178, 104 to 52/μm^2 and then increased to 92/μm^2 while the length of ZnO nanorods showed opposite tendency, as shown in Table 4.5. As observed from top view of SEM images, hexagonal structure was obtained for ZnO nanorods grown under concentration ratio of 2:1 and 2:2 while those grown under 2:0.25 and 2:0.5 showed non-hexagonal structure. It meant the concentration ratios of 2:1 and 2:2 could contribute to better morphology of ZnO nanorods.

Table 4.5 Diameter, density and length of ZnO nanorods under different concentrations of HMT.

Concentration ratio	Diameter (nm)	Density (/μm^2)	Length (nm)
2:0.25	32	178	646
2:0.5	67	104	786
2:1	131	52	784
2:2	88	92	582

The reason why ZnO nanorods could be influenced by concentration of HMT could be attributed to growth direction and growth rate during CBD process. According to chemical reactions (1-6), the growth rate of ZnO nanorods was significantly influenced by concentration of HMT. Low concentration of HMT resulted in low concentration of OH^-, which decreased the formation of ZnO. For ZnO nanorods, the dominant growth orientation was (0001) orientation. Therefore, ZnO nanorods grown under different concentrations showed preferential (0001) growth direction. As the concentration of HMT increased, horizontal growth rate increased, resulting in the diameter increased. However, the high concentration of OH^- could suppress the growth rate as well, which led to smaller diameter and shorter length for ZnO nanorods grown under the concentration ratio of 2:2.

Figure 4.13(a) exhibited XRD patterns of ZnO nanorods grown in different concentration ratios of $Zn(NO_3)_2 \cdot 6H_2O$ and HMT. It indicated the presence of a single diffraction peak at 34.40º, which was identified as (002) diffraction peak. It meant that ZnO nanorods grew preferentially along (0001) orientation, which was confirmed by the vertical growth for ZnO nanorods. Furthermore, intensity of (002) diffraction peak increased and FWHM decreased as the concentration ratio increased from 2:0.25 to 2:1 while those showed opposite tendency for concentration ratio of 2:2, as shown in Fig. 4.13(b). It indicated crystallinity of obtained ZnO nanorods became better as concentration ratio increased from 2:0.25 to 2:1, then became worse at concentration ratio of 2:2. The crystallinity tendency of ZnO nanorods could be attributed to the growth rate and the morphology of ZnO nanorods. The higher growth rate increased the

diameter and length of ZnO nanorods, resulting in the crystallinity became better.

Figure 4.14 showed photoluminescence spectra of ZnO nanorods grown in different concentration ratios of $Zn(NO_3)_2 \cdot 6H_2O$ and HMT. It was also clearly observed that ZnO nanorods exhibited two different emissions: a strong broad emission with the peak located at around 636 nm in the visible region and a weak UV emission located at around 376 nm, which were attributed to defects such as Zn_i and the intrinsic emission, respectively. It was found that the intensity of visible peak decreased significantly as concentration of HMT increased, which could be attributed to the increasing concentration of OH^-. Therefore, formation of zinc interstitials was suppressed, which resulted in the visible emission reduced.

Optical transmittance spectra of ZnO nanorods grown in different concentration ratios of $Zn(NO_3)_2 \cdot 6H_2O$ and HMT was shown in Fig. 4.15. All samples showed high transmittance of over 60% in the visible range. Vertical aligned ZnO nanorods scattered less light, which resulted in the high transmittance of ZnO nanorods. ZnO nanorods with small diameter and short length showed higher transmittance than those with bigger diameter and longer length, indicating large size of ZnO nanorod reduced the transmittance rate.

4.4.3 Summary

Vertical aligned ZnO nanorods was synthesized on AZO film under different concentrations of HMT. As the concentration of HMT increased, the diameter and length were increased firstly and then decreased. The crystallinity of ZnO nanorods was also firstly increased and then decreased. As concentration of HMT increased, the concentration of OH- increased, which resulted in less zinc interstitials formed. Therefore, the intensity of visible PL emission was decreased. The high transmittance of over 60% in visible range was obtained for ZnO nanorods. ZnO nanorods grown under 2:1 were suitable for application of DSSC in the future.

4.5 Effects of reaction time on the structural and optical properties of ZnO nanorods

4.5.1 Experiments

In last several sections, AZO films with thickness of 200 nm and concentration ratio of 2:1 were verified to be the best conditon to synthesize ZnO nanorods by CBD method. Therefore, using the same synthesis conditions, the time dependence will be investigated in order to get ZnO nanorods with large surface area and long length in this part.

AZO film with thickness of 200 nm was chosen to use as the substrate to fabricate ZnO nanorods. The solution was prepared with $Zn(NO_3)_2 \cdot 6H_2O$ of 0.025 mol/L and HMT of 0.0125

mol/L diluted into deionized water. AZO substrate was fixed at screw and stand vertically. The solution was heated to 95 °C and kept for 5 hours. After 5 hours, the substrate was taken out of the solution and washed with deionized water in an ultrasonic cleaner several times, dried in the air at room temperature. The solution was changed every 5 hours. Therefore, solution was changed 2, 3, and 4 times for ZnO nanorods with growth time of 10, 15, and 20 hours. The conditions were summarized in Table 4.6.

Table 4.6 CBD conditions of ZnO nanorods growth with expanded growth time.

Film	Thickness (nm)	Concentration of $Zn(NO_3)_2 \cdot 6H_2O$ (mol/L)	Concentration of HMT (mol/L)	Temperature (°C)	Time (h)
AZO	200	0.025	0.0125	95	5 10 15 20

4.5.2 Results and discussion

Figure 4.16 showed the SEM images of ZnO nanorods with expanded growth time. It was clearly seen that ZnO nanorods followed highly vertical alignment on AZO substrates regradless of the growth time. It was found that both diameter and length of ZnO nanorods increased with annealing processes increased. Morphology of SEM images showed much difference among ZnO nanorods with different growth time. The average diameter of ZnO nanorods was 131, 221, 195, and 207 nm in the order of growth time 5, 10, 15, and 20 hours, respectively. The uniformity of ZnO nanorods became worse as growth time increased. Small nanorods grew on big nanorods from the top view of SEM images. From Fig. 4.16(4-b), the nanorods overlapped and a big nanorod contains several small nanorods, which could be attributed to that ZnO nanorods served as the seed layer for further growth of ZnO nanorod. Due to the surface roughness and different growth rate of ZnO nanorods, several small ZnO nanorods grew on a big nanorod. As growth time expanded, the length of ZnO nanorods increased significantly from 784 nm to 3775 nm, which was due to ZnO prefered to grow along (0001) orientation.

Figure 4.17 showed the XRD patterns, (002) diffraction peak intensity and FWHM of ZnO nanorods with expanded growth time. XRD patterns exhibited only (002) diffraction peak for ZnO nanorods, which confirmed ZnO nanorods grew along (0001) orientation. Therefore, ZnO nanorods showed vertical growth. The intensity of (002) diffraction peak increased and the FWHM decreased, indicating the crystallinity became better with growth time extended.

Figure 4.18 showed the PL spectra of ZnO nanorods after growth time of 5, 10, 15, and 20 hours. It was found that the two emission peaks centered at 380 nm and 636 nm. As growth time

extended, intensity of UV emission decreased while that of yellow-orange emission increased greatly. It could be attributed to the growth of ZnO nanorods during time extended. As time extended, it can be clearly seen that several small nanorods consists of a big nanorod. As well-known, small nanorods usually have worse crystallinity and more defects than big nanorods. Therefore, the yellow-orange emission was increased. In contrast, worse crystallinity reduced the intrisic emission for ZnO nanorods, decreasing the UV emission.

Optical transmittance of ZnO nanorods with expanded growth time were shown in Fig. 4.19. It was found that the transmittance was largely reduced with growth time increased. The transmittance was reduced from 65% to 30% after growth time of 5 hours to 20 hours. The decreased transmittance was due to the ununiformity of ZnO nanorod and more defects formed in the nanorods. Therefore, optical transmittance was decreased greatly with growth time increased.

4.5.3 Summary

Reaction time had a significant influence on ZnO nanorod growth during CBD process. ZnO nanorods followed the same vertical growth direction on AZO substrate. The length increased greatly while the diameter showed no much difference, which verified ZnO nanorods preferred to grow along (0001) orientation. As the reaction time extended, crystallinity of ZnO nanorods was improved, intensity of UV emission was decreased and intensity of visible emission was increased. Moreover, the optical transmittance decreased significantly from 65% to 30% in visible range.

4.6 Conclusions

In this chapter, ZnO nanorods were fabricated on transparent conductive AZO films by chemical bath deposition method. The parameters such as the seed layer thickness, precursor concentration and reaction time in CBD mehotd were investigated in detail.

1) The effects of thickness of AZO film on ZnO nanorods growth were investigated. As AZO film thickness increased, the grain size of AZO films increased, which resulted in the diameter of ZnO nanorods was increased. ZnO nanorods followed the same (0001) orientation with underneath AZO films. The obtained ZnO nanorods showed improved crystallinity as substrate thickness increased. A near UV emission and a strong broad visible emission were found for ZnO nanorods, which was resulted from intrinsic transition and zinc interstitials. ZnO nanorods fabricated on AZO films with different thicknesses showed high transmittance of over 65% in visible range.

2) The effects of concentration of $Zn(NO_3)_2 \cdot 6H_2O$ on ZnO nanorods growth were investigated. It was found that the concentration of $Zn(NO_3)_2 \cdot 6H_2O$ had great influence on growth of ZnO nanorods. As the concentration of $Zn(NO_3)_2 \cdot 6H_2O$ increased, the diameter of ZnO nanorods increased greatly, the length increased to the maximum at concentration ratio of 2:1. The crystallinity was also improved and the intensity of visible emission increased due to the excessive supply of zinc source, which formed more zinc interstitials in ZnO nanorods. High transmittance of 60% in the visible range was obtained.

3) The effects of concentration of HMT on ZnO nanorods growth were investigated. The diameter of ZnO nanorods was increased from 2:0.25 to 2:1 and then decreased at 2:2. The crystallinity of ZnO nanorods was also firstly increased and then decreased. The intensity of visible PL emission was decreased as concentration of HMT increased, which was due to the increasing concentration of OH^- resulted in less zinc interstitials formed. The high transmittance of over 60% in visible range was obtained for ZnO nanorods.

4) The effects of reaction time on ZnO nanorods growth were investigated. As reaction time increased, ZnO nanorods always followed the same vertical growth direction on AZO substrate. The length of ZnO nanords increased greatly and crystallinity was improved. Moreover, intensity of UV emission was decreased and intensity of visible emission was increased due to more defects formed in the nanorods.

ZnO nanorods fabricated on AZO film with thickness of 200 nm and under concentration ratios of 2:1 showed uniform morphology, good crystallinity and high transmittance, which had great potential to be applied in application of DSSC.

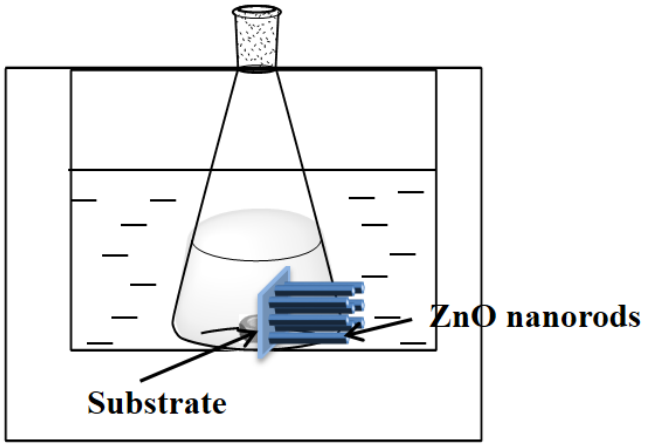

Fig. 4.1 Apparatus diagram of CBD method.

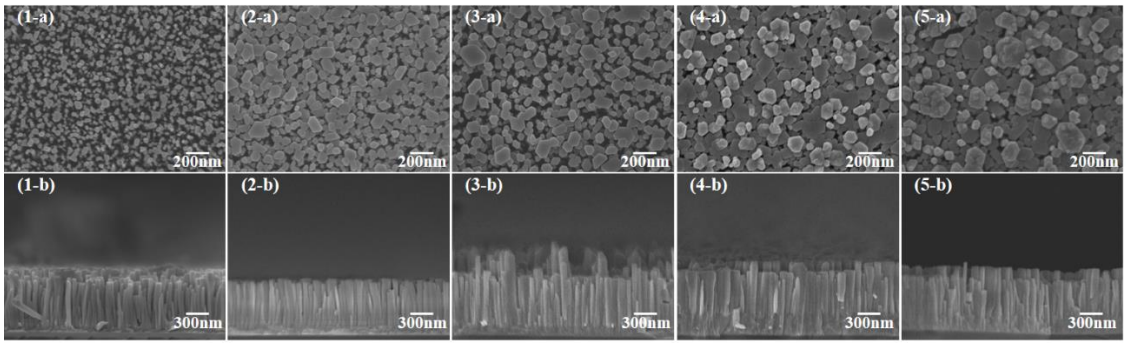

Fig. 4.2 (a) Top view and (b) cross-section view FE-SEM images of ZnO nanorods grown on AZO films with thickness of (1) 100, (2) 150, (3) 200, (4) 250, and (5) 300 nm.

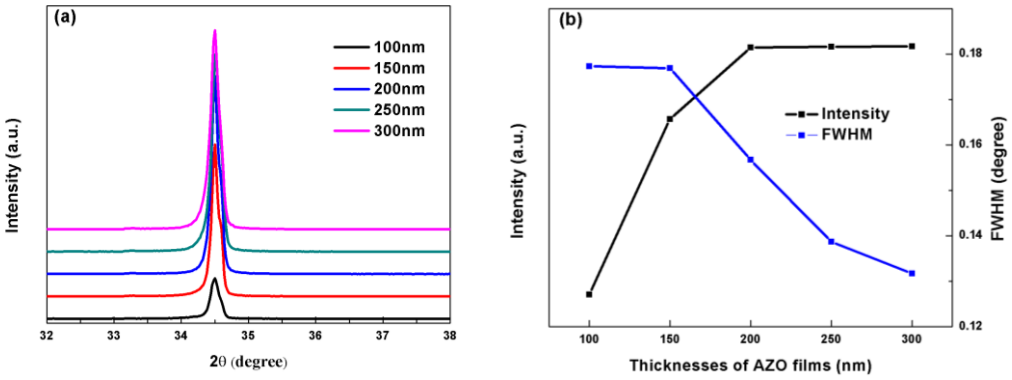

Fig. 4.3 (a) XRD patterns, (b) intensity and FWHM of (002) diffraction peak of ZnO nanorods grown on AZO films with different thicknesses.

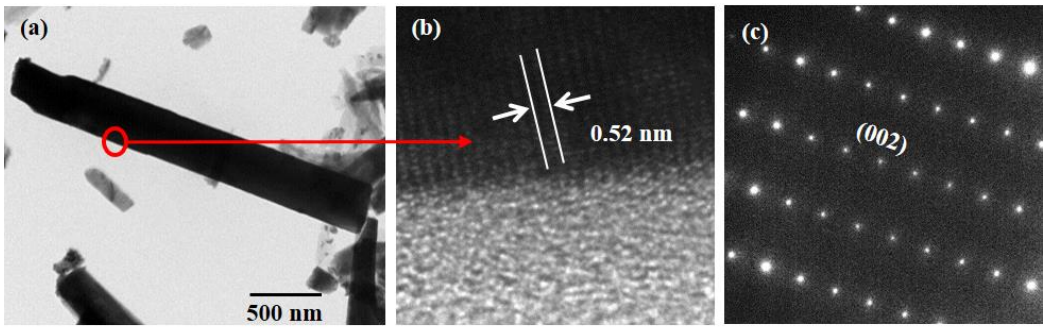

Fig. 4.4 (a) TEM image, (b) HRTEM image, and (c) SAED pattern of ZnO nanorod grown on 200-nm-thick AZO film.

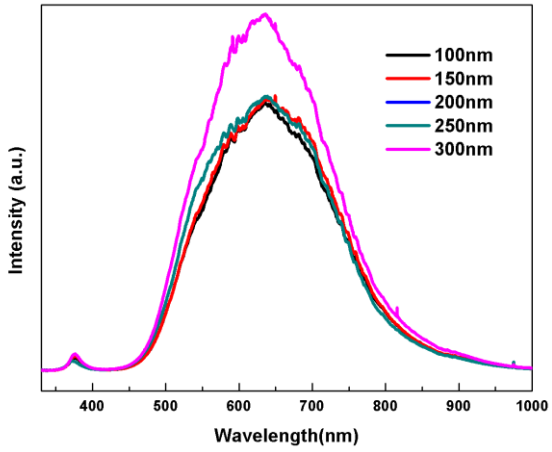

Fig. 4.5 PL spectra of ZnO nanorods grown on AZO films with different thicknesses.

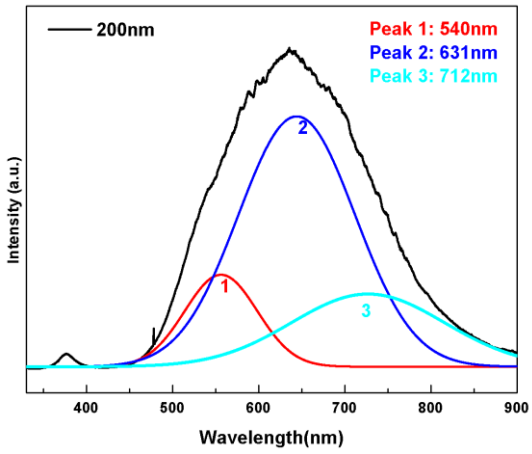

Fig. 4.6 Peak division of PL visible peak using Gaussian.

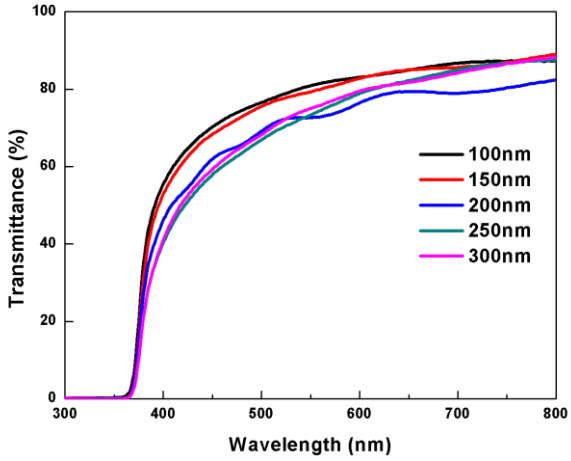

Fig. 4.7 Optical transmittance spectra of ZnO nanorods grown on AZO films with different thicknesses.

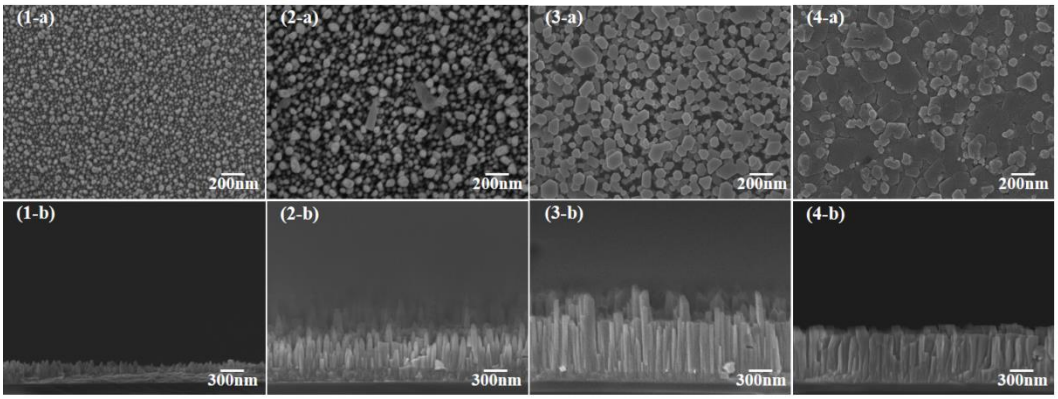

Fig. 4.8 (a) Top view and (b) cross-section view FE-SEM images of ZnO nanorods grown under the concentration ratio of (1) 0.5:1, (2) 1:1, (3) 2:1, and 4:1.

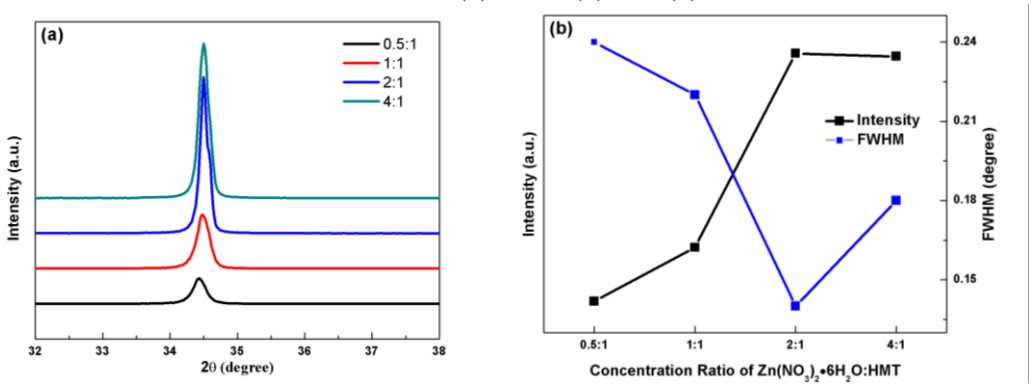

Fig. 4.9 (a) XRD patterns, (b) intensity and FWHM of (002) diffraction peak of ZnO nanorods grown ZnO nanorods grown under different concentrations of $Zn(NO_3)_2 \bullet 6H_2O$.

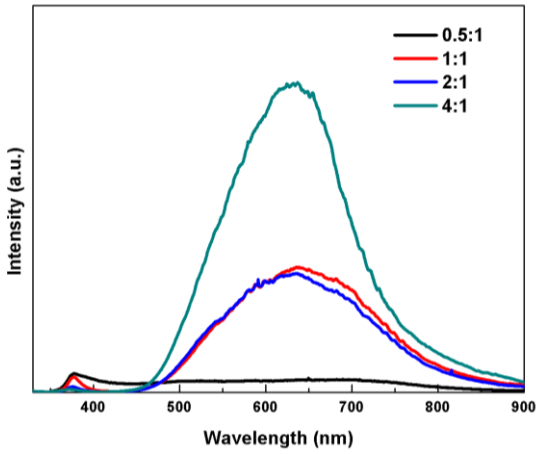

Fig. 4.10 PL spectra of ZnO nanorods grown under different concentrations of $Zn(NO_3)_2 \cdot 6H_2O$.

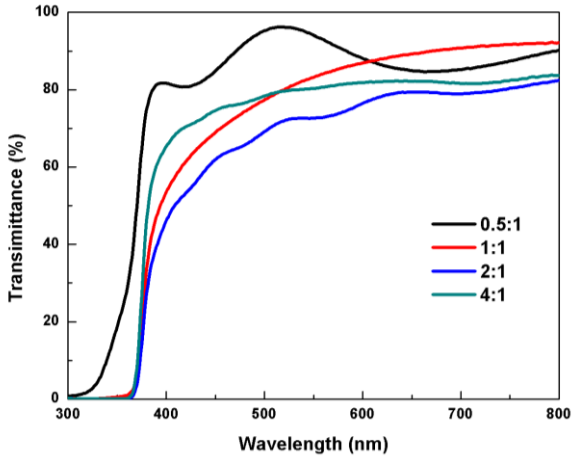

Fig. 4.11 Optical transmittance spectra of ZnO nanorods grown under different concentrations of $Zn(NO_3)_2 \cdot 6H_2O$.

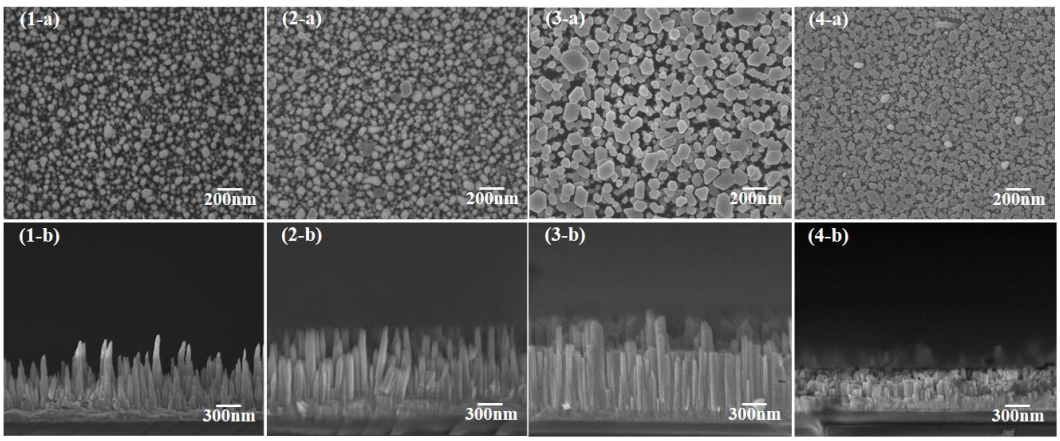

Fig. 4.12 (a) Top view and (b) cross-section view FE-SEM images of ZnO nanorods grown under the concentration ratio of (1) 2:0.25, (2) 2:0.5, (3) 2:1, and 2:2.

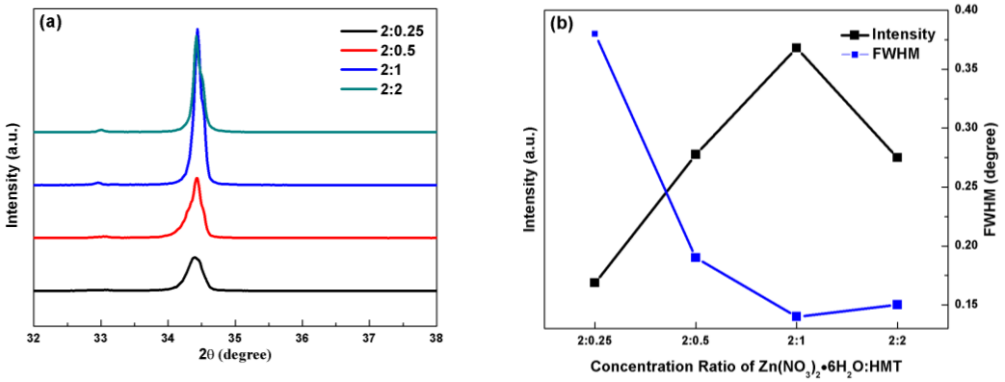

Fig. 4.13 (a) XRD patterns, (b) intensity and FWHM of (002) diffraction peak of ZnO nanorods grown under different concentrations of HMT.

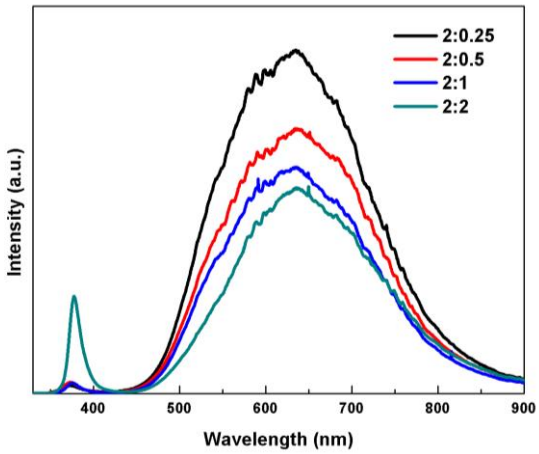

Fig. 4.14 PL spectra of ZnO nanorods grown under different concentrations of HMT.

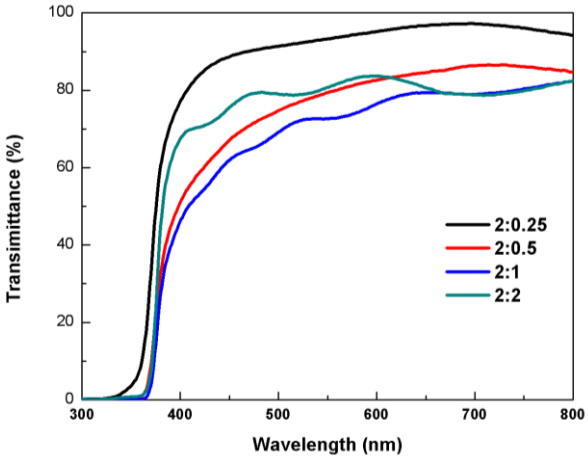

Fig. 4.15 Optical transmittance spectra of ZnO nanorods grown under different concentrations of HMT.

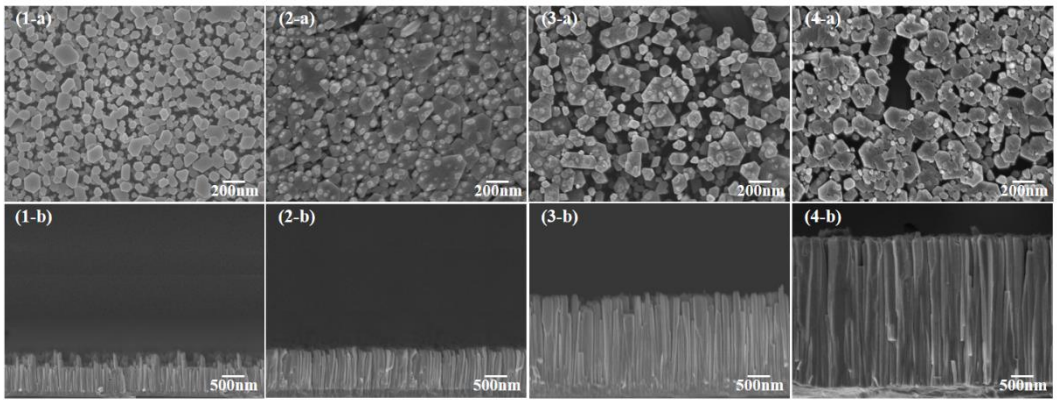

Fig. 4.16 (a) Top view and (b) cross-section view FE-SEM images of ZnO nanorods with reaction time of (1) 5, (2) 10, (3) 15, and 20 hours.

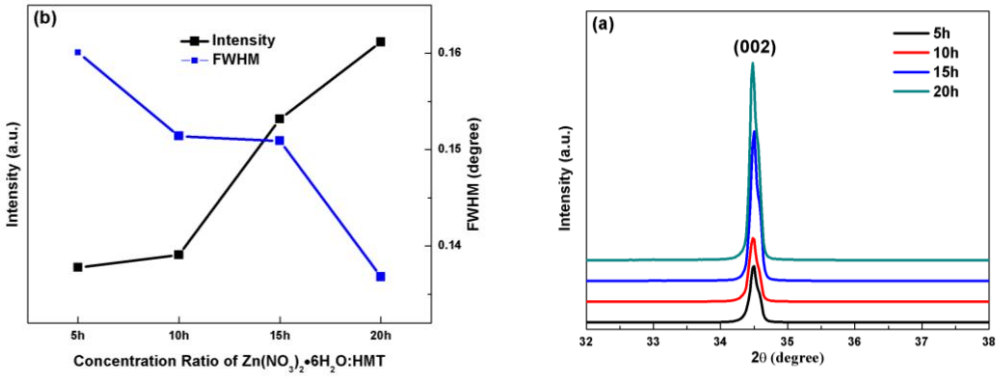

Fig. 4.17 (a) XRD patterns, (b) intensity and FWHM of (002) diffraction peak of ZnO nanorods grown ZnO nanorods with different growth time.

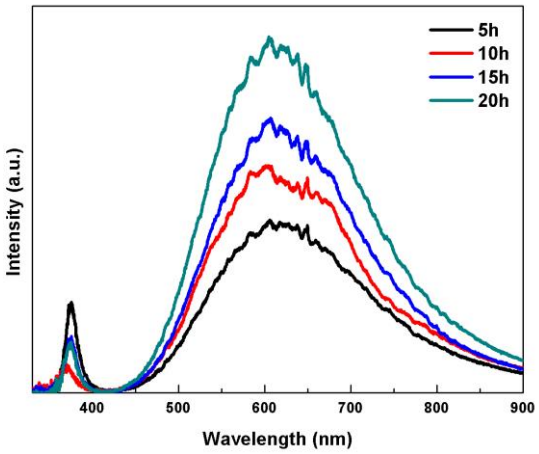

Fig. 4.18 PL spectra of ZnO nanorods with different growth time.

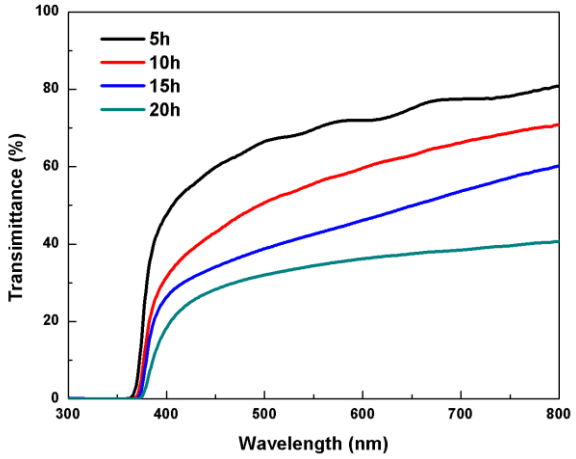

Fig. 4.19 Optical transmittance spectra of ZnO nanorods with different growth time.

4.7 References

[1] S.E. Ahn, J.S. Lee, H. Kim, S. Kim, B.H. Kang, and G.T. Kim. *Appl. Phys. Lett.* 84 (2004) 5022-5024.
[2] T. Okada, B.H. Agung, and Y. Nakata. *Appl. Phys. A.* 79 (2004) 1417-1419.
[3] X. Liu, X.H. Wu, H. Cao, and R.P.H. Chang. *J. Appl. Phys.* 95 (2004) 3141-3147.
[4] A. Yengantiwar, R. Sharma, O. Game, and A. Banpurkar. *Curr. Appl. Phys.* 11 (2011) S113-S116.
[5] S. Chu, D. Li, P.C. Chang, and J.G. Lu. *Nanoscale Res. Lett.* 6 (2011) 1-4.
[6] V.M. Guérin, J. Rathousky, and T. Pauporte. *Sol. Energ. Mat. Sol. Cells.* 102 (2012) 8-14.
[7] M. Thambidurai, N. Muthukumarasamy, D. Velauthapillai, and C. Lee. *J. Mater. Sci.* Mater. Electron. 24 (2013) 1921-1926.
[8] G.R. Patil, R.S. Gaikwad, M.B. Shelar, R.S. Mane, S.H. Han, and B.N. Pawar. *Arch. Phys. Res.* 3 (2012) 401-406.
[9] C. Li, M. Furuta, T. Matsuda, T. Hiramatsu, H. Furuta, and T. Hirao. *Adv. Mater. Sci. Eng.* (2007).
[10] H.P. Chang, F.H. Wang, J.C. Chao, C.C. Huang, and H.W. Liu. *Curr. Appl. Phys.* 11 (2011) S185-S190.
[11] D. Wang, Z. Li, T. Kawaharamura, M. Furuta, T. Narusawa, and C. Li. *Phys. Stat. Sol. c,* 9 (2012) 194-197.
[12] C. Li, T. Kawaharamura, T. Matsuda, H. Furuta, T. Hiramatsu, M. Furuta, and T. Hirao. *Appl. Phys. Exp.* 2 (2009) 091601.
[13] Z.L. Wang. *J. Phys. Condens. Matter,* 16 (2004) R829.
[14] C.T. Lee. *Mater.* 3 (2010) 2218-2259.
[15] A. Wei, X.W. Sun, C.X. Xu, Z.L. Dong, Y. Yang, S.T. Tan, and W. Huang. *Nanotech.* 17 (2006) 1740–1744.

Chapter 5

Fabrication and characterization of ZnO-TiO_2 core-shell nanorods by mist CVD method

5.1 Introduction

Recently, ZnO based DSSC has attracted much attention because TiO_2 and ZnO exhibit similar bandgap [1]. Additionally, ZnO has much higher electron mobility (200~1000 $cm^2/(V•s)$) than TiO_2 (0.1~4 $cm^2/(V•s)$) [2], which helps the electron transportation. More importantly, ZnO is much easier to fabricate into various nanostructures to enlarge the surface area [3]. Therefore, ZnO is expected to be the promising material to improve the conversion efficiency of DSSC.

However, ZnO nanorods are not as chemically stable as TiO_2， which are easy to be dissolved in acidic dye solution and electrolyte solution. ZnO nanorods are also easily to form some defects, which increase the electron-hole recombination and form more the Zn^{2+}/dye complex on the surface [4-7]. In order to overcome these disadvantages, ZnO nanorods should be coated with a chemically stable shell. This core-shell structure can form an energy barrier, which reduces the recombination, and passivate ZnO surface, which reduces the complex [8]. The ZnO-TiO_2 core-shell nanorod is one of the most promising nanocomposites due to the facts that conversion efficiency could be improved by about 1 to 5 times [9-12]. Previous studies reported ZnO nanorods could be coated with TiO_2 layer by sol-gel [13], solution method [14] and atomic layer deposition (ALD) [15]. However, the remained difficulties are the uniformity and controlling thickness of TiO_2 layer.

As reported, mist CVD method was proven to be an effective method to fabricate thin films [16,17] and modify ZnO nanorods [18]. Therefore, in order to overcome the disadvantages of ZnO-based DSSC, the novel mist CVD method was used to TiO_2 shell on ZnO nanorods in this research.

Titanium dioxide crystallizes in three structures: tetrahedral anatase, rutile and orthorhombic brookite. Rutile is primarily desirable for optical applications and is the thermodynamically stable phase; anatase has high kinetic stability and is more photocatalytic, which is expected to improve the performance of DSSC [10,12]. Therefore, fabrication of pure anatase TiO_2 film on ZnO nanorods is desired.

Based on our previous study, the high conversion efficiency of DSSC could be realized by

controlling the vertical alignment of ZnO nanorods, the quality of transparent conductive substrates [19-21]. In this chapter, a low-cost mist CVD method was introduced to deposit TiO_2 films and coat TiO_2 on ZnO nanorods. The effects of deposition temperature, precursor concentration, and annealing temperature on TiO_2 films and TiO_2 coating on ZnO nanorods were invesitigated.

5.2 Deposition and characterization of TiO_2 films by mist CVD method

5.2.1 Effects of deposition temperature on the morphological and structural properties of TiO_2 films

5.2.1.1 Experiments

The fine channel mist-CVD (FCM-CVD) system was used to synthesize TiO_2 films on quartz substrate. Details of the FCM-CVD system have been reported in previous research [19,20]. Titanium tetraisopropoxide (TTIP) used as the solute was dissolved in ethanol. The concentration of TTIP was 0.1 mol/L. The solution was ultrasonically atomized at the frequency of 2.4 MHz, and the mist was transferred to the fine channel using air as carrier gas and dilute gas, whose flow rates were controlled at 2.5 and 4.5 L/min, respectively. The Substrate temperature varied from 250, 300, 350, 400 and 450℃. The experimental conditions were shown in Table 5.1.

Table 5.1 Mist CVD conditions to fabricate TiO_2 films under different temperatures.

Titanium source	Concentration (Mol/L)	Solvent	Carrier gas flow rate (L/min)	Dilute gas flow rate (L/min)	Temperature (˚C)
$Ti(OC_3H_7)_4$	0.1	Ethanol	2.5	4.5	250
					300
					350
					400
					450

5.2.1.2 Results and discussion

The deposition rates of TiO_2 films were remarkably influenced by the substrate temperatrue, shown in Fig. 5.1. The thickness of TiO_2 film deposited at 250℃ could not be measured due to the uncontinous film. The thicknesses of TiO_2 films were 6.7, 4.2, 7.5, and 12 nm/min in the order of deposition temperature of 300, 350, 400, and 450℃.

The surface properties of TiO_2 films deposited at different temperatures were shown in Fig.

5.2. The small seperated particles were observed on the surface of TiO_2 film deposted at 250℃, which meant the film was not continuous. Therefore, this film would not be discussed in the research. The surfacs of TiO_2 films were very uniform with the rms roughness of 0.57, 1.28, 2.24, and 2.89 nm corresponding to 300, 350, 400, and 450℃. Fig. 5.3 depicted SEM images of TiO_2 films synthesized under 300, 350, 400 and 450℃. It was clearly seen that all the TiO_2 films exhibited a uniform surface. At synthesis temperature of 300℃, particles with size of 31 nm packed together and the space among particles was around 11 nm. When the synthesis temperature increased to 350℃, much smaller particles were found on the surface and small particles formed grain with size of 55 nm. As temperature increased to 400℃, TiO_2 films showed long and thin sheet-like grains with length of 132 nm. It was found that shorter and bigger sheet-like grains with length of 105 nm were shown on TiO_2 films synthesized under 450℃.

The structural property of TiO_2 films was determined by Rigaku ATX-G diffractometer using grazing incidence x-ray diffraction (GIXRD) model at a 0.35° incidence angle in the range from 20 to 80°. XRD patterns of TiO_2 films were shown in Fig. 5.4. A strong diffraction peak was observed at 25.28°, which was assigned to anatase (101) plane. Other diffraction peaks were also observed at 37.80, 48.04, 55.06, 62.68, 70.03 and 75.02°, identified to anatase (004), (200), (211), (204), (220) and (215) planes respectively. No any rutile diffraction peaks were found from XRD patterns, which meant the synthesized TiO_2 films were pure anatase. There was no visible diffraction peak for TiO_2 film under 300℃. (200) diffraction peak showed highest intensity than other diffraction peak for TiO_2 film under 350℃, indicating growth along (200) orientation was dominant. As temperature increased to 400 and 450℃, (101) diffraction peak became dominant because anatase TiO_2 preferentially grew along the (101) crystallographic direction.

Raman spectra of TiO_2 film was shown in Fig. 5.5, which was measured using a confocal Raman microscope (HORIBA, LabRAM HR800) with a 532.8 nm excitation laser. Raman spectra displayed three peaks centered at 399, 519 and 639 cm^{-1}, which were associated with the B_{1g}, $A_{1g}+B_{1g}$ and E_g modes of the anatase phase respectively. As temprature increased, the intensities of those Raman peaks increased, indicating that the anatase crystallinity became better. No rutile Raman peaks were found from Raman spectra, which was also confirmed that TiO_2 films was pure anatase.

The optical transmittance of TiO_2 films was shown in Fig. 5.6. It was found that the optical transmittance of TiO_2 films deposited at 350, 400, and 450℃ was similar (75%) in visible range. However, average transmittance of TiO_2 film at 300℃ was lower than 70% in visible range, which could be attributed to the poor crystallinity of TiO_2 films deposted at 250℃.

The formation mechanism of pure anatase TiO_2 film was attributed to mist-CVD method.

During mist-CVD process, TTIP would discompose into TiO_2, C_3H_6 and H_2O, shown in Equation 5.1 [22,23].

$$Ti(OC_3H_7)_4 \rightarrow TiO_2 + 4\ C_3H_6 + 2\ H_2O\ (T>510K) \quad (5.1)$$

TiO_2 would form on the quartz substrate. It was widely known that TTIP would react with H_2O as soon as H_2O formed. Therefore, TTIP would react with H_2O and produce H_4TiO_4, which would discompose to TiO_2 at high temperature, shown in Equation 5.2 and 5.3.

$$Ti(OC_3H_7)_4 + 4\ H_2O \rightarrow H_4TiO_4 + 4\ (CH_3)_2CHOH \quad (5.2)$$

$$H_4TiO_4 \rightarrow TiO_2 + 2\ H_2O \quad (5.3)$$

During mist-CVD process, TTIP ethanoic solution was atomized into mist droplets with the diameter of several micrometers under ultrasonic transducer. The mist droplets were transferred to the fine channel. The droplets would burst into smaller droplets with diameter of several nanometers in the reaction channel due to the high temperature and high pressure. TTIP decomposed into TiO_2, C_3H_6 and H_2O at temperature of over 510K. As well known, TTIP exhibits high reactivity to H_2O. Therefore, TTIP would react with H_2O and produce hydrous titanium oxide, which would discompose to TiO_2 immediately at high temperature of 450℃. During mist-CVD deposition, the decomposition and hydrolysis of TTIP occurred. Therefore, TiO_2 film was synthesized on quartz substrate. During TiO_2 film synthesis, TiO_2 film tended to be constructed into anatase other than rutile due to long-range ordered anatase structure was easier to construct than short-range ordered rutile structure. Moreover, isopropanol and ethanol in the chamber would suppress other growth orientation except (101) orientation, which was confirmed by XRD data. The high deposition rate (11.7 nm/min) of TiO_2 film at 450℃ could contribute to the sheet-like grains [24].

Therefore, TiO_2 films synthesized under 450℃ had better anatase crystallinity, which were used to study thermal stability.

5.2.1.3 Summary

In summary, pure anatase structured TiO_2 films were successfully synthesized by mist CVD method. As synthesis temperature increased from 300 to 450℃, surface of TiO_2 film was changed from particles to long and thin sheet-like grains. Only strong anatase diffraction peaks were found for TiO_2 film synthesized at 450℃ while no diffractions peak was shown for that at 300℃. Raman spectra confirmed that anatase structure was found for TiO_2 films. High transmittance of over 75% in visible range was found for obtained TiO_2 films deposited at temperature from 350 to 450℃.

5.2.2 Effects of TTIP concentration in ethanol solution on the morphological and structural properties of TiO_2 films

5.2.2.1 Experiments

TiO_2 films were synthesized by the fine channel mist-CVD (FCM-CVD) system, which was reported in last section. In this section, the experimental conditions including the unltrasonic frequency, carrier gas flow rate, dilute gas flow rate were kept the same with before. The substrate temperature was kept at 450℃. The concentration of TTIP dissolved in ethanol varied from 0.025 to 0.4 mol/L. The experimental conditions were summarized in Table 5.2.

Table 5.2 Mist CVD conditions to fabricate TiO_2 films under different concentrations.

Titanium source	Concentration (Mol/L)	Solvent	Carrier gas flow rate (L/min)	Dilute gas flow rate (L/min)	Temperature (˚C)
$Ti(OC_3H_7)_4$	0.025 0.05 0.1 0.2 0.4	Ethanol	2.5	4.5	450

5.2.2.2 Results and discussion

The deposition rate of TiO_2 film was significantly increased with the increase of TTIP concentration, shown in Fig. 5.7. The deposition rate increased from 4.0 nm/min at concentration of 0.025 mol/L to 13.63 mol/L at concentration of 0.4 mol/L. The higher concentration contributed to the higher deposition rate of TiO_2 film. As the concentration increased. the mist density of TTIP solution decreased, indicating that higher TTIP concentration increased the difficulty to generate mist droplet.

The SEM images of TiO_2 films deposited under different concentrations were shown in Fig. 5.8. The sheet-like grains were clearly observed for all the TiO_2 films. As concentration increased, the nanosheet length increased from 65 to 156 nm due to the significantly increased TiO_2 formation rate. The increasing grain size could be attributed to the higher deposition rate of TiO_2 film at higher TTIP concentrations.

XRD patterns of TiO_2 films shown in Fig. 5.9 indicated that a strong (101) diffraction peak and several small diffraction peaks, which were identified as the anatase structure. Same diffraction peaks were found for all TiO_2 films, which meant TiO_2 films had similar structures. The Intensity of (101) diffraction peak was increased from 0.025 to 0.2 mol/L and then

decreased at 0.4 mol/L, shown in Fig. 5.10(a). The FWHM of (101) diffraction peak showed the opposite tendency to intensity of TiO_2 films. It meant the anatase crystallinity of TiO_2 films increased as concentration increased to 0.2 mol/L. Based on the Scherrer's equations, the (101) orientation crystallite size of TiO_2 films was calculated to be from 14.41, 14.61, 14.53, and 17.05 nm corresponding to the concentration of 0.025, 0.05, 0.1, and 0.2 mol/L, shown in Fig. 5.10(b). However, the (101) crystallite size of TiO_2 films under 0.4 mol/L decreased. It also confirmed that anatase crystallinity of TiO_2 film increased with the increase of TTIP concentration.

Figure 5.11(a) showed Raman spectra of TiO_2 films deposited under different concentrations. It showed three peaks centered at 399, 519 and 639 cm^{-1}, which were associated with the B_{1g}, A_{1g} + B_{1g} and E_g modes of the anatase phase respectively. As concentration increased to 0.2 mol/L, the intensities of these peaks increased, shown in Fig. 5.11(b). However, intensities of these peaks decreased at 0.4 mol/L. Raman spectra confirmed that anatase crystallinity increased when concentration increased from 0.025 to 0.2 mol/L.

The optical transmittance of TiO_2 films was shown in Fig. 5.12. It was found that the optical transmittance of TiO_2 films deposited under different concentrations was over 75% in visible range. It meant the optical transmittance of TiO_2 films was not significantly influenced by the TTIP concentration.

As the concentration of TTIP increased, discomposation rate of TTIP to TiO_2 became faster and the deposition rate of TTIP increased during mist CVD process. However, the structural and optical properties of TiO_2 films were not influenced by increasing deposition rate of TiO_2 films because discomposation rate of TTIP to TiO_2 was dependent on the temperature not the concentration.

5.2.2.3 Summary

In summary, the effects of TTIP concentration on the morphological, structural and optical properties of TiO_2 films was investigated. It was found that size of sheet-like grain greatly increased with the increase of TTIP concentration. The pure anatase structured TiO_2 films were obtained. The crystallinity of TiO_2 film was slightly increased with the increase of concentration from 0.025 to 0.2 mol/L. The high transmittance of over 75% in visible range was obtianed for TiO_2 films.

5.2.3 Effects of annealing temperature on the morphological and structural properties of TiO_2 films

5.2.3.1 Experiments

TiO_2 films were deposited on quartz substrates by mist CVD method. The experimental conditions were interpreted in 5.2.1.1. Titanium tetraisopropoxide (TTIP) was dissolved in ethanol with the concentration of 0.2 mol/L. The flow rate of carrier gas and dilute gas were controlled at 2.5 and 4.5 L/min, respectively. The substrate temperature was kept at 450℃. After deposition, TiO_2 films were put into a rapid thermal annealing (RTA). The annealing temperature was varied from 600, 800, 1000, to 1100℃ and kept for 1 hour.

5.2.3.2 Results and discussion

Figure 5.13 showed the SEM images of as-deposited TiO_2 film and TiO_2 films after annealing at 600, 800, 1000, and 1100℃. As annealing temperature increased from 600 to 1000℃, the morphology of TiO_2 films including the length, thickness of sheet-like grains showed no much difference. However, when annealing temperature incresed to 1100℃, a whole large grain with many voids was found for TiO_2 films, which might be transformation of TiO_2 film occored at this temperature.

The XRD patterns of TiO_2 films were shown in Fig. 5.14. It showed a strong (101) diffraction peak and several small diffraction peaks such as (200), (211), (204), (220) and (215) diffraction peaks, all of which were assigned to anatase phase. XRD patterns confirmed that no rutile phase transformed after calcination from 600 to 1000℃.

However, XRD pattern for TiO_2 film calcined at 1100℃ was different from others. A strong diffraction peak was found at around 27.40°, which was identified to rutile (110) plane. Several small diffraction peaks were also assigned to planes of rutile phase. Weak anatase (101) diffraction peak was still found from the XRD patterns. The weight fractions of rutile phase and anatase phase could be calculated by the empirically determined formula in Eq. 5.4,

$$\frac{W_R}{W_A} = 1.22\frac{I_R}{I_A} - 0.28 \tag{5.4}$$

Here, I_R and I_A are the intensity of rutile (110) and anatase (101) diffraction peak respectively. Therefore, the weight fractions of rutile and anatase were 83.1:16.9. Most anatase structure had been transformed into rutile structure.

Raman spectra displayed three anatase phase peaks for TiO_2 films calcined from 600 to 1000℃, shown in Fig. 5.15. No rutile Raman peaks were found from Raman spectra, indicating no rutile phase transformed from temperature 600 to 1000℃. However, Raman spectrum of

TiO_2 film annealed at 1100℃ showed two strong peaks centered at 446 and 612 cm^{-1}, which were corresponded to the E_g and A_{1g} modes of the rutile phase respectively. Moreover, the weak anatase Raman peaks were still shown in the spectrum. Therefore, Raman spectrum confirmed that both anatase and rutile phases existed and weight of rutile phase was much more than that of anatase after annealed at 1100℃.

According to Scherrer's equation, the (101) orientation crystallite size could be calculated using the FWHM value. The calculated crystallite size of TiO_2 films slightly increased from 14.7 to 17.3 nm as annealing temperature increased from 600 to 1000℃, shown in Fig. 5.16. Therefore, crystallite size was slightly increased after annealing. As reported, anatase phase is thermodynamically more stable than rutile phase for crystallite size less than critical size. Moreover, the rutile transformation would be difficult to occur if the crystallite size doesn't increase [24], which maybe a reason of high thermal stability of TiO_2 films.

Another reason for high temperature stabilized pure anatase TiO_2 film could be due to the fabrication method. These unique sheet-like grains with fewer interfaces had a great influence on the anatase to rutile phase transformation. Fewer grain interface can slow the phase transformation. The packing characteristics of the sheet-like TiO_2 grains suppressed the interface nucleation of the rutile phase and significantly limited the phase transformation at a relatively high temperature. Moreover, the weak connections among sheet-like grains worked as barriers, which blocked anatase-rutile transformation.

As temperature increased over 1000℃, the interface and weak connections could not suppress the anatase-rutile transformation. The sheet-like grains were merged into a large grain with many voids.

5.2.3.3 Summary

In summary, annealed TiO_2 film showed no apparent surface changes as annealing temperature increased from 600 to 1000℃. No rutile Raman peak and no rutile diffraction peak were found from TiO_2 films annealed from 600 to 1000℃. The transformation from anatase to rutile for TiO_2 films occored at the temperature of 1100℃. The sheet-like grains and small crystallite size may contribute to the high temperature stability of TiO_2 film.

5.3 Fabrication and characterization of ZnO-TiO_2 core-shell nanorods

5.3.1 Experiments

Fabrication of ZnO nanorods by multi-annealing method was reported in Chapter 3. After fabrication of ZnO nanorods, TiO_2 was coated on ZnO nanorods by mist CVD method.

Alkali-free glass sheets (Eagle XG) were used as the substrates for ZnO nanorods fabrication. Firstly, 300 nm-thick AZO film and 500 nm-thick ZnO film was deposited on the glass substrates in a conventional RF (13.56 MHz) magnetron sputtering system successively. Secondly, a multi-annealing process was carried out for ZnO/AZO film. During multi-annealing process, the forming gas (H_2 : N_2 = 2 : 98 %) and oxygen was introduced in the annealing furnace in turn. Finally, TiO_2 thin film coating on ZnO nanorods was fabricated via Mist CVD system. The 0.1 Mol/L ethanoic TTIP solution was prepared as the precursor solution. The experimental conditions of mist CVD was interpreted in previous section.

5.3.2 Results and discussion

Figure 5.17 showed FE-SEM images of as-fabricated ZnO nanorods and ZnO-TiO_2 core-shell nanorods fabricated by mist CVD under different growth time. It was clearly observed that the morphology including the surface, the diameter, and length of ZnO nanorods was different. The as-fabricated ZnO nanorods showed hexagonal structure from the surface, being vertical to the substrate, as shown in Fig. 5.17(a-1) and (a-2). Fig. 5.17(b-f) showed the ZnO-TiO_2 core-shell nanorods by mist CVD under growth time of 5, 10, 15, and 20 min. It was clearly observed that the surface of ZnO nanorod was covered with TiO_2 from the top view and cross-section views of core-shell nanorods. From the inserted images of ZnO nanorods, small TiO_2 particles formed on the surface of ZnO nanorod under growth time of 5 min. As growth time expanded to 20 min, the sheet-like grains were clearly observed. As growth time expanded, the diameter of core-shell increased, which indicated the thickness of TiO_2 shell increased significantly. The increase of TiO_2 shell thickness was not linearly with growth time. The calculated TiO_2 shell thicknesses were 3, 8, 15, and 25 nm corresponding to the growth time of 5, 10, 15, and 20 min. The length of ZnO nanorods also increased with growth time of mist CVD increased. The length growth of ZnO nanorods showed similar tendency to that of diameter.

XRD patterns of ZnO nanorods and ZnO-TiO_2 core-shell nanorods were shown in Fig. 5.18. ZnO (002) diffraction peak was clearly found from the XRD patterns. Moreover, a strong diffraction peak was observed at 25.2°, which was assigned to anatase (101) plane. Other diffraction peaks were also observed at 37.8, 48.0, 55.0, 62.6, 70.0 and 75.0°, which were identified to anatase (004), (200), (211), (204), (220) and (215) planes respectively. No any rutile diffraction peaks were found from XRD patterns, which meant the fabricated ZnO-TiO_2 core-shell nanorods were pure anatase. As TiO_2 growth time increased, the intensity of anatase (101) diffraction peak increased due to the TiO_2 thickness increased. Therefore, pure anatase TiO_2 shell was successfully synthesized on ZnO nanorods.

In order to further confirm formation of the ZnO-TiO_2 core-shell, TEM and EDX

measurement of core-shell structures fabricated under 15 min was performed, shown in Fig. 5.19. It was clearly observed that the a thin and uniform TiO_2 shell had been formed on the surface of ZnO nanorod. The thickness of TiO_2 shell was around 15 nm. The lattice fringes of 0.35 nm in HRTEM images corresponding to (101) plane of TiO_2 was shown in Fig. 5.19(b). HRTEM images also showed the (101) plane of TiO_2 shell with different growth directions, which was confirmed the intertwined nanosheet structure. EDX elemental mapping of Zn and Ti for a single core-shell nanorod was shown in Fig. 5.19(c,d). It was clearly seen that the shell layer of TiO_2 was uniformly coated on the surface of ZnO nanorod. Line scan of EDX for ZnO-TiO_2 core-shell was shown in Fig. 5.20. It was found that population intensity of Ti was higher on the edge and lower in the center of core-shell while that of Zn was only shown in the center.

Therefore, TiO_2 shell was successfully fabricated on ZnO. The mechanism of formation of TiO_2 shell on surface of ZnO nanorods during Mist-CVD can be explained as follows: Solute TTIP was dissolved in ethanol following by atomized to form mist droplets in the diameter scale of several micrometers with ultrasonic transducer. The mist droplets containing TTIP molecules were transferred by the air from the supply unit to the reaction chamber where ZnO nanorods were settled. During the Mist-CVD process, TiO_2 shell formed according to these reactions of TTIP. Moreover, ZnO nanorods served as the catalysts to contribute to TiO_2 shell during Mist-CVD process. When Mist-CVD growth started for 5 min, the small TiO_2 nuclei formed on the surface of ZnO nanorods. As growth time extended, formed TiO_2 nuclei epitaxial grew and TiO_2 shell formed. During TiO_2 shell synthesis, TiO_2 tended to be constructed into anatase other than rutile due to long-range ordered anatase structure was easier to construct than short-range ordered rutile structure. Moreover, isopropanol and ethanol in the chamber would suppress other growth orientation except (101) orientation, which was confirmed by XRD data. Therefore, the sheet-like grains for TiO_2 shell formed on the ZnO nanorods [24].

Figure 5.21 showed optical transmittance curves of ZnO nanorods and core-shell nanorods. ZnO nanorods without TiO_2 shell showed high transmittance of 75% in visible range. As TiO_2 growth time increased, the transmittance in visible range decreased significantly. For core-shell nanorods coated after 20 min, the transmittance in visible range was nearly 30% due to great scattering of sheet-like grains of TiO_2.

5.3.3 Summary

In summary, ZnO nanorods coated with pure anatase TiO_2 shell had been successfully fabricated on AZO substrate by mist CVD method. The morphology of ZnO nanorods were greatly modified with TiO_2 layers under different growth time. As growth time increased, the

diameter and length of ZnO-TiO_2 core-shell nanorods greatly increased. EDX confirmed that TiO_2 shell was uniformly covered the surface of ZnO nanorod. However, the optical transmittance of ZnO nanorods was decreased due to coated with TiO_2 shell.

5.4 Conclusions

In this chapter, pure anatase TiO_2 films and TiO_2 coated ZnO nanorods were synthesized by mist CVD method. The parameters including synthesis temperature, TTIP concentration, annealing temperature on TiO_2 film deposition and effects of mist CVD deposition time on ZnO-TiO_2 core-shell structures were investigated in detail.

1) Synthesis temperature had a great influence on the deposition of TiO_2 films. TiO_2 film could be deposited at temperature of 250℃. As synthesis temperature increased from 300 to 450℃, surface of TiO_2 film was changed from particles to long and thin sheet-like grains. XRD patterns indicated that deposited TiO_2 films were pure anatase and the crystallinity of TiO_2 films became better. High transmittance of over 75% in visible range was found for obtained TiO_2 films deposited at temperature from 350 to 450℃. Transmittance of TiO_2 films slightly increased with depostion temperature increased.

2) The influence of precursor concentration of TTIP on morphological, structural and optical properties of TiO_2 films was studied. SEM images confirmed that length of sheet-like grain was greatly increased, indicating the higher formation rate of sheet-like grains with the increase of concentration from 0.025 to 0.2 mol/L. Furthermore, TiO_2 kept the anatase structure and crystallinity of TiO_2 film was slightly increased. All the TiO_2 films exhibited a high transmittance of over 75% in visible range. TTIP concentration had no great influence on morphological, structural, and optical properties of TiO_2 film. Better crystallinity, faster deposition rate and high transmittance of TiO_2 film was obtained at the concentration of 0.2 mol/L, which was the optimized experimental conditions for TiO_2 films.

3) For application of TiO_2, the anatase-rutile transformation was very important. The TiO_2 films were annealed at temperature from 600 to 1100℃. After annealed at temperature from 600 to 1000℃,no visible change was observed from the morphology of TiO_2 film. Only anatase diffraction peaks and Raman peaks were found from TiO_2 films annealed from 600 to 1000℃. When temperature increased to 1100℃, sheet-like grains merged into a large grains. The rutile diffraction peaks and Raman peaks were found. Therefore, the transformation from anatase to rutile for TiO_2 films occored. The sheet-like grains and small crystallite size may contribute to the high temperature stability of TiO_2 film.

4) pure anatase TiO_2 shell was successfully coated on ZnO nanorods by mist CVD method. The morphological, structural and optical properties of ZnO nanorods were greatly modified with TiO_2 layers under different deposition time. The diameter of ZnO-TiO_2 core-shell nanorods was

greatly increased with the increased of deposition time. The length of core-shell nanorods slightly increased. XRD patterns and EDX confirmed that pure anatase TiO_2 shell was uniformly covered the surface of ZnO nanorod. The optical transmittance of ZnO nanorods was decreased due to coated with TiO_2 shell. The TiO_2 coated ZnO nanorods were expected to improve the performance of ZnO based solar cell, which would be demonstrated in Chapter 6.

TiO_2 synthesized by mist CVD showed very high stability at high temperature and TiO_2 shell was uniformly coated on ZnO nanorods, which had great potential to be applied in high temperature sensor and photocatalytic applications.

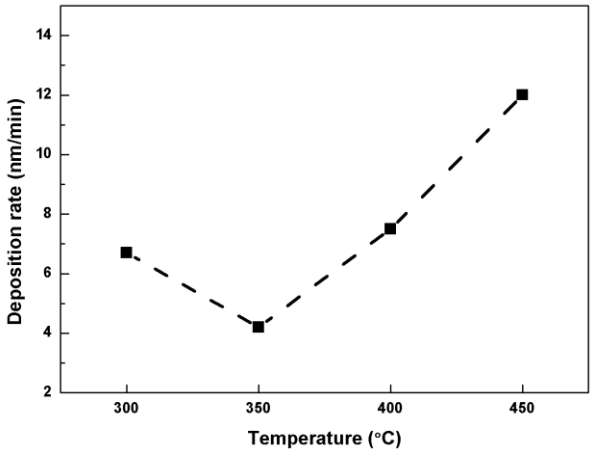

Fig. 5.1 Deposition rate of TiO_2 films synthesized at temperature of 300, 350, 400 and 450℃.

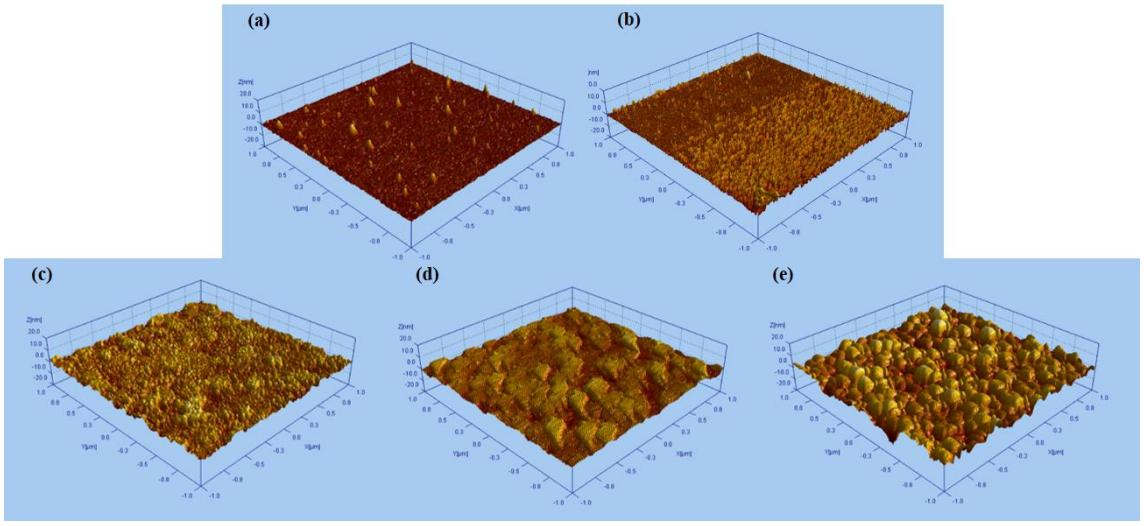

Fig. 5.2 AFM images of TiO_2 films synthesized at temperature of (a) 250, (b) 300, (c) 350, (d) 400 and (e) 450℃.

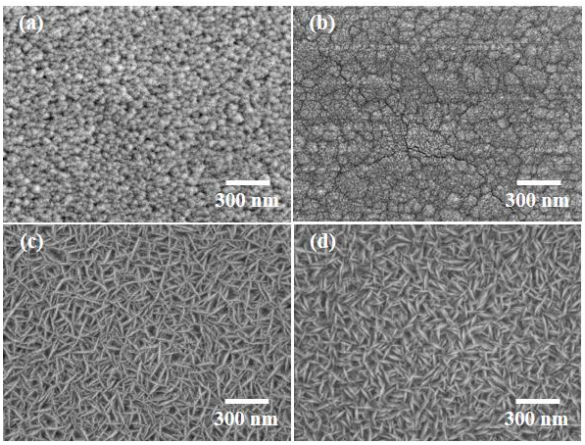

Fig. 5.3 SEM images of TiO_2 films synthesized at temperature of (a) 300, (b) 350, (c) 400, and (d) 450℃.

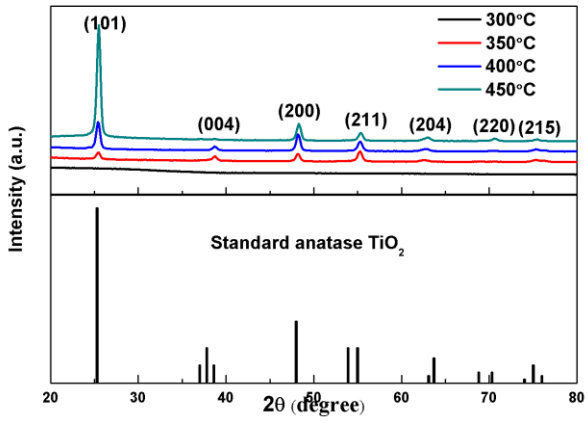

Fig. 5.4 XRD patterns of TiO_2 films synthesized at temperature of 300, 350, 400, and 450°C. (The below image was the XRD diffraction pattern for standard anatase TiO_2)

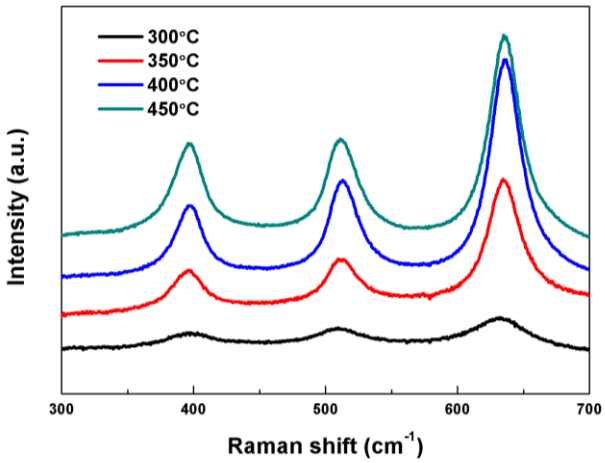

Fig. 5.5 Raman spectra of TiO_2 films synthesized at temperature of 300, 350, 400, and 450°C.

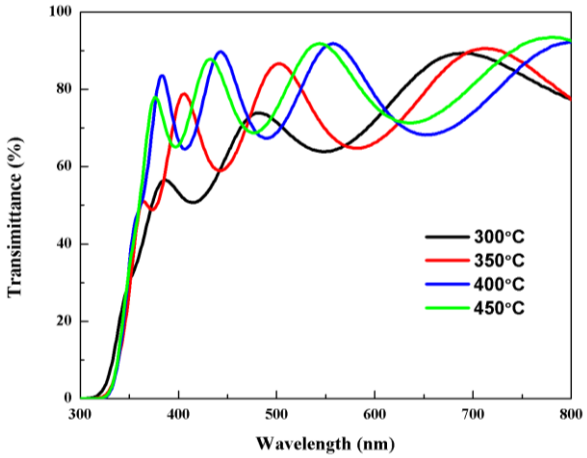

Fig. 5.6 Optical transmittance spectra of TiO_2 films synthesized at temperature of 300, 350, 400, and 450°C.

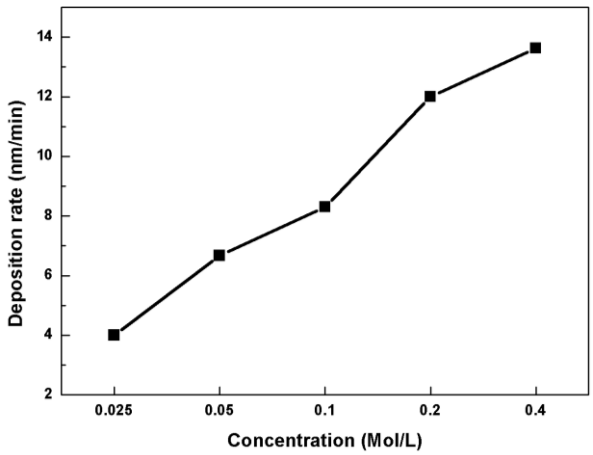

Fig. 5.7 Deposition rate of TiO_2 films synthesized at TTIP concentration of 0.025, 0.05, 0.1, 0.2, and 0.4 mol/L.

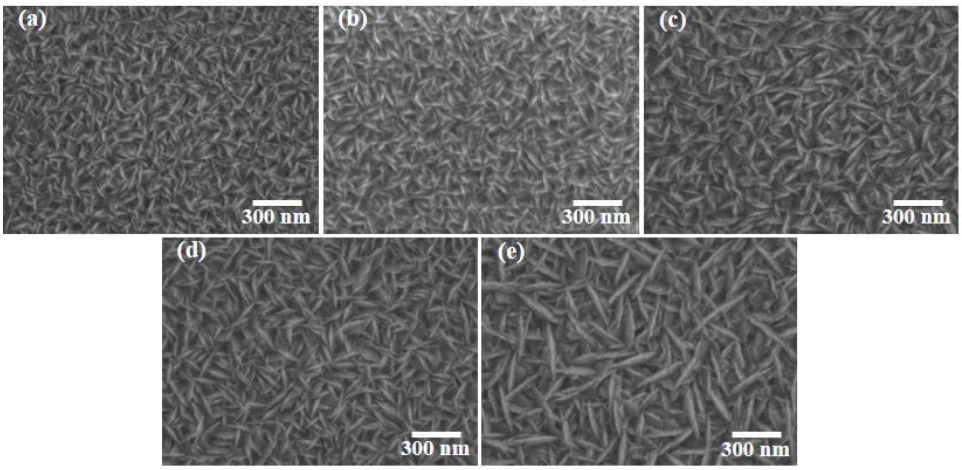

Fig. 5.8 SEM images of TiO_2 films synthesized at TTIP concentration of (a) 0.025, (b) 0.05, (c) 0.1, (d) 0.2, and (e) 0.4 mol/L.

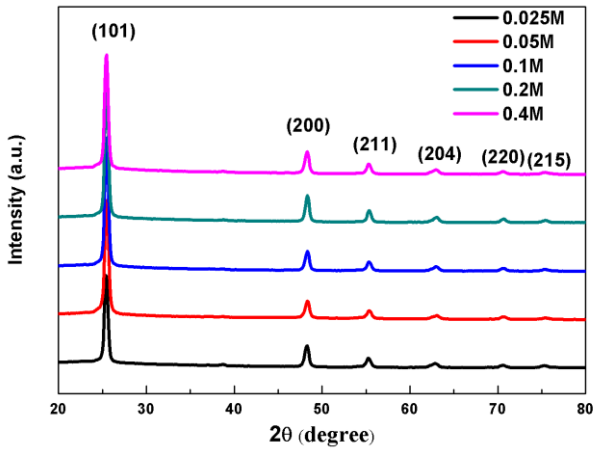

Fig. 5.9 XRD patterns of TiO_2 films synthesized at TTIP concentration of 0.025, 0.05, 0.1, 0.2, and 0.4 mol/L.

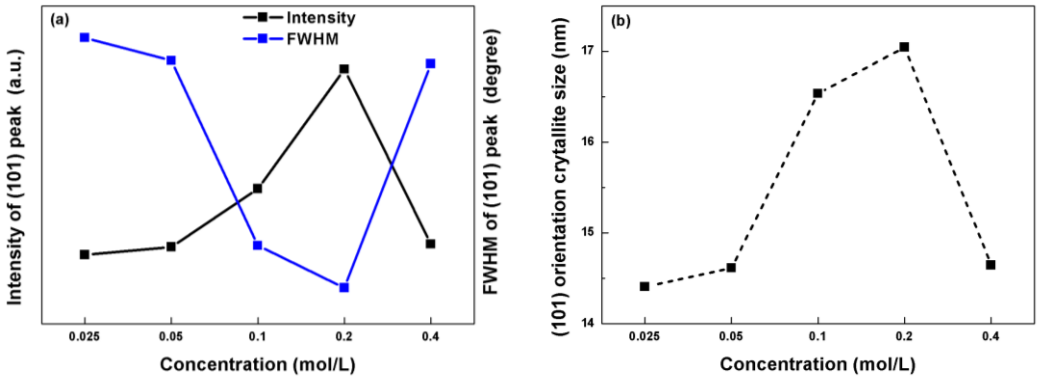

Fig. 5.10 (a) intensity and FWHM of (101) diffraction peak, and (b) (101) orientation crystallite size of TiO_2 films synthesized at TTIP concentration of 0.025, 0.05, 0.1, 0.2, and 0.4 mol/L.

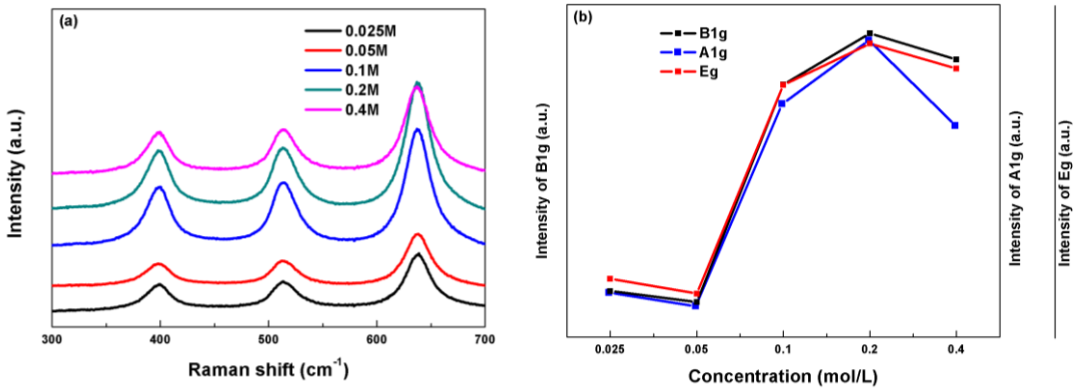

Fig. 5.11 (a) Raman spectra and (b) intensities of three Raman peaks of TiO_2 films synthesized at TTIP concentration of 0.025, 0.05, 0.1, 0.2, and 0.4 mol/L.

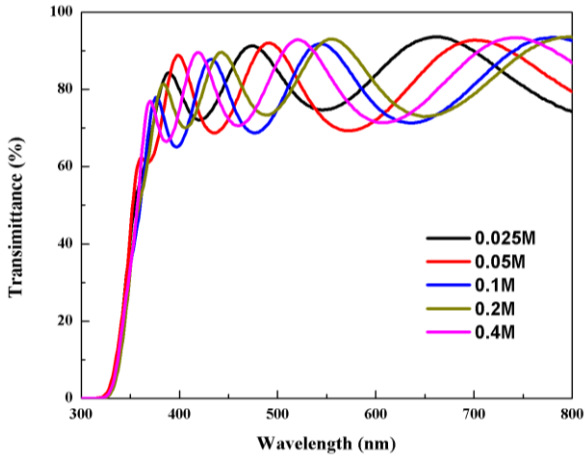

Fig. 5.12 Optical transmittance spectra of TiO_2 films synthesized at TTIP concentration of 0.025, 0.05, 0.1, 0.2, and 0.4 mol/L.

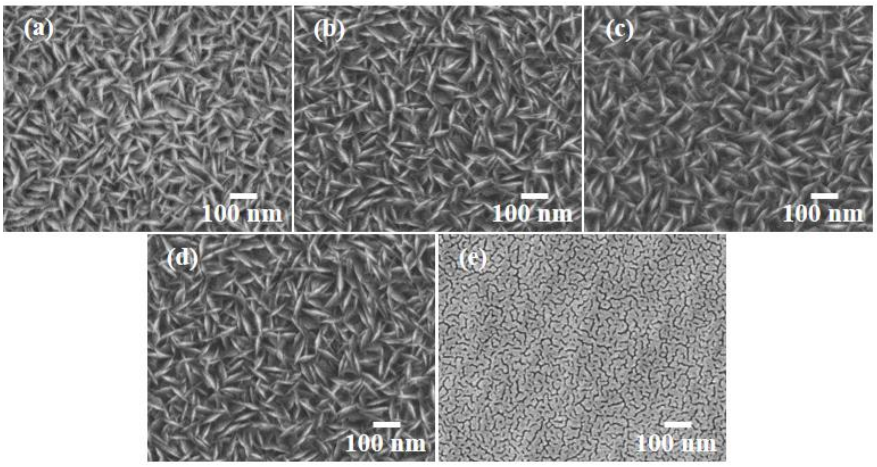

Fig. 5.13 SEM images of (a) as-deposited TiO_2 films and TiO_2 films after annealed at temperature of (b) 600, (c) 800, (d) 1000 and (e) 1100℃.

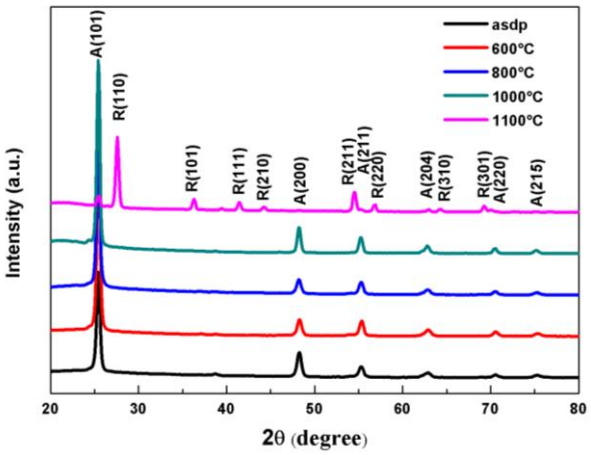

Fig. 5.14 XRD patterns of as-deposited TiO_2 films and TiO_2 films after annealed at temperature of 600, 800, 1000 and 1100℃.

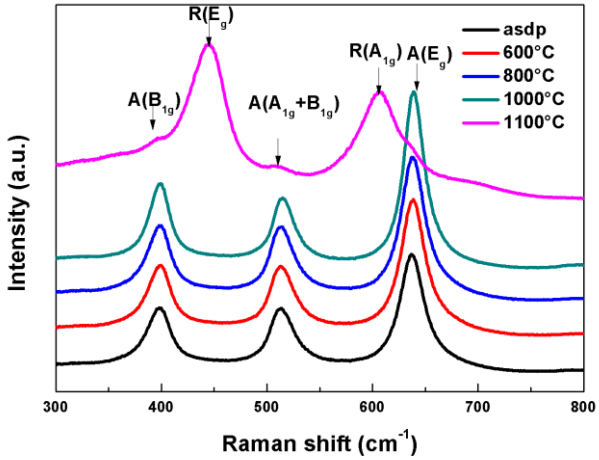

Fig. 5.15 Raman spectra of as-deposited TiO_2 films and TiO_2 films after annealed at temperature of 600, 800, 1000 and 1100℃.

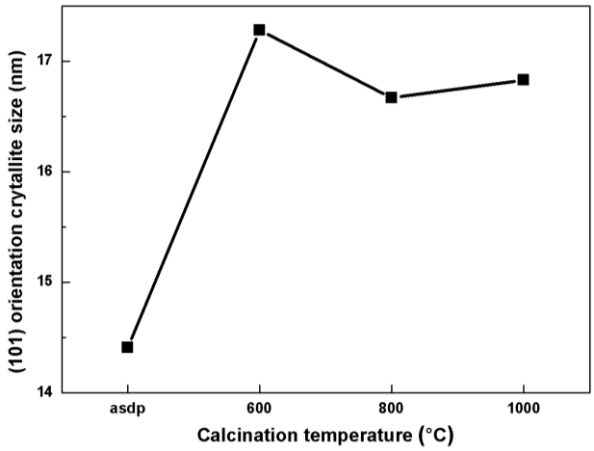

Fig. 5.16 Crystallite size of as-deposited TiO_2 films and TiO_2 films after annealed at temperature of 600, 800, and 1000℃

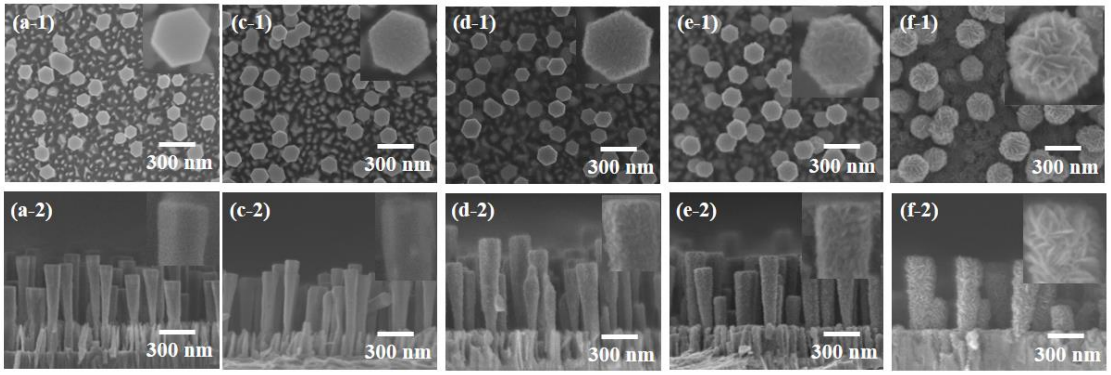

Fig. 5.17 (1) Top view and (2) cross section view of FE-SEM images of (a) as-fabricated ZnO nanorods and ZnO-TiO_2 core-shell nanorods fabricated at growth time of (b) 5, (c) 10, (d) 15, and (e) 20 minutes. (Inserted images showed a single core-shell nanorod under different growth time).

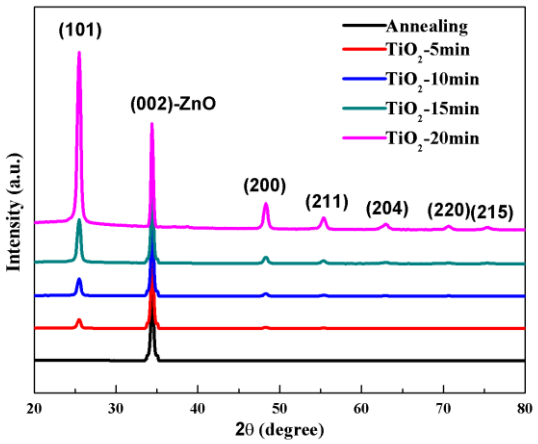

Fig. 5.18 XRD patterns of as-fabricated ZnO nanorods and ZnO-TiO_2 core-shell nanorods fabricated at growth time of 5, 10, 15, and 20 minutes.

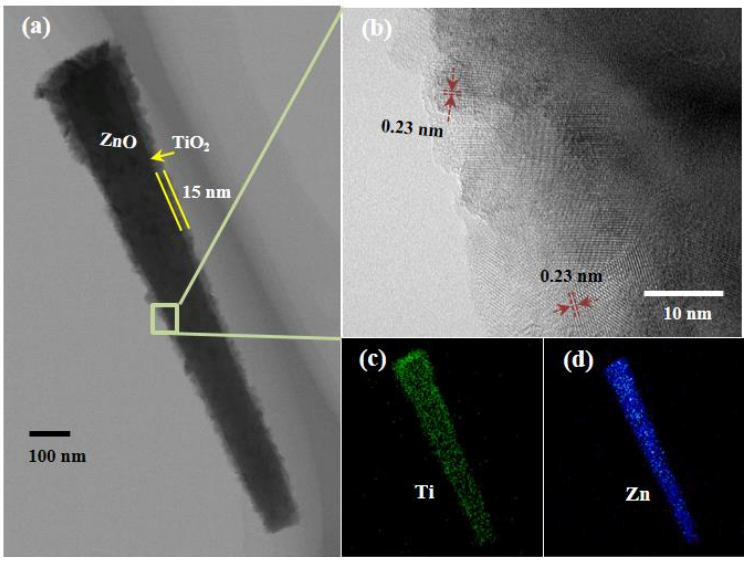

Fig. 5.19 (a) TEM image, (b) HRTEM image, EDX elemental mapping of (c) Ti, and (d) Zn of a single ZnO-TiO_2 core-shell nanorod fabricated at growth time of 15 minutes.

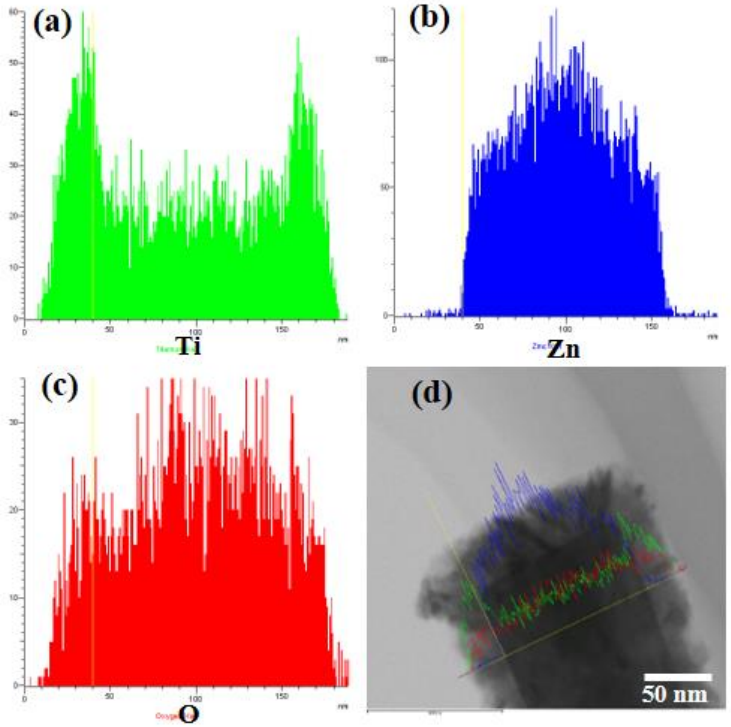

Fig. 5.20 Line-scan EDX-TEM images of ZnO-TiO_2 core-shell nanorods fabricated at growth time of 15 minutes.

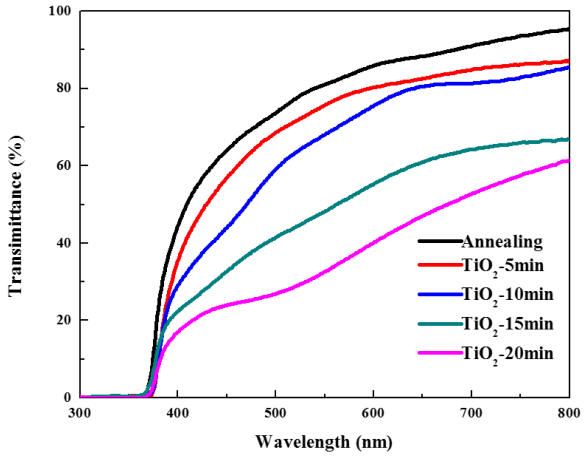

Fig. 5.21 Optical transmittance spectra of as-fabricated ZnO nanorods and ZnO-TiO_2 core-shell nanorods fabricated at growth time of 5, 10, 15, and 20 minutes.

5.5 References

[1] A. Kołodziejczak-Radzimska, and T. Jesionowski. *Mater.* 7 (2014) 2833-2881.

[2] P. Tiwana, P. Docampo, M.B. Johnston, H.J. Snaith, and L.M. Herz. *ACS nano,* 5 (2011) 5158-5166.

[3] I. Gonzalez-Valls, and M. Lira-Cantu. *Energy Environ. Sci.* 2 (2009) 19-34.

[4] L. Lu, R. Li, K. Fan, and T. Peng. *Solar Energy,* 84 (2010) 844-853.

[5] S.B. Ambade, R.S. Mane, A.V. hule, M.G. Takwale, A. Abhyankar, B. Cho, and S.H. Han. *Scr. Mater.* 61 (2009) 12-15.

[6] F. Yan, L. Huang, J. Zheng, J. Huang, Z. Lin, F. Huang, and M. Wei. *Langmuir,* 26 (2010) 7153-7156.

[7] H. Horiuchi, R. Katoh, K. Hara, M. Yanagida, S. Murata, H. Arakawa, and M. Tachiya. *J. Phys. Chem. B,* 107 (2003) 2570-2574.

[8] M. Law, L.E. Greene, A. Radenovic, T. Kuykendall, J. Liphardt, and P Yang. *J. Phys. Chem. B,* 110 (2006) 22652-22663.

[9] A.K. Chandiran, M. Abdi-Jalebi, M.K. Nazeeruddin, and M. Grätzel. *ACS nano,* 8 (2014) 2261-2268.

[10] P. Atienzar, T. Ishwara, B.N. Illy, M.P. Ryan, B.C. O'Regan, JR Durrant, and J. Nelson. *J. Phys. Chem. Let.* 1 (2010) 708-713.

[11] Y. Feng, X. Ji, J. Duan, J. Zhu, J. Jiang, H. Ding, G. Meng, R. Ding, J. Liu, A. Hu, and X. Huang. *J. Solid State Chem.* 190 (2012) 303-308.

[12] K. Prabakar, M. Son, W.Y. Kim, and H. Kim. *Mater. Chem. Phys.* 125.(2011) 12-14.

[13] R. Zhao, L. Zhu, F. Cai, Z. Yang, X. Gu, J. Huang, and L. Cao. *Appl. Phys. A,* 113 (2013) 67-73.

[14] G.K.L. Goh, H.Q. Le, T.J. Huang, B.T.T. Hui. *J. Solid State Chem.* 214 (2014) 17-23.

[15] L.E. Greene, M. Law, B.D. Yuhas, and P. Yang. *J. Phys. Chem. C,* 111 (2007) 18451-18456.

[16] T. Kawaharamura, and S. Fujita. *Phys. Status Solidi C,* 5 (2008) 31383140.

[17] T. Kawaharamura. *Jpn J. Appl. Phys.* 53, (2014) 05FF08.

[18] X. Li, C. Li, T. Kawaharamura, D. Wang, N. Nitta, M. Furuta, H. Furuta, and A. Hatta. *Tran Mater. Res. Soc. Jpn.* 39 (2014) 161-164.

[19] X. Li, C. Li, T. Kawaharamura, D. Wang, N. Nitta, M. Furuta, H. Furuta, and A. Hatta. *Nanosci. Nanotech. Let.* 6 (2014) 174-180.

[20] X. Li, C. Li, S. Hou, A. Hatta, J. Yu, and N. Jiang. *Compos. Part B Eng.* 74 (2015) 147-152.

[21] S. Hou, and C. Li. *Thin Solid Films,* 605 (2016) 37-43.

[22] K.L. Siefering, and G.L. Griffin. *J. Electrochem. Soc.* 137 (1990) 1206-1208.
[23] K.H. Ahn, Y.B. Park, and D.W. Park, *Surf. Coat. Technol.* 171 (2003) 198-204.

Chapter 6

Fabrication and evaluation of ZnO based DSSC

6.1 Introduction

In last three chapters, ZnO nanorods were fabricated by different methods with the final application in DSSCs. Generally, the characterization of tranditional DSSC contains illuminated I-V, where the cell is illuminated at simulated sunlight and basic parameters measured [1]; dark I-V, where the cell is in the dark and IV characteristic tranced [2]; and I_{sc}-V_{oc}, where short circuit current (I_{sc}) and the open circuit voltage (V_{oc}) are recorded at different illumination levels [3].

The most common characterization for DSSC is the illuminated I-V (J-V). Several important parameters including I_{sc}, V_{oc}, fill factor (FF), and overall conversion efficiency etc. are used to characterize solar cells. I_{sc} and V_{oc} are the common parameters of the circuit. FF is a parameter in conjunction with I_{sc} and V_{oc} determines the ratio of maximum obtainable power from a solar cell. FF is defined based on following equations (6.1) [4].

$$\mathrm{FF} = \frac{V_{MP} I_{MP}}{V_{OC} I_{SC}} \tag{6.1}$$

Here, V_{MP} and I_{MP} is the voltage and current of maximum power, respectively. The efficiency of a solar cell is determined as the fraction of incident power which is converted to electricity and is defined as:

$$\eta = \frac{V_{OC} I_{SC} FF}{P_{in}} \tag{6.2}$$

Here, P_{in} is the incident power. In addition, series resistance (Rs) and shunt resistance (Rsh) are also very important for the characterization of DSSC. In general, very high values of R_s and very low values of R_{sh} reduce I_{sc} and V_{oc}, respectively [5].

In this chapter, ZnO nanorods and TiO_2 coated ZnO nanorods fabricated on ZnO based substrates were used as the photoanode in DSSCs. The improvements of ZnO based DSSCs in terms of ZnO nanorods had been investigated.

6.2 Demonstration of DSSC based on ZnO nanostructures

6.2.1 Experiments

ZnO nanorods had been fabricated on AZO or GZO substrate by multi-annealing and CBD

methods, which was discussed in Chapter 3 and 4. Photoanodes using ZnO nanorods on AZO or GZO substrate were applied to fabricate DSSC.

Firstly, the photoanodes were immersed in an ethanoic 0.5 mM N719 (Sigma Aldrich, St. Louis, MO) solution for 12 hours. Then the dye-adsorbed photoanodes were assembled with a platinum coated counter-electrode to form a sandwich-structured DSSC. The cell was filled with the electrolyte solution which contained 0.05 M iodine and 0.1 M lithium iodine. The structure of DSSC was GZO//ZnO nanorods//N719//I^-/I_3^-//Pt//ITO.

6.2.2 Results and discussion

Demonstrated DSSCs using obtained ZnO nanorods on transparent conductive GZO substrates as photoanodes was fabricated. Fig. 6.1 showed the J-V curves of ZnO-based DSSCs using ZnO nanorods with different length as photoanode material. ZnO nanorods were vertical aligned on GZO substrates. The length of different ZnO nanorods were 1.527 and 865 nm, respectively shown in the inserted images in Fig. 6.1. The overall conversion efficiencies of demonstrated DSSC with long and short ZnO nanorods were 3.19% and 1.31%, respectively, shown in Table 6.1. It was found that the short circuit current density (J_{sc}) was tremendously increased from of 5.01 to 8.11 mA/cm^2 and the open circuit voltage (V_{oc}) was slightly improved from 0.60 to 0.64 V. Supprisingly, The fill factor (FF) was largely improved from 0.43 to 0.62. Therefore, The length of ZnO nanorods significantly improved the performance of DSSC including J_{sc}, V_{oc}, and fill factor. For DSSC, large surface area meant more dye molecules could be attached on ZnO nanorods, which would be tremendously increased the current density. The imrovement of FF indicated that the recombination between electron and holes, and scattering during electron transportation were less.

Table 6.1 Characteristics of DSSCs based on ZnO nanorods with length of (a) 1527 nm and (b) 865 nm.

Sample	J_{sc} (mA·cm^{-2})	V_{oc} (V)	FF	PCE (%)
Short nanorods	5.01	0.60	0.43	1.31
Long nanorods	8.11	0.64	0.62	3.19

The J-V curves of ZnO-based DSSCs using ZnO nanorods with or without oxygen annealing as photoanode material was shonw in Fig. 6.2. After oxygen annealing, no visible morphology change was found from ZnO nanorods, which was discussed in Chapter 3. The length of ZnO nanorods were 1.527, shown in the inserted images in Fig. 6.2. After oxygen annealing, great improvement was found from J_{sc}, which was increased from 6.73 to 8.11 mA/cm^2. Based on the

research of oxygen annealing effects of ZnO nanorods in Chapter 3, oxygen vacancies were reduced and the crystallinity of ZnO nanorods was slightly improved. Therefore, the recombination of electron-hole and electron scattering in ZnO nanorods were reduced, thus enhancing the current density. However, the V_{oc} and FF were hardly changed regardless of oxygen annealing. Therefore, the overall conversion efficiencies of demonstrated DSSCs were improved from 2.68 to 3.19% for ZnO nanorods after oxygen annealing.

Table 6.2 Characteristics of DSSCs based on ZnO nanorods with or without O_2 post-annealing treatment.

Sample	J_{sc} (mA·cm^{-2})	V_{oc} (V)	FF	PCE (%)
Without O_2 treatment	6.73	0.63	0.63	2.68
With O_2 treatment	8.11	0.64	0.62	3.19

ZnO nanorods fabricated by CBD method were also used to demonstrate DSSC. Fig. 6.3 showed J-V curves of DSSCs using ZnO nanorods with different length as photoanode material. ZnO nanorods grown by CBD with different growth time from 5 to 20 hours. It was found that the length of ZnO nanorods was 784, 1242, 1913, and 3775 nm in the order of reaction time of 5, 10, 15, and 20 hours, respectively. As reaction time increased, the J_{sc} was increased from 0.75 to 1.97 mA/cm^2, which meant large surface area increased the current density. It was also found that the V_{oc} was also almost similar due to the fact that voltage barrier was influenced by the reaction time. The overall conversion efficiencies of demonstrated DSSCs were improved from 0.12 to 0.35%, which was much lower than that of DSSCs using ZnO nanorods by multi-annealing compared to Fig. 6.1. The reasons could be attributed to the worse crystallinity of ZnO nanorods by CBD, which caused the electron scattering and recombination increase. Therefore, the fill factor of DSSC based on ZnO nanorods by CBD was much lower than that by mutli-annealing. As reaction time extended, the overall conversion efficiency improved. However, the FF reached the maximum of 0.41 for ZnO nanorods in growth of 10 and 15 hours. It might be because of the relatively large surface area and high transmittance.

Table 6.3 Characteristics of DSSCs based on ZnO nanorods by CBD method.

Sample	**J_{sc} (mA·cm^{-2})**	**V_{oc} (V)**	**FF**	**PCE (%)**
CBD-5h	0.75	0.55	0.29	0.12
CBD-10h	0.79	0.58	0.41	0.19
CBD-15h	0.98	0.57	0.41	0.23
CBD-20h	1.97	0.62	0.28	0.35

6.2.3 Summary

In summary, ZnO nanorods fabricated by both multi-annealing and CBD methods could be applied to DSSCs. Large surface of ZnO nanorods contributed to the higher current density. Oxygen annealing reduced the defects and improved the crystallinity. All of these reduced the electron-hole recombination and electron scattering during electron transportation. High transmittance allowed more photons to be absorbed by more dye molecules. Therefore, the short circuit current density, fill factor and overall conversion efficiency of DSSC were improved.

6.3 Demonstration of DSSC based on ZnO-TiO_2 core-shell nanorods

6.3.1 Experiments

The fabrication of ZnO-TiO_2 core-shell nanorods on AZO film substrate were discussed in Chapter 5. Here, core-shell nanorods on AZO film were used to fabricate a sandwich-structured DSSC. N719 (Sigma Aldrich, St. Louis, MO) was used as dye sensitizer in ZnO based DSSC. The platinum coated ITO glass was used as the counter-electrode. The electrolyte solution which contained 0.05 M iodine and 0.1 M lithium iodine was applied as the electrolyte.

6.3.2 Results and discussion

Table 6.4 Characteristics of DSSCs based on as-fabricated ZnO nanorods and ZnO-TiO_2 core-shell nanorods.

Sample	J_{sc} (mA·cm^{-2})	V_{oc} (V)	FF	PCE (%)
No TiO_2	5.01	0.60	0.43	1.31
TiO_2-5min	5.79	0.62	0.50	1.57
TiO_2-10min	6.10	0.62	0.58	2.12
TiO_2-15min	6.73	0.63	0.63	2.68
TiO_2-20min	6.42	0.64	0.63	2.57

As discussed in Chapter 5, pure anatase TiO_2 films with sheet-like grains were coated on ZnO nanorods, shown in inserted images of Fig. 6.4. It was found that thickness of TiO_2 shell increased with the increase of growth time. Fig. 6.4 showed the J-V curves of DSSCs based on pure ZnO nanorods and ZnO-TiO_2 core-shell nanorods. Table 6.4 showed photovoltaic parameters including J_{sc}, V_{oc}, FF, and photoelectric conversion efficiency (PCE) of DSSCs based on pure ZnO nanorods and ZnO-TiO_2 core-shell nanorods. For DSSC using pure ZnO nanorods, it showed J_{sc} of 5.01 mA/cm^2, V_{oc} of 0.60 V, FF of 0.43, and an overall conversion

efficiency of 1.31%. The addition of TiO_2 shells on ZnO nanorods resulted in considerable improvement in J_{sc}, V_{oc} and FF. As shell thickness increased from 0 to 25 nm, J_{sc} increased to 0.37 to 1.62 mA/cm^2 and V_{oc} slightly increased to 0.02 to 0.04 V. FF jumped to 0.63 from 0.43, which was a huge improvement of 47%. Overall, the overall conversion efficiency double increased with TiO_2 shell thickness of 15 nm, jumping from 1.31 to 2.68%.

This ZnO-TiO_2 core-shell nanorods was supposed to help utilize the favorable electron mobility and diffusion rate of ZnO nanorods without compromising the negative effects of Zn^{2+}/dye agglomeration and surface recombination. There were several reasons to account for the greatly improved performance of DSSC. Firstly, TiO_2 shell prevented the ZnO surface being dissolved in acidic dye solutions and the Zn^{2+}/dye complex at the nanorods surface no longer existed. Secondly, the TiO_2 shell has much lower electron-hole recombination rate than ZnO nanorods, which could greatly improve Jsc and FF. Thirdly, TiO_2 shell could also suppressed the recombination rate by passivating the defects on the interface between ZnO nanorods and TiO_2 shell. Finally, carrier mobility in ZnO was much faster than that in TiO_2. Therefore, the charge transfers from dye to conductive band of TiO_2 and then through ZnO nanorods to AZO substrate was significantly improved.

6.3.3 Summary

In summary, DSSC using anatase TiO_2 coated ZnO nanorods as photoanode material had been demonstrated. The morphology of ZnO nanorods were greatly modified with TiO_2 layers under different growth time. TiO_2 shell was uniformly coated the surface of ZnO nanorod. TiO_2 shell was demonstrated to improve J_{sc} from 5.01 to 6.73 mA/cm^2, the fill factor from 0.43 to 0.63, and overall conversion efficiency from 1.31 to 2.68%. TiO_2 coated ZnO nanorods exhibited a dramatic improvement in J_{sc}, FF, and PCE, which has great promising in improving the performance of photovoltaic devices.

6.4 Conclusions

In this chapter, fabricated ZnO nanorods by both multi-annealing and CBD methods and TiO_2 coated ZnO nanorods by multi-annealing method were applied in DSSCs. The characterization of DSSCs using ZnO nanorods as photoanodes were evaluated.

1) ZnO nanorods with different surface area, oxygen annealing and different fabrication methods were investigated in DSSC demonstration. Large surface area of ZnO nanorods meant more dye molecules were absorbed, thus increasing the photo generated current population. Oxygen vacancies were reduced by oxygen annealing, which increased the crystallinity and

reduced the recombination centre. Therefore, large surface area and oxygen annealing contributed to the higher current density, higher fill factor and the overall conversion efficiency. DSSC using ZnO nanorods fabricated by multi-annealing showed much higher efficiency than that by CBD method.

2) In order to overcome the disadvantages of ZnO nanorods used in DSSC, TiO_2 shell was coated on ZnO nanorods to improve the efficiency of DSSC. It was found that pure anatase TiO_2 shell with sheet-like grains was coated on ZnO nanorods. As growth time increased, the thickness of TiO_2 shell increased. Pure anatase TiO_2 shell provented ZnO surface from being dissolved in acidic dye solutions and reduced the electron-hole recombination. TiO_2 shell worked as a barrier that blocked the recombination between electrons and dyes. Therefore, after coated with TiO_2 shell, J_{sc} was improved from 5.01 to 6.73 mA/cm^2 and the fill factor was improved from 0.43 to 0.63 with the increase of the growth time from 0 to 20 min. Moreover, the overall conversion efficiency was increased from 1.31 to 2.68%.

The performance of ZnO based DSSC was improved by enlarging the surface area, reducing the oxygen vacancies and coating with TiO_2 shell. In the future, performance of DSSC is expected to further improved by optimizing the photoanodes and dyes.

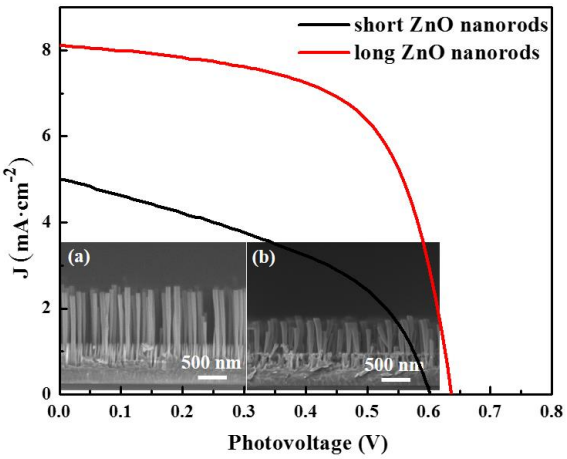

Fig. 6.1 J-V characteristics of demonstrated DSSC based on ZnO nanorods fabricated by multi-annealing method with length of (a) 1527 nm and (b) 865 nm.

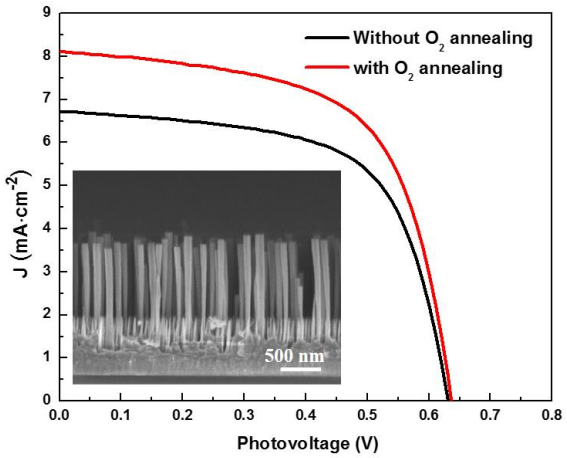

Fig. 6.2 J-V characteristics of demonstrated DSSC based on ZnO nanorods fabricated by multi-annealing method with or without O_2 post-annealing treatment.

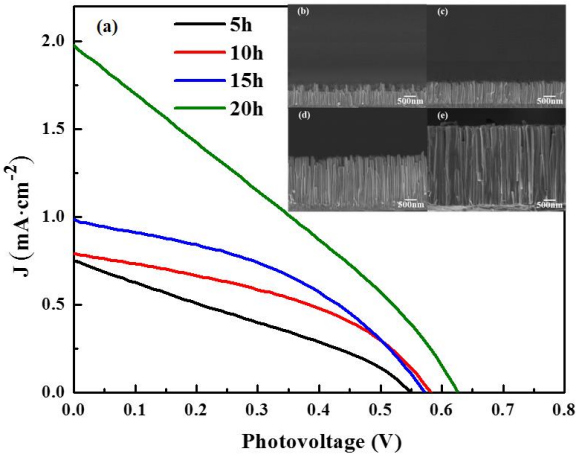

Fig. 6.3 J-V characteristics of demonstrated DSSC based on ZnO nanorods after growth time of (a) 5, (b) 10, (c) 15, and (d) 20 hours by CBD method.

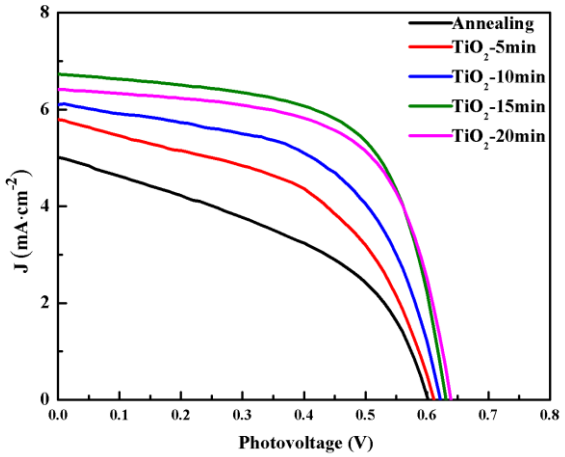

Fig. 6.4 J-V characteristics of demonstrated DSSCs based on as-fabricated ZnO nanorods and ZnO-TiO_2 core-shell nanorods fabricated by mist CVD at growth time of 5, 10, 15, and 20 minutes.

6.5 References

[1] F.A. Lindholm, J.G. Fossum, and E.L. Burgess. *IEEE Trans. Electron Dev.* 26 (1979) 165–171.
[2] J. Zhao, A. Wang, X. Dai, M.A. Green, and S.R. Wenham. *22nd IEEE PV Specialists Conference.* (1991) 399-402.
[3] M. Wolf, and H. Rauschenbach. *Adv. Energy Convers.* 3 (1963) 455-479.
[4] M.A. Green. *Solid-State Electron.* 24 (1981) 788-789.
[5] P. Singh, and N.M. Ravindra. *Emerg. Mater. Res.* 1 (2012) 33-38.

Chapter 7

Conclusions

In this thesis, fabrication of ZnO-based photoanodes in applications of DSSC was investigated.

ZnO based transparent conductive substrates were deposited by sputtering method to replace the conventional ITO and FTO substrates. The vertical alignment of ZnO nanorods was well controlled on ZnO based substrates via multi-annealing and chemical bath deposition methods. The electron recombination of ZnO nanorods in application of DSSC were reduced by coating with anatase TiO_2 shell. The overall conversion efficiency of DSSC was improved twice by coating with anatase TiO_2 shell.

Therefore, the main conclusions of this thesis were summarized as followed:

1. Deposition of transparent conductive ZnO based substrates

Transparent conductive ZnO based films were deposited on glass substrates by sputtering methods. The structural, optical and electrical properties of ZnO films were greatly influenced via doped with aluminium and gallium. The aluminium and gallium dopant not only improved the crystallinity of ZnO film, but also the resistivity and electron mobility. It was found that as film thickness increased from 50 to 300 nm, the crystallinity of AZO and GZO films was improved, resistivity decreased, and electron mobility increased. AZO and GZO films showed strongly c-axis growth direction and high transmittance of over 80% in visible range. AZO and GZO films with thickness of 300 nm showed comparable mobility and resistivity to commercial ITO films. Therefore, both films could replace ITO substrate to be applied as the TCO substrates for electrodes in DSSC.

2. Fabrication of vertical aligned ZnO nanorods on AZO and GZO substrates

2.1 ZnO nanorods fabricated by multi-annealing method

ZnO nanorods were fabricated on different substrates by multi-annealing method. The effects of substrates, oxygen treatment, and annealing on morphological, structural, and optical properties of ZnO nanorods were investigated.

1) ZnO nanorods were fabricated on ITO, AZO and GZO substrates by multi-annealing method. ZnO nanorods fabricated on AZO and GZO were vertical aligned while those on ITO were not. Due to AZO and GZO had good c axis growth, ZnO nanorods followed the same growth direction to underneath AZO and GZO. Low mismatch between ZnO film and AZO or

GZO film contributed to vertical alignment of ZnO nanorods. Because of the vertical alignment, ZnO nanorods fabricated on AZO and GZO had better crystallinity and higher optical transmittance than those on ITO.

2) Oxygen treatment was applied to ZnO nanorods fabricated by multi-annealing. PL properties of ZnO nanorods were significantly influenced by oxygen annealing. Zinc interstitials and oxygen vacancies in ZnO nanorods were oxidized after oxygen treatment, which enhanced the UV emission and reduced the green-blue emission. Moreover, the crystallinity and optical transmittance of ZnO nanorods were slightly improved after oxygen treatment.

3) ZnO nanorod growth was affected by annealing process. Vertical alignment of ZnO nanorods was achieved on AZO substrates. Diameter and length of ZnO nanorods were greatly increased with the increase of annealing process. Crystallinity, intensities of both UV emission and visible emission for ZnO nanorods increased as annealing time extended.

2.2 ZnO nanorods fabrication by chemical bath deposition

ZnO nanorods were fabricated on transparent conductive AZO films by chemical bath deposition method. The effects of the seed layer thickness, precursor concentration and growth time on morphological, structural, and optical properties of ZnO nanorods were investigated in detail.

1) The effects of AZO film thickness on ZnO nanorods growth were investigated. As AZO film thickness increased, the grain size of AZO films increased, which resulted in the diameter of ZnO nanorods was increased. ZnO nanorods were vertical aligned fabricated on AZO films with different thicknesses. ZnO nanorods showed high transmittance of over 65% in visible range.

2) The effects of concentration of $Zn(NO_3)_2 \cdot 6H_2O$ on ZnO nanorods growth were investigated. As the concentration of $Zn(NO_3)_2 \cdot 6H_2O$ increased, the diameter of ZnO nanorods increased greatly, the length increased to the maximum at concentration ratio of 2:1. The crystallinity was also improved and the intensity of visible emission increased due to the excessive supply of zinc source, which formed more zinc interstitials in ZnO nanorods.

3) The effects of concentration of HMT on ZnO nanorods growth were investigated. The diameter of ZnO nanorods was increased from the ratio of 2:0.25 to 2:1 and then decreased at 2:2. The crystallinity of ZnO nanorods was also firstly increased and then decreased. The intensity of visible PL emission was decreased as concentration of HMT increased, which was due to the increasing concentration of OH^- resulted in less zinc interstitials formed.

4) The effects of reaction time on ZnO nanorods growth were investigated. As reaction time increased, ZnO nanorods kept vertical growth direction and the length increased greatly. The crystallinity of ZnO nanorods was improved and intensity of visible emission was increased.

3. Fabrication of TiO_2 films by mist CVD method

Pure anatase TiO_2 films were synthesized by mist CVD method. The effects of experimental parameters including synthesis temperature, TTIP concentration, and annealing temperature on TiO_2 film were investigated in detail.

1) Morphological and structural properties of TiO_2 films were influenced by synthesis temperature. As synthesis temperature increased from 300 to 450℃, surface of TiO_2 film was changed from particles to long and thin sheet-like grains. TiO_2 films were pure anatase and the crystallinity of TiO_2 films became better.

2) Morphological, structural and optical properties of TiO_2 films was dependent on the TTIP concentration. It was found that length of sheet-like grain was greatly increased, indicating the higher formation rate of sheet-like grains with the increase of concentration from 0.025 to 0.2 mol/L. Furthermore, TiO_2 kept the anatase structure and crystallinity of TiO_2 film was slightly increased.

3) Annealing treatment was applied to TiO_2 film to investigate the thermal stability. No visible change was observed from the morphology of TiO_2 film when the annealing temperature ranged from 600 to 1000℃. XRD data and Raman spectra confirmed that anatase structure was kept at 1000℃. When temperature increased to 1100℃, sheet-like grains merged into a large grains. The rutile diffraction peaks and Raman peaks were found.

4. Fabrication of TiO_2 shell on ZnO nanorods by mist CVD method

In order to over the disadvantages of ZnO nanorods applied in DSSCs, TiO_2 shell was coated on ZnO nanorods by mist CVD method. The morphological, structural and optical properties of ZnO nanorods were greatly modified with TiO_2 layers under different deposition time. The diameter of ZnO-TiO_2 core-shell nanorods was greatly increased with the increased of deposition time. The length of core-shell nanorods slightly increased. XRD patterns and EDX confirmed that pure anatase TiO_2 shell was uniformly covered the surface of ZnO nanorod. The TiO_2 coated ZnO nanorods were expected to improve the performance of ZnO based solar cell.

5. Fabrication and evaluation of ZnO based DSSC

ZnO based DSSCs were demonstrated using ZnO nanorods fabricated by both multi-annealing and CBD methods and TiO_2 coated ZnO nanorods by multi-annealing method.

1) Large surface area of ZnO nanorods increased the photo generated current population. Oxygen vacancies were reduced by oxygen annealing, which increased the crystallinity and reduced the recombination centre. Therefore, large surface area and oxygen annealing contributed to the higher current density, higher fill factor and the overall conversion efficiency. The highest overall efficiency of 3.19% was obtained from ZnO nanorods fabricated on GZO

substrates with a fill factor of 0.64.

2) Pure anatase TiO_2 shell provented ZnO surface from being dissolved in acidic dye solutions and reduced the electron-hole recombination. TiO_2 shell worked as a barrier that blocked the recombination between electrons and dyes. Compared DSSC using pure ZnO with that using ZnO-TiO_2 core-shell, J_{sc} was improved from 5.01 to 6.73 mA/cm^2 and the fill factor was improved from 0.43 to 0.63 with the increase of the growth time from 0 to 20 min. The overall conversion efficiency from 1.31 to 2.68%.

List of publications

(A) Reviewed jounal papers

First author:

1) Fabricated ZnO nanorods on transparent conductive Ga-doped ZnO film as photoanodes applying for dye-sensitized solar cell.
Shengwen Hou, Chaoyang Li
Nanoscience and Nanotechnology Letters, 8, 561-566 (2016).

2) Aluminum-doped ZnO thin film as seeds layer effects on the alignment of zinc oxide nanorods synthesized in the chemical bath deposition.
Shengwen Hou, Chaoyang Li
Thin Solid Films, 605, 37-43 (2015).

3) Controllable ZnO nanorods growth by chemical bath deposition.
Shengwen Hou, Chaoyang Li, G.I.P. De Silva
Transactions of the Materials Research Society of Japan, 40, 187-190 (2015).

4) ZnO-TiO2 core-shell nanorods fabricated by mist chemical vapor deposition in application of dye-sensitized solar cell,
Shengwen Hou, Chaoyang Li
(To be submitted)

5) High temperature stabilized anatase TiO2 films synthesized by mist chemical vapor deposition method,
Shengwen Hou, Chaoyang Li
(To be submitted)

Co-author:

1) Comparison of the photoluminescence properties of ZnO nanorods synthesized by multi-annealing and chemical bath deposition methods.
Chaoyang Li, **Shengwen Hou**

ITE Transactions on Media Technology and Applications, 4, 320-325 (2016).

2) Well-controllable fabrication of aligned ZnO nanorods for dye-sensitized solar cell application.
Chaoyang Li, **Shengwen Hou**, Xin Li
MRS Proceedings Cambridge University Press, 1805, mrss15-2124440 (2015).

3) Thickness of ITO thin film influences on fabricating ZnO nanorods applying for dye-sensitized solar cell.
Xin Li, Chaoyang Li, **Shengwen Hou**, Akimitsu Hatta, Jinhong Yu, Nan Jiang
Composites Part B: Engineering, 74, 147-152 (2015).

(B) International and domestic conferences

International conferences with proceeding as first author:

1) Mg-, Al-, and Ga-doped ZnO films as seed layers for ZnO nanorods synthesized in chemical bath deposition.
Shengwen Hou, Chaoyang Li
The 23rd Annual International Conference on Composites and Nano Engineering, July 12-18, 2015, Chengdu, China. (Oral presentation)

2) Self-assembled ZnO nanorods synthesis improved by conductive oxide films in chemical bath deposition.
Shengwen Hou, Chaoyang Li
The 2015 European Materials Research Society Spring Meeting and Exhibition, May 11-15, 2015, Lille, France. (Poster presentation)

3) Concentration dependence of precursors for zinc oxide nanorods fabricated by chemical bath deposition.
Shengwen Hou, Chaoyang Li
China-Japan Innovation Forum, November 5, 2014, Hefei, China. (Oral presentation)

4) Controllable ZnO nanorods growth by chemical bath deposition.
Shengwen Hou, Chaoyang Li, G.I.P. De Silva,
International Union of Materials Research Societies-International Conference in Asia 2014,

August 24-30, 2014, Fukuoka, Japan. (Oral presentation)

International conferences with proceeding as co-author:

1) Photoluminescence properties of ZnO nanorods growth vertically on transparent and conductive Al-doped ZnO substrates.
Chaoyang Li, **Shengwen Hou**
Pacific Rim Meeting on Electrochemical and Solid-State Science 2016, October 2-7, 2016, Hawaii, USA.

2) Ga-doped zinc oxide films as transparent and conductive substrates applying in dye-sensitized solar cell.
Chaoyang Li, **Shengwen Hou**
32nd European Photovoltaic Solar Energy Conference and Exhibition, June 20-24, 2016, Munich, Germany.

3) Photoluminescence and structural properties of well-arrayed ZnO nanorods growth directly on the transparent and conductive Al-doped ZnO substrates.
Chaoyang Li, **Shengwen Hou**
Display Week 2016 International Symposium, Seminar and Exhibition, May 22-27, 2016, San Francisco, USA.

4) Comparison the photoluminescence properties of ZnO nanorods on AZO substrates synthesized by different methods.
Chaoyang Li, **Shengwen Hou**
The 22nd International Display Workshops, December 9-11, 2015, Otsu, Japan.

5) Fabrication and characterization of ZnO nanorods on TCO glass for photovoltaics application.
Chaoyang Li, **Shengwen Hou**
The 14th International Union of Materials Research Societies-International Conference on Advanced Materials, October 25-29, 2015, Jeju, Korea.

6) Fabrication of ZnO nanorods on AZO substrates as photoelectrodes for dye-sensitized solar cell application.
Chaoyang Li, **Shengwen Hou**

31st European Photovoltaic Solar Energy Conference and Exhibition, September 14-18, 2015, Hamburg, Germany.

7) Fabrication of high performance metal oxide transparent thin film for OLED application.
Chaoyang Li, **Shengwen Hou**
International Display Manufacturing Conference & 3D Systems and Applications 2015, August 20-28, 2015, Nangang, Taiwan.

8) Well-controllable fabrication of aligned ZnO nanorods for dye-sensitized solar cell application.
Chaoyang Li, **Shengwen Hou**, Xin Li
The 2015 Material Research Society Spring Meeting and Exhibit, April 4-10, 2015, San Francisco, USA.

9) Growth, structure, and cathodoluminescence property of ZnO nanorods prepared with low temperature reducing annealing.
Chaoyang Li, Xin Li, **Shengwen Hou**
The 21st International Display Workshops, December 3-5, 2014, Niigata, Japan.

10) Novel hybrid methods for fabricating large surface ZnO nanorods photoelectrode for dye-sensitized solar cell application.
Chaoyang Li, Xin Li, **Shengwen Hou**, Toshiyuki Kawaharamura
30th European Photovoltaic Solar Energy Conference and Exhibition, September 22-26, 2014, Amsterdam, Netherland.

11) Fabrication of vertical aligned ZnO nanorods on AZO thin film for photovoltaic applications.
Chaoyang Li, Xin Li, **Shengwen Hou**, Toshiyuki Kawaharamura, Mamoru Furuta,
21st International Workshop on Active-Matrix Flatpanel Displays and Devices, July 2-4, 2014, Kyoto, Japan.

Domestic conferences with proceeding as first author:

1) Dependence of ZnO nanostructures fabricated on the different substrates by a novel annealing method.
Shengwen Hou, Lilin Xie, Chaoyang Li

Electronics Society, Electronic Information Displays (EID) 2017, January 26-27, 2017, Tokushima, Japan. (Oral presentation)

2) Fabrication of ZnO nanorods as electrodes applying for dye-sensitized solar cells.
Shengwen Hou, Chaoyang Li
Symposium of Nanotechnology Institute, October 12, 2016, Kochi, Japan. (Oral presentation)

3) Fabrication of ZnO based dye-sensitized solar cell.
Shengwen Hou, Chaoyang Li
Symposium of Nanotechnology Institute, October 14, 2015, Kochi, Japan. (Poster presentation)

4) Low-temperature fabricating uniform and controllable ZnO nanorods.
Shengwen Hou, Chaoyang Li
62th Japan Society of Applied Physics Spring Meeting, March 11-15, 2015, Tokai University, Japan. (Oral presentation)

5) ZnO nanorods fabricated by chemical bath deposition.
Shengwen Hou, Chaoyang Li, Toshiyuki Kawaharamura
Symposium of Nanotechnology Institute, October 25, 2014, Kochi, Japan. (Oral presentation)1)DSSC.